

# REPORT DOCUMENTATION PAGE

AFRL-SR-AR-TR-05-

0077

Public Reporting burden for this collection of information is estimated to average 1 hour per response, including the gathering and maintaining the data needed, and completing and reviewing the collection of information. Send comments regarding this burden estimate or any other aspect of this collection of information, including suggestions for reducing this burden, to Washington Headquarters Services, Directorate for Information Operations and Reports, 1215 Jefferson Davis Highway, Suite 1204, Arlington, VA 22202-4302, and to the Office of Management and Budget, Paperwork Reduction Project (0704-0188), Washington, DC 20503.

1. AGENCY USE ONLY (Leave Blank)		2. REPORT DATE 02/21/05		3. REPORT TYPE AND DATES COVERED Final (02/01/02 - 11/30/040)	
4. TITLE AND SUBTITLE Control of Separation for Turbulent Boundary Layers Subjected to Wall Curvature and Streamwise Pressure Gradients				5. FUNDING NUMBERS F49620-02-1-0122	
6. AUTHOR(S) Dr. Hermann F. Fasel				8. PERFORMING ORGANIZATION REPORT NUMBER	
7. PERFORMING ORGANIZATION NAME(S) AND ADDRESS(ES) Department of Aerospace and Mechanical Engineering, University of Arizona, Tucson, AZ 85721				10. SPONSORING / MONITORING AGENCY REPORT NUMBER	
9. SPONSORING / MONITORING AGENCY NAME(S) AND ADDRESS(ES) USAF, AFRL AF Office of Scientific Research 4015 Wilson Blvd, Room 713 Arlington, VA 22203-1954 <i>NA</i>					
11. SUPPLEMENTARY NOTES					
12 a. DISTRIBUTION / AVAILABILITY STATEMENT Approved for public release; distribution unlimited.				12 b. DISTRIBUTION CODE	
13. ABSTRACT (Maximum 200 words)  Low Pressure Turbine (LPT) stages are important for modern jet engines, and in particular for engines used in Unmanned Aerial Vehicles (UAV). At low operating Reynolds numbers boundary layers remain laminar over a large downstream extent of LPT blades. Laminar boundary layer separation can cause significant reductions in turbine and overall engine performance. In an experimental research program at the Air Force Research Laboratory (AFRL), the potential advantages of Active Flow Control (AFC) for separation control were systematically explored. In collaboration with the experimental effort, we performed numerical investigations of AFC for LPT separation to investigate the relevant physical mechanisms. Numerical simulations can provide insight into flow details that is not possible in experiments. We chose a two-pronged approach: A computationally less efficient but more versatile finite volume code was employed for simulations of the full geometry. Open-loop control strategies were explored in 2-D calculations. Detailed investigations of the VGJ actuation for a flat plate model problem were performed with a very efficient finite difference code. The high-resolution DNS helped identify some of the key physical mechanisms responsible for the effectiveness of VGJs.					
14. SUBJECT TERMS				15. NUMBER OF PAGES 82	
				16. PRICE CODE	
17. SECURITY CLASSIFICATION OR REPORT UNCLASSIFIED	18. SECURITY CLASSIFICATION ON THIS PAGE UNCLASSIFIED	19. SECURITY CLASSIFICATION OF ABSTRACT UNCLASSIFIED	20. LIMITATION OF ABSTRACT UL		

NSN 7540-01-280-5500

Standard Form 298 (Rev.2-89)  
Prescribed by ANSI Std. Z39-18  
298-102

Enclosure 1

**FINAL REPORT**

AFOSR GRANT F49620-02-1-0122

**CONTROL OF SEPARATION FOR TURBULENT BOUNDARY LAYERS  
SUBJECTED TO WALL CURVATURE AND STREAMWISE PRESSURE  
GRADIENTS**

**Hermann F. Fasel**

Department of Aerospace and Mechanical Engineering  
The University of Arizona  
Tucson, AZ 85721



Submitted to  
Thomas J. Beutner  
Air Force Office of Scientific Research

February 2005





## ABSTRACT

The research focus for this grant was changed from the original more generic investigation to investigating separation and separation control for Low Pressure Turbine (LPT) blades. Low Pressure Turbine (LPT) stages are important for modern jet engines, and in particular for engines used in Unmanned Aerial Vehicles (UAV). One direction in the development of UAVs is the trend towards smaller vehicles, and therefore smaller jet engines. This leads to relatively low LPT operating Reynolds numbers (Reynolds numbers can drop to values as low as 25,000). In these operating ranges, boundary layers remain essentially laminar over a large downstream extent of the turbine blades, even in the presence of elevated free stream turbulence. This may lead to laminar boundary layer separation, which can cause a significant reduction in turbine and overall engine performance. In fact, increases of the loss coefficient as high as 300% have been reported (Sharma 1998). In an experimental research program at the Air Force Research Laboratory (AFRL) by Rivir and co-workers, the potential advantages of Active Flow Control (AFC) were systematically explored for low-pressure turbines. For example, they showed that the momentum deficit of a PakB cascade at off-design conditions could be reduced by 65% when pulsed Vortex Generator Jets (VGJs) were used. They were also able to demonstrate that the losses encountered when the blade spacing was increased by 50% could be almost completely eliminated with pulsed VGJs.

Although the experiments have convincingly demonstrated the potential benefits of VGJs, the relevant physical mechanisms are far from understood. In collaboration with the experimental effort, we performed numerical investigations of AFC for LPT separation. The objective was to exploit the synergism between the experimental and numerical efforts, in order to increase the chances for a breakthrough in the understanding of the physical mechanisms that are relevant for effective deployment of AFC for controlling LPT separation. Numerical simulations can provide insight into flow details that is not possible in experiments. We chose a two-pronged approach: A computationally less efficient but more versatile finite volume code was employed for simulations of the full geometry. Two- and three-dimensional simulations with and without turbulence models predicted the flow with various degrees of accuracy. Open-loop control strategies were explored in 2-D calculations. Detailed investigations of the VGJ actuation for a flat plate model problem were performed with a very efficient finite difference code. The high-resolution DNS shed light on some of the key physical mechanisms responsible for the effectiveness of VGJs. These simulations are truly of a "landmark" nature since they resolve all scales of motion down to the dissipative length scales.





# TABLE OF CONTENTS

	Page
ABSTRACT .....	iii
1. INTRODUCTION .....	1
1.1 Technical background .....	1
1.2 Vortex Generator Jets for Active Flow Control .....	3
1.3 Previous investigations of Low-Pressure Turbine Flows .....	5
2. NUMERICAL SIMULATIONS OF PAKB LOW-PRESSURE TURBINE BLADE INVESTIGATED EXPERIMENTALLY AT AFRL .....	7
2.1 Cases studied .....	7
2.2 Computational method .....	7
2.3 Computational grids and boundary conditions .....	8
2.4 Uncontrolled natural flow .....	10
2.4.1 Two-dimensional calculations .....	10
2.4.2 URANS calculations and Implicit Large Eddy Simulation .....	16
2.4.3 Three-dimensional simulations .....	22
2.4.4 Larger blade spacing .....	27
2.4.5 Periodic passing wake .....	28
2.5 Open-loop control .....	29
2.5.1 Set-up of 2-D flow actuation .....	29
2.5.2 Results for design blade spacing .....	31
2.5.3 Results for 25% larger blade spacing .....	35
2.5.4 Pulsed Vortex Generator Jets .....	40
3. DIRECT NUMERICAL SIMULATION OF LAMINAR SEPARATION BUBBLES AND ACTIVE FLOW CONTROL USING VORTEX GENERATOR JETS .....	45
3.1 Numerical method and code development .....	45
3.2 Hydrodynamic instabilities in laminar separation bubbles .....	46
3.2.1 Case 1: steady separation bubble .....	47
3.2.2 Case 2: marginally unsteady separation bubble .....	52
3.2.3 Case 3: highly unsteady separation bubble .....	54
3.3 Active control of a generic separation bubble using vortex generator jets .....	57
3.3.1 Steady VGJs .....	61
3.3.2 Pulsed VGJs .....	63
3.4 Direct Numerical Simulations of active flow control for a boundary layer subjected to low-pressure turbine blade conditions .....	66
3.4.1 Steady VGJs .....	71
3.4.2 Pulsed VGJs .....	72
4. SUMMARY AND CONCLUSION .....	75
5. CONFERENCES, WORKSHOPS, AND PAPERS .....	78
REFERENCES .....	79





## 1. INTRODUCTION

### 1.1 Technical background

Low Pressure Turbine (LPT) stages are important components of many modern jet engines. In the recent past, unmanned aerial vehicles (UAVs) are becoming increasingly important for military operations. One direction in the development of UAVs is the trend towards smaller vehicles, and therefore smaller jet engines. This leads to relatively low LPT operating Reynolds numbers (the Reynolds numbers can drop to values as low as 25,000). In these operating ranges, boundary layers remain essentially laminar over a large downstream extent of the turbine blades, even in the presence of elevated free stream turbulence. As a consequence, the laminar boundary layer flow separates from the blades, causing significant losses in turbine and overall engine performance. In fact, increases of the loss coefficient as high as 300% have been reported (Sharma 1998).

It was recognized several years ago that Active Flow Control (AFC) applied to LPT blades can counter such unfavorable conditions, and that AFC could lead to considerable performance improvements as well as to a reduction in component weight. In a broadly based experimental research program at the Air Force Research Laboratory (AFRL) at Wright-Patterson Air Force Base, Rivir and co-workers (Bons et al. 1999, 2000, 2001, Sondergaard et al. 2002) systematically explored the potential advantages of employing AFC for low-pressure turbine stages. Bons et al. (2000) have shown that the momentum deficit of a PakB cascade at off-design conditions could be reduced by 65% when pulsed vortex generator jets (VGJs) were used. Sondergaard et al. (2002) showed that the losses encountered when the blade spacing was increased by 50% could also be successfully eliminated with pulsed VGJs.

Since off-design conditions are unavoidable, conservative design margins have to be adopted in the design of LPT stages to guarantee safe and reliable operation. An on-demand flow control system that would assist during critical off-design operation and that can be deactivated during cruise flight conditions could therefore be very beneficial. A different strategy would be to reduce the blade count (and thus component weight) and avoid separation in all flight conditions, including cruise, by continuously applying active flow control. The experiments at AFRL have shown that even when AFC is implemented into an existing (conventional) blade design (PakB), already significant improvements of LPT performance can be achieved. Therefore, when considering integration of AFC for low pressure turbine (LPT)



blades from the very beginning of engine development, and not just as an add-on or "fix", more aggressive designs can be contemplated which may ultimately result in true breakthroughs in the efficiency and overall performance of jet engines.

Although the experiments at AFRL by Rivir and co-workers have convincingly demonstrated the potential benefits of VGJs the relevant physical mechanisms are far from understood. In other words, the fundamental question, "why are VGJs so effective in preventing separation and stall or reattaching separated boundary layers for LPT blades?" has yet to be answered. The underlying physics are highly complex, as both *unsteady separation* and *transition* mechanisms are at work interactively. Each of these areas by itself, *transition* from laminar to turbulent flow and *unsteady separation*, belong to the least understood areas of flow physics. The main understanding of transition is based on the so-called linear regime, where the amplitudes of the instability waves are small and, as a consequence, the so-called linear stability theory can be employed for modeling. For LPT applications, as a consequence of the strong streamwise amplification of the disturbance waves, the disturbances quickly reach very large amplitudes. The strong amplification is due to the streamwise adverse pressure gradients, the convex wall curvature (suction side of blade), and the elevated free stream turbulence in turbine operations (when compared to external free flow conditions). Therefore, linear theory is not applicable (in particular for high free stream turbulence levels) and the transition mechanisms are not "linear" (not of Tollmien-Schlichting type). Rather, the transition process is of a "by-pass" nature (Morkovin 1969), that is the linear stages are by-passed. Due to the non-linearity and the non-uniqueness of the by-pass mechanisms, slight changes in "initial" conditions (say, operating conditions) can result in drastically different breakdown-to-turbulence scenarios.

The fundamental understanding of separation is almost as incomplete as that of transition, especially when the separation process is unsteady and three-dimensional as in the application to be investigated here. The unsteadiness is introduced by the pulsing of the VGJs and/or by the naturally present large "coherent" flow structures, which result from the instability of the separated "base flow". The three-dimensionality is caused by the fact that the jets are injected through small holes that are relatively far apart from each other (several hole diameters). For time-dependent, three-dimensional separation, even the definition of unambiguous "separation" criteria is a challenge (see for example the Moore, Rott, Sears (MRS) criterion, Schlichting and Gersten 2000). Again, as for transition, boundary layer separation under such conditions is a highly non-linear, non-unique process that exhibits a strong sensitivity to "initial" conditions.

Clearly, for LPT separation, the two mechanisms interact non-linearly, thereby considerably



expanding the range of non-uniqueness. Separation, in general, strongly accelerates transition, while transition, in general, delays or can even prevent separation. However, to what degree they affect each other depends on the details of the "initial" conditions and is strongly influenced by the geometry (roughness, wall curvature, wall temperature, jet geometry, frequency and amplitudes of forcing, etc.). Thus, when both of these non-linear, non-unique mechanisms are at work at the same time, as is the case for the LPT, surprises are likely, both positive and negative. For example, when frequencies and amplitudes of the pulsed blowing are "just right", the effectiveness of separation control is indeed stunning, requiring a very small energy input. In other instances, although unintentional and often due to a lack of understanding, AFC is not effective in the sense that separation is not prevented/delayed or that an unacceptable energy input is required. Therefore, in light of the complex physics that are at work in AFC for LPTs using vortex generator jets, it is obvious that a better understanding of the most relevant physical mechanisms needs to be achieved before this technology can be transitioned successfully into practice and to ensure safe, reliable and effective operation.

Funded by AFOSR a research program was initiated at the University of Arizona in collaboration with AFRL to numerically investigate AFC using VGJs for LPT applications. The hope was that, with the synergism between the experimental effort and our numerical simulations, the chances for a breakthrough in the understanding of the relevant physical mechanisms would be significantly increased. While narrow parameter ranges may be explored more easily in the experiments, larger changes of the flow parameters (e.g. geometry, locations of the AFC devices, forcing frequencies and amplitudes etc.) can be more easily investigated with numerical simulations. Most importantly, numerical simulations can provide insight into flow details not possible in experiments.

## **1.2 Vortex Generator Jets (VGJs) for Active Flow Control (AFC)**

Extensive experimental investigations of active LPT separation control have been performed by Rivir and co-workers at AFRL (Bons et al. 1999, 2000, 2001, Sondergaard et al. 2002) and at Brigham Young University by Bons and co-workers. These investigations have focused on AFC using Vortex Generator Jets (VGJs), both steady and pulsed. The jets were employed at a skew angle of  $90^\circ$  (the angle formed by the projection of the jet onto the surface and the free stream direction) and a pitch angle of  $30^\circ$  (the angle formed by the jet and the surface). Rivir and co-workers found that, with pulsed VGJs, a drastic reduction in boundary



layer separation on the suction side of a PakB LPT blade at a Reynolds number of 25,000 could be achieved. Various jet velocity amplitudes and duty-cycles (ratio of jet on-time to pulsing period) were investigated. Both steady and pulsed blowing was reported to be effective in reducing separation losses. However, pulsed blowing was shown to be much more efficient, requiring only a small fraction of the mass flow rate compared to the steady VGJs. The major impact of VGJ control was attributed to triggering early boundary layer transition, especially when the jets were employed near the "natural" (uncontrolled) separation location. Bons and Sondergaard et al. also proposed that the underlying physical mechanisms responsible for the effectiveness of the separation control using pulsed jets may be different from using steady jets.

Most of the prior research conducted on VGJs has involved jets issuing into turbulent boundary layers. Johnston and Nishi (1990) considered spanwise arrays of pitched and skewed steady VGJs and reported the formation of streamwise vortices in the boundary layer. Compton and Johnson (1992) investigated the streamwise development of such longitudinal structures and concluded that skew angles of  $45^\circ$  to  $90^\circ$  created the strongest vortices. They also showed that the vortices produced by the steady jets were similar to weak vortices generated by solid vortex generators. Henry and Pearcey (1994) investigated the three-dimensional flow field generated by pitched and skewed VGJs issuing into a turbulent boundary layer using numerical simulations. Their simulations identified the importance of the streamwise pressure gradient as a parameter influencing the development of the observed streamwise vortices. Later, Khan and Johnston (2000) employed three-component laser Doppler velocimetry to further investigate the characteristics of the dominant streamwise vortices created by pitched and skewed VGJs. They found that, for their experimental configuration, a pitch angle of  $30^\circ$  and a skew angle of  $60^\circ$  generated vortices with the highest peak vorticity. They reported that turbulence levels in the boundary layer were enhanced by the presence of the vortices. It is generally believed that this increased turbulent mixing is responsible for the effectiveness of VGJs in turbulent boundary layer separation control.

Pulsed VGJs were first considered by McManus et al. (1994). The jets were reported to successfully prevent separation in an otherwise stalled two-dimensional diffuser. The pulsed VGJs were found to cause the formation of large-scale turbulent structures which promote mixing in the boundary layer region. In comparison to steady VGJs, the pulsed jets improved separation control significantly for a fixed mass flow rate. In an effort to shed light on the physics of pulsed jet separation control, Johari and McManus (1997) investigated the interaction of pulsed VGJs with a zero pressure gradient turbulent boundary layer from the



perspective of vorticity dynamics. They attributed the improved performance of pulsed VGJs (compared to steady VGJs) to the formation, stretching and bending of vortex ring structures.

Due to the limited research conducted on VGJs and their role in active flow control, many of the underlying physical mechanisms are still far from understood. The question arises whether the mechanisms that are reportedly responsible for increased mixing in turbulent boundary layers are equally relevant for laminar (transitional) separation such as for LPT blades.

### **1.3 Previous investigations of Low-Pressure Turbine (LPT) flows**

Several researchers have performed numerical simulations of LPT flows and the related problems of laminar separation on a flat-plate boundary layer subjected to a streamwise pressure gradient or passing wakes. Two-dimensional (2-D) and three-dimensional (3-D) Implicit Large Eddy Simulations (ILES) of the PakB cascade at Reynolds numbers of  $Re=25,000$ ,  $50,000$ , and  $100,000$  with and without AFC by VGJs were performed by Rizzetta and Visbal (2003, 2004) with a high-order accurate compressible code. For  $Re=25,000$  the simulations indicated flow transition and flow reattachment close to the trailing edge. The reattachment location was at  $0.97C_x$  in the 2-D computation and at  $0.85C_x$  in the 3-D computation ( $C_x$  is the axial chord length). In the experiments by Rivir and co-workers (Bons et al. 1999, 2000, 2001, Sondergaard et al. 2002) the flow reattached at  $x>0.99C_x$ . Due to the earlier reattachment in the 3-D ILES the pressure recovery is stronger than in the 2-D computation. Flow separation is predicted at  $\sim 0.7C_x$  for both cases. This compares well to the experimental value of  $\sim 0.7C_x$ . A 2-D computation at  $Re=25,000$  with a higher-order accurate compressible code was also performed by Mutnuri et al. (2003). They predicted flow separation at  $0.71C_x$  and showed a wall pressure distribution that matched experimental results by Huang et al. (2003). The same geometry was also investigated by us using a high-order compressible code (Gross and Fasel 2004). It was shown that the flow can be successfully controlled with pulsed blowing through a slot. Highly resolved three-dimensional simulations were presented for a flat-plate boundary layer subjected to the same streamwise pressure gradient as measured in the experiments of Rivir and co-workers (Postl et al. 2003, 2004). Various parameters associated with VGJ control were explored and insight was gained into the physical mechanisms responsible for the successful separation control.

Raverdy et al. (2003) performed an ILES of the T106 LPT blade in a linear cascade at  $Re=110,000$ . The code was second order accurate and based on the compressible Navier-



Stokes equations in the finite volume formulation. The largest computational grid had 2 million grid points. Mean velocity profiles and wall pressure distribution of the experiment were matched. A Large Eddy Simulation (LES) of the same geometry at a Reynolds number of 58,100 with 10.6 million grid points was carried out by Michelassi et al. (2003). The incompressible Navier-Stokes equations were solved with a second order accurate finite volume method and a dynamic subgrid stress model. The transition of the laminar boundary layer on the suction side by periodic upstream wakes and the appearance of longitudinal vortices on the pressure side were studied. The same case, at the higher Reynolds number of 148,000, was also studied by Xiaohua and Durbin (2001). They used a second-order accurate incompressible code with 57 million grid points. The focus of this investigation was on the formation of longitudinal vortices on the pressure side of the blades caused by the passage of the distorted periodic upstream wake. With the same numerical method, Xiaohua et al. (1999) also studied the interaction of periodic passing wakes with a laminar boundary layer on a grid with 52.4 million grid points. Particular focus was on the appearance of turbulent spots and their downstream development into turbulent strips. They found that flow separation can occur between these turbulent strips. Suzen and Huang (2004) developed an intermittency model to more cost effectively study the wake/blade interaction. Results for the PakB cascade at a Reynolds number of 50,000 were obtained from an incompressible second-order accurate code. They studied the effect of the wake passing frequency on the wall pressure distribution. Steady state 2-D RANS calculations of the PakB cascade at Reynolds numbers 25,000, 50,000, and 100,000 with  $k-\omega$  turbulence model were performed by Garg (2002). The dimensionless turbulent viscosity at  $Re=50,000$  was of order 1.

Although this brief literature survey is by no means complete, it reflects the strong interest in the problem of LPT blade separation. The simulation of separating/transitioning LPT flows alone challenges existing CFD codes and computer platforms and motivates the development of modeling techniques like LES and URANS. While some understanding of unsteady LPT flows has been obtained (e.g. the generation of streamwise vortices on the LPT pressure side triggered by periodic upstream wakes) the physics of pulsed VGJs for LPT separation control has not yet been fully understood. This report summarizes the AFOSR funded research effort that has been made at the University of Arizona to produce high-fidelity LPT flow simulations and to add to the understanding of AFC by VGJs.



## 2. NUMERICAL SIMULATIONS OF PAKB LOW-PRESSURE TURBINE (LPT) BLADE INVESTIGATED EXPERIMENTALLY AT AFRL

### 2.1 Cases studied

For our simulations we chose the  $Re=25,000$  case from the experiments by Rivir and co-workers at AFRL (Bons et al. 1999, 2000, 2001, Sondergaard et al. 2002). The Reynolds number was based on the axial chord length  $C_x=0.1778\text{m}$  and the inflow velocity,  $v_\infty$ . Of the many cases studied in the experiments this one was most susceptible to laminar separation. The inflow Mach number in the experiments was 0.0064. The inflow angle was  $35^\circ$ , the outflow angle was fixed to  $60^\circ$ . The design speedup ratio (ratio of turbine outflow and inflow velocity) was 1.64. The experimental cascade had 8 blades and a span of  $\sim 5C_x$ . In the computations, both the number of blades and the span were assumed to be infinite (periodicity conditions). Simulations were performed for the design blade spacing,  $d/C_x=0.88$ , and a 25% larger blade spacing,  $d/C_x=1.1$ .

### 2.2 Computational method

A CFD code developed in our group was employed for simulations of the experimental cascade. The code solves the compressible Navier-Stokes equations in curvilinear coordinates. For robustness (especially on highly distorted grids) the finite volume method is employed for the convective terms. Since high-order accurate finite volume formulations of the viscous terms are very cumbersome, these terms are computed with finite differences. Low- and high-order discretizations are available: For low-order, the convective terms are discretized with a 2<sup>nd</sup>-order accurate symmetric Total Variation Diminishing (TVD) scheme (Yee 1987) and the viscous terms are discretized with 2<sup>nd</sup>-order accurate finite differences. According to Margolin and Rider (2002), this low-order accurate upwind scheme discretization should allow for Implicit Large Eddy Simulations (ILES). For ILES the numerical truncation error of the discretization must exhibit similar diffusion characteristics at the smallest resolved scales as standard sub-grid scale turbulence models used in Large Eddy Simulation (LES). The higher-order discretization of the convective terms is based on 5<sup>th</sup>, 7<sup>th</sup>, and 9<sup>th</sup>-order accurate upwind schemes based on a Weighted Essentially Non-Oscillatory (WENO) extrapolation of the characteristic variables and the Roe scheme (Gross and Fasel 2002). Fourth-order accurate finite differences were used for



the viscous terms. In both cases, an implicit 2<sup>nd</sup>-order accurate Adams-Moulton method is employed for time integration. The resulting system of equations is solved iteratively by a Newton iteration based on a line Gauss-Seidel algorithm. The convergence of the implicit method is monitored by checking the residuals  $R_m$  of the governing equations. The global residual,  $R$ , is defined by summation over all cells  $N$  and taking the maximum over all equations  $m$ ,

$$R = \max_m \left( \sqrt{\frac{1}{N} \sum_N R_m^2} \right)$$

All cases were integrated with a non-dimensional time step of  $\Delta t=0.001$ . This resulted in CFL numbers of about 350~450. When the implicit method was converged until the global residual,  $R$ , dropped below 1, 15-25 iterations of the implicit method were required per time step. The code was parallelized using the Message Passing Interface (MPI) and scales well on larger number of processors (linear speedup was achieved for up to 32 processors on a SGI Origin 2000. Calculations were performed on 16 processors on a SGI Origin 3400 and on 32 processors on a HP GS 1280.

### 2.3 Computational grids and boundary conditions

A multi block Poisson grid generator developed in our group was utilized for obtaining grids of sufficient smoothness and quality for the current investigations, i.e. for the design blade spacing,  $d/C_x=0.88$ , and the 25% larger blade spacing,  $d/C_x=1.1$ . A 5 block grid structure was chosen (Fig. 2.1), with an O-block encompassing the blade. Grid points were clustered on the suction side of the blade where the separation bubble was anticipated and in the wake region of the blade for resolving the vortex street. Massive grid stretching was applied at the inflow and outflow boundaries to dampen upstream and downstream traveling waves. The total number of cells was 31600 (coarse grid) and 91300 (fine grid) for the two-dimensional (2-D) grids. Although the majority of the studies were done with the fine grid, some of the preliminary investigations were performed on the coarse grid. For the three-dimensional (3-D) simulations, the fine grid was extended in the spanwise  $z$ -direction using 64 cells. In accordance with findings by Rizetta and Visbal (2003) the spanwise extent of the computational domain was set to  $\Delta z=0.2C_x$ . The total number of cells of the 3-D grid was 5.8 million. The grid resolution in wall



units (based on boundary layer conditions on the suction side at  $0.5C_x$ ) was between 3 and 33 in the streamwise direction, between 0.5 and 1 in the wall normal direction, and 9 in the spanwise direction (for comparison, Rizzetta and Visbal (2003) used 3.1...50.6, 0.4, 6.5).

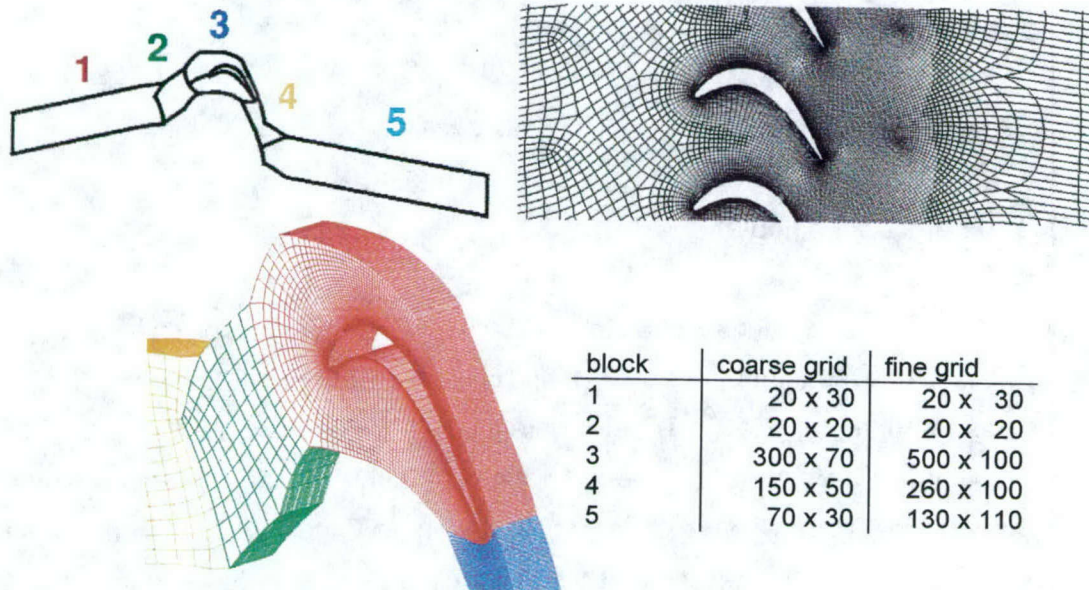


**Fig. 2.1:** Computational grid used for all but 3-D ILES results. Every other grid line is omitted for clarity. Block structure, 2-D grid, 3-D grid (64 points in  $z$ ,  $\Delta z=0.2$ ) and block resolutions. Shown is grid for design blade spacing,  $d/C_x=0.88$ .

At the inflow boundary, the velocity components and the temperature were prescribed while the static pressure was extrapolated from the interior. At the outflow boundary, temperature and velocities were extrapolated while the static pressure was prescribed. The walls were treated as adiabatic. All other boundaries were periodic.

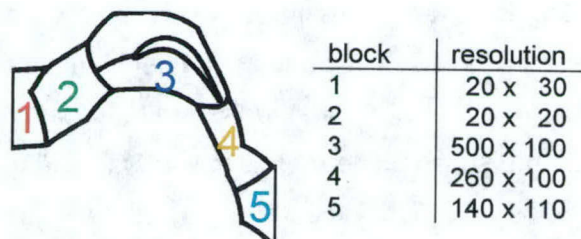


**Fig. 2.2:** Block structure and block resolution of computational grid used for 3-D ILES.

The streamwise extent of the computational domain was reduced for the 3-D ILES simulations (Fig. 2.2). Streamwise grid stretching was applied at the inflow and outflow



boundaries. The spanwise extent of the grid was  $\Delta z=0.1$  and identical to the hole spacing of the Vortex Generator Jets (VGJs) employed for flow control. 32 cells were used in the spanwise direction. The total number of cells was 92400 for the 2-D grid and 3.0million for the 3-D grid. A non-reflecting boundary condition based on suggestions by Thompson (1987) and Kim and Lee (2000) was applied at the inflow and outflow boundaries.

## 2.4 Uncontrolled natural flow

### 2.4.1 Two-dimensional calculations

Preliminary 2-D investigations with an inflow Mach number of  $M=0.25$  on the coarse grid did not agree well with the measurements by Rivir and co-workers at AFRL (Bons et al. 1999, 2000, 2001, Sondergaard et al. 2002). To elucidate possible reasons for the discrepancies, sensitivities of the CFD results with respect to various parameters, namely Reynolds number,  $Re$ , inflow angle,  $\alpha$ , (different to the experiments the outflow angle was not specified in the simulations), inflow Mach number,  $M$ , and blade spacing,  $d/C_x$ , were investigated (Fig. 2.3). Shown are curves of the time-averaged wall pressure coefficient,

$$c_p = (p - p_\infty) / (0.5 \rho_\infty v_\infty^2).$$

For variations in Reynolds number up to 5000 the solution did not change considerably (Fig. 2.3a). Changes of the inflow angle in the order of  $1^\circ$  had a very limited impact on the pressure distribution (Fig. 2.3b). However, when the inflow Mach number was lowered the pressure distribution did get significantly closer to the experimental data (Fig. 2.3c). Experience with other flow problems (that did, however, not feature flow acceleration comparable to the LPT flow) and the fact that compressible codes do converge faster for higher Mach numbers lead to the choice of an inflow Mach number of 0.25. It was then later detected that the maximum Mach-number of the flow on the suction side for this inflow Mach number was about 0.7 and well within the compressible regime. From the sensitivity study it became apparent that an inflow Mach-number of 0.1 was sufficiently small. All further calculations were hence performed with an inflow Mach-number of 0.1. (It should be kept in mind that the inflow Mach number in the experiments was 0.0064.) As expected, the blade spacing,  $d/C_x$ , had a strong impact on the pressure distribution (Fig. 2.3d).

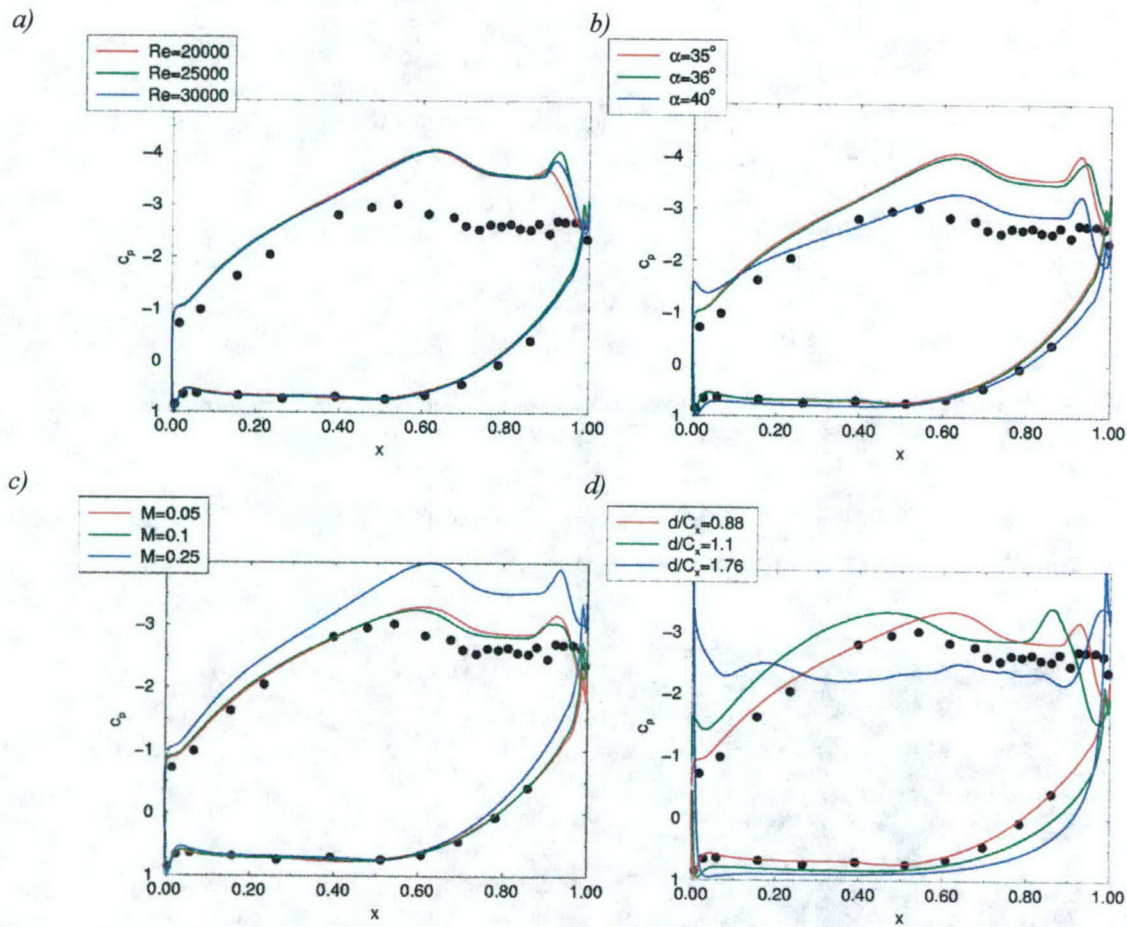


**Fig. 2.3: Time-averaged wall pressure coefficient. Sensitivity of flow to variations in a) Reynolds number,  $Re$ , ( $\alpha=35^\circ$ ,  $M=0.25$ ,  $d/C_x=0.88$ ), b) inflow angle,  $\alpha$ , ( $Re=25000$ ,  $M=0.25$ ,  $d/C_x=0.88$ , outflow angle is not fixed), c) inflow Mach number,  $M$ , ( $Re=25000$ ,  $\alpha=35^\circ$ ,  $d/C_x=0.88$ ) and d) blade spacing,  $d/C_x$ , ( $Re=25000$ ,  $\alpha=35^\circ$ ,  $M=0.1$ ). Coarse grid results.**



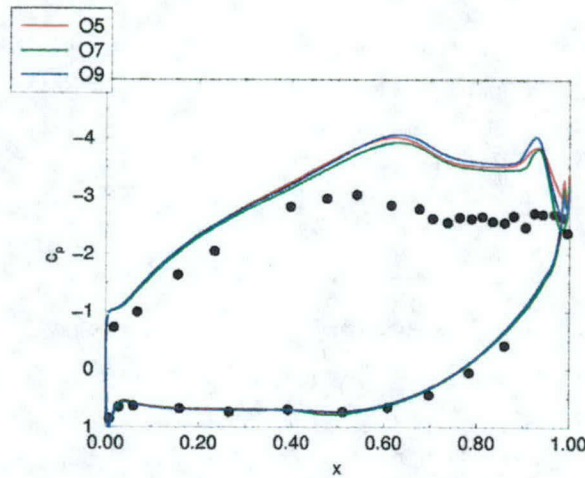


*Fig. 2.4: Dependence of time-averaged wall pressure coefficient on accuracy of numerical scheme ( $Re=25000$ ,  $\alpha=35^\circ$ ,  $M=0.25$ ,  $d/C_x=0.88$ ). Coarse grid results.*

When the accuracy of the discretization of the convective terms was altered the predicted wall pressure distribution did not change noticeably (Fig. 2.4).

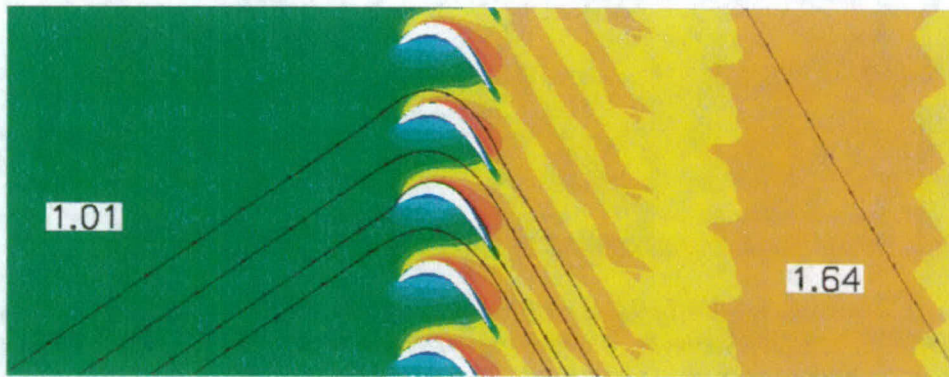


*Fig. 2.5: Iso-contours of time-averaged total velocity and streamlines.*

The computed speed-up ratio agrees well with the experimental value of 1.64 (Figs. 2.5 and 2.6). Cascade inflow and outflow angles were also in close accordance with the experimental findings (Fig. 2.6). In the simulations the inflow angle was prescribed while the outflow angle was variable and entirely determined by the flow solver. In the experiment, the inflow angle was set to  $35^\circ$  and the outflow angle was set to  $60^\circ$ .



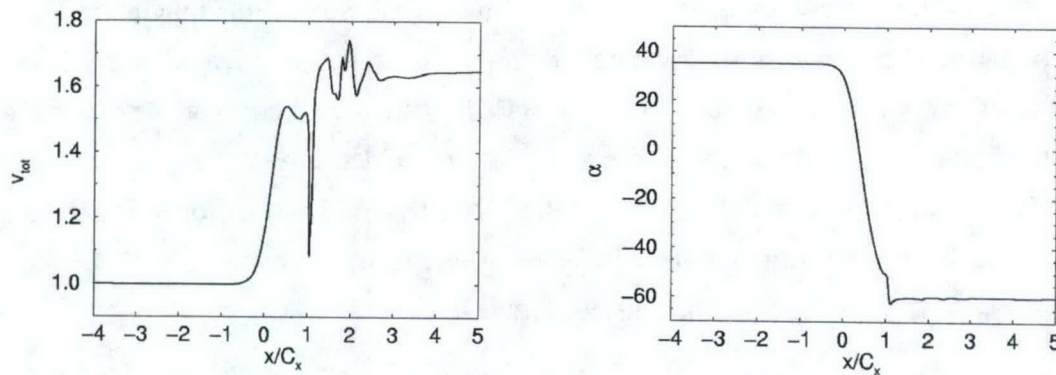


**Fig. 2.6: 2-D calculation of entire cascade at design blade spacing,  $d/C_x=0.88$ . Time-averages. Left: Total velocity and right: stream line angle along  $y=\text{const.}$  line.**

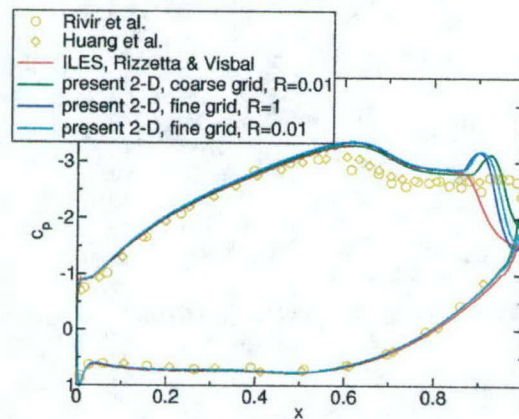


**Fig. 2.7: Time-averaged wall pressure coefficient. Experiments by Rivir and co-workers at AFRL and Huang et al. and numerical simulations: 3-D ILES by Rizzetta and Visbal. Last three curves are 2-D simulations on coarse and fine grid for different convergence criteria.**

Dependence of the numerical result on the grid resolution and the accuracy of the implicit time stepping method (global residual,  $R$ ) was studied as well (Fig. 2.7). Included in the same figure are measurements by Rivir and co-workers and Huang et al. (2003), as well as the wall pressure distribution from a 3-D ILES by Rizzetta and Visbal (2003). The inflow turbulence level was about 1% in both experiments. The agreement between the numerical simulations is very good except in a region near the trailing edge of the blade. The “hump” that appears in the  $c_p$ -distributions for the 2-D calculation is not visible in the experiments and in the 3-D calculation. This “hump” is caused by the formation of strong spanwise coherent structures as shown in Fig. 2.8. The strength of these structures is overpredicted in the 2-D calculation when compared with the 3-D simulations. The onset of strong turbulent mixing in the 3-D calculation weakens



the coherence of the spanwise structures. The result by Rizzetta and Visbal (2003) shows a significantly stronger pressure recovery close to the trailing edge. This may be the result of turbulent mixing and an earlier reattachment of the turbulent flow. Fine grid results are shown for two iteration convergence criteria,  $R=1$  and  $R=0.01$ . The  $R=0.01$  calculations required about 80-90 iterations per time step. The results are sufficiently close to each other to justify the use of  $R=1$  for the following calculations. The coarse and fine grid results for  $R=0.01$  are close enough to each other for demonstrating grid convergence. For the following investigations, the fine grid was considered to be sufficiently well resolved.

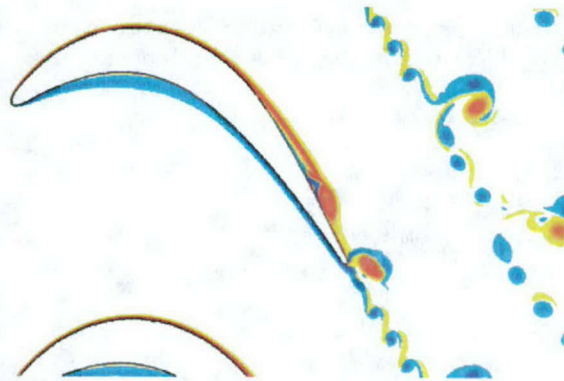


*Fig. 2.8: Instantaneous visualization of spanwise vorticity. Results for design blade spacing,  $d/C_x=0.88$ . Fine grid results.*

Iso-surfaces of instantaneous spanwise vorticity,

$$\omega_z = \partial v / \partial x - \partial u / \partial y,$$

are shown in Fig. 2.8. The separated shear layer is inviscidly unstable. Small disturbances are exponentially amplified to non-linear amplitudes, leading to the formation of spanwise vortices that are traveling in downstream direction and increase the wall normal momentum exchange. The additional mixing thickens and reattaches the boundary layer. Downstream of the blade the spanwise structures interact with the counter-rotating vorticity originating from the pressure side of the blade. The trailing wake is dominated by the shedding frequencies (and their lower and higher harmonics) associated with the instability of the separated shear layer (low frequencies) and the trailing edge separation (high frequencies).



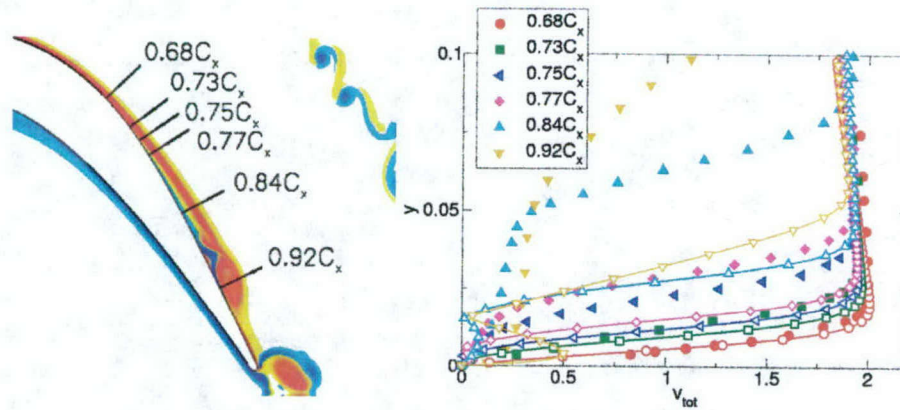


**Fig. 2.9:** Time-averaged profiles of total velocity,  $v_{tot} = \sqrt{(u^2 + v^2)}$ . Left: Instantaneous visualization of spanwise vorticity and locations where velocity profiles were taken. Right: Comparison with measurements by Rivir and co-workers. Results are for design blade spacing,  $d/C_x = 0.88$ .

In Fig. 2.9, velocity profiles at various streamwise locations obtained from the 2-D calculation are compared with measurements by Rivir and co-workers. At 68% axial chord, the profiles match very well. At all other stations, the measured velocity profiles differ significantly from the computed profiles. The deviation appears to be mainly due to the different separation location in the experiment. Overall, the experimental data indicate a larger separation bubble than the simulations. The  $c_p$ -curves in Fig. 2.7 show a systematic discrepancy between the numerical simulations and the experimental data. This discrepancy has also been noticed in previous studies (Postl et al. 2003, 2004) and remains disputed until today. In the simulations the wall pressure increase associated with the laminar separation sets in farther downstream and the pressure plateau in the separated region is lower. Based on a detailed discussion with the experimentalists it was conjectured that the slightly different geometry used in the experiment (the blades do not precisely match the PakB design) could be responsible for some of the differences observed between the computations and the experiments at AFRL. Therefore, a 2-D comparison calculation was carried out for a blade with geometry data obtained from precision measurements of a warped blade. Since the result shows no significant effect on the separation location when compared to the original PakB design (Fig. 2.10) it was concluded that minor geometry inaccuracies do not explain the discrepancies between experiment and computations.



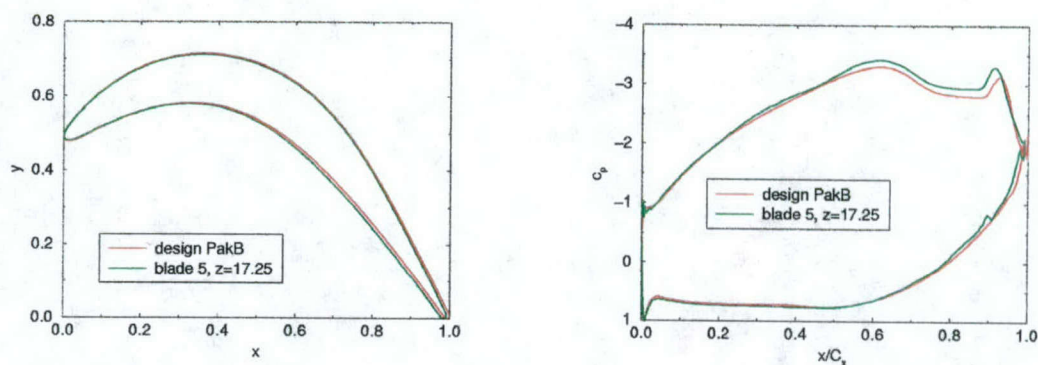


*Fig. 2.10: Computation of entire cascade at design blade spacing,  $d/C_x=0.88$ . Comparison of design PakB geometry with slightly warped rapid-prototyped geometry. Left: Comparison of geometries and right: pressure coefficient.*

Reasons for the consistently smaller separation region in the simulations may be insufficient grid resolution or numerical accuracy, arguing that added numerical diffusion delays separation. Although it can not be excluded that some systematic error was made when modeling the experimental set-up (e.g. finite number of blades in the experiment, instrumentation not on all blades, manufacturing inaccuracies, blades not being precisely aligned with each other, fixed outflow angle, inflow turbulence levels, surface roughness, etc.) the main objection to the current 2-D simulations stems from the fact that the flow is transitional and hence 3-D. To clarify if turbulent mixing had a significant impact on the separation location two steps were taken: Turbulence modeling was applied in 2-D calculations and the transition process was studied in 3-D simulations.

#### **2.4.2 Unsteady Reynolds-Averaged Navier-Stokes (URANS) calculations and Implicit Large Eddy Simulation (ILES)**

Since the LPT flow is transitional the most reliable and also most computationally expensive approach is to perform a well-resolved 3-D Direct Numerical Simulation (DNS). Because this approach requires enormous grid resolutions incurring massive computational cost one may also feel tempted to model the small-scale turbulent motion in Unsteady Reynolds-Averaged Navier-Stokes (URANS) calculations or Implicit Large Eddy Simulations (ILES) at a dramatically lower computational expense. So far three different turbulence modeling approaches have been applied to LPT flows: Reynolds-averaged Navier-Stokes (RANS) (Garg 2002, Chernobrovkin and Lakshminarayana 1999), Large Eddy Simulation (LES) (Michelassi et al.



2003), and ILES (Raverdy et al. 2003, Rizzetta and Visbal 2003, Gross and Fasel 2004), were the diffusion of the numerical discretization acts as turbulence sub-grid stress model (Margolin and Rider 2002).

Here, for URANS, the 1998  $k$ - $\omega$  turbulence model by Wilcox (2000), in both the standard and the low Reynolds number formulation, was employed in conjunction with the Boussinesq-assumption or the explicit algebraic Reynolds stress model (EASM) by Gatski (Gatski and Sepziale 1993, Gatski and Jongen 2000, Rumsey and Gatski 2001). Two additional equations, one for the turbulence kinetic energy,  $k$ , and one for the turbulence dissipation,  $\omega$ , need to be solved. The  $k$ -production term,

$$P_k = 1/\text{Re} \tau_{ij}^T \partial v_i / \partial x_j,$$

is computed from the Reynolds stresses,  $\tau_{ij}^T$ , and the mean flow velocity gradients,  $\partial v_i / \partial x_j$ . It is subtracted from the energy equation of the Navier-Stokes equations. The eddy viscosity is computed from

$$\mu_T = \rho k / \omega,$$

where  $\epsilon = \text{Re} \beta^* k \omega$ . For the 1998  $k$ - $\omega$  model  $\beta^*$  and  $\beta$  are dependent on derivatives of  $k$ ,  $\omega$ , and the local strain rate and vorticity (Wilcox 2000). In the original formulation the Boussinesq-approximation is employed for computing the Reynolds stresses. When the Explicit Algebraic Stress Model (EASM) is used, the turbulence equations are solved for  $k$  and  $\omega = 0.09 \omega$  and the eddy viscosity is computed as  $\mu_T = c_\mu \rho k / \omega$  with model-dependent  $c_\mu$ .

For the current calculations different combinations of the various turbulence modeling elements were explored in 2-D calculations. The convective terms were computed with the 5<sup>th</sup>-order accurate WENO scheme to assure that turbulence model properties were not obscured by the numerical diffusion of the mean flow discretization. The wall was considered to be hydraulically smooth. The turbulence kinetic energy  $k$  was set to zero at the wall. For the wall next cell,  $\omega$  was computed from the wall distance  $y^+$  (Wilcox 2000). The computed value was then multiplied by 10 and used as  $\omega$  wall value. A boundary condition accounting for surface roughness is available but was not employed.

For ILES, the convective terms were discretized with a 2<sup>nd</sup>-order accurate symmetric TVD scheme (Yee 1987). Margolin and Rider (2002) argue that 2<sup>nd</sup>-order upwind schemes in the finite volume formulation have diffusion characteristics akin to the subgrid-stress provided by



standard LES models. The viscous terms were computed with 2<sup>nd</sup>-order accurate finite differences.

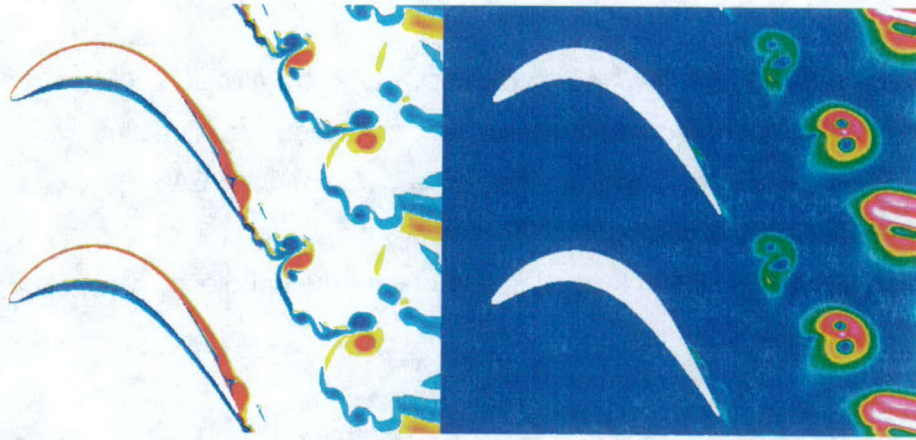
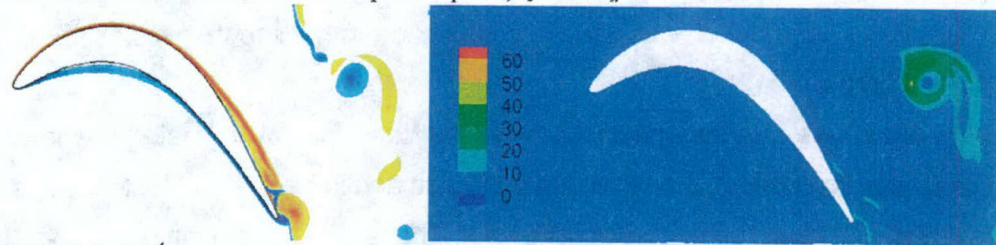


*Fig. 2.11: Computation of entire cascade at design blade spacing,  $d/C_x=0.88$ . URANS computation with combination of 1988 Wilcox  $k-\omega$  turbulence model and Rumsey and Gatski EASM model. Iso-contours of left: spanwise vorticity and right: eddy viscosity ( $0 \leq \mu_T/\mu \leq 0.5$ ). No transition model was used.*

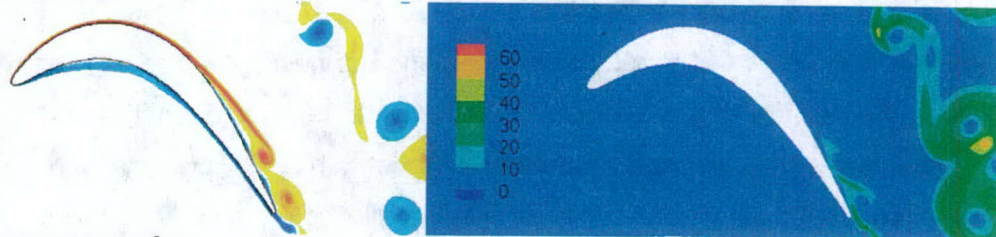
Earlier results with 1988  $k-\omega$  model and extremely laminar inflow ( $I_T=6.3 \cdot 10^{-6} C_x$ ,  $Tu_\infty=0.0058\%$ ) were somewhat discouraging (Fig. 2.11). Eddy-viscosity,  $\mu_T$ , built up in the separation region close to the trailing edge and in the structures downstream. However, the eddy viscosity level was of the same order as the laminar viscosity. It was decided that more research was needed to identify turbulence models appropriate for transitional LPT flows.



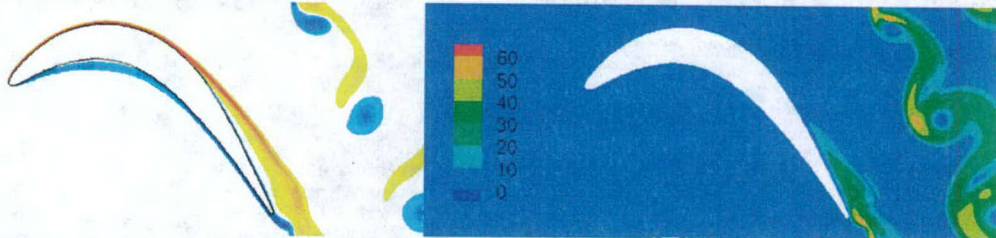
a) Low Reynolds number  $k-\omega$  model, Boussinesq-assumption,  $l_T=10^{-4}C_x$



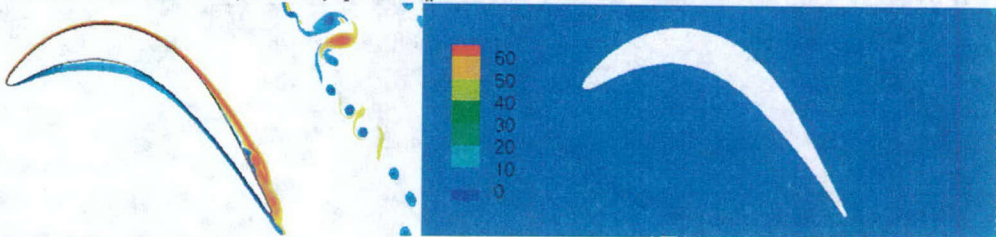
b)  $k-\omega$  model, EASM,  $l_T=10^{-4}C_x$



c)  $k-\omega$  model, EASM,  $l_T=10^{-3}C_x$



d) Low Reynolds number  $k-\omega$  model, EASM,  $l_T=10^{-4}C_x$



e) no turbulence modeling (laminar flow)

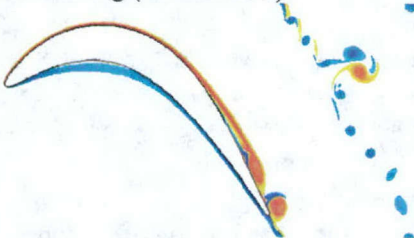


Fig. 2.12: Computation of entire cascade at design blade spacing,  $d/C_x=0.88$ . Iso-contours of left: spanwise vorticity,  $\omega_z$ , and right: eddy viscosity,  $\mu_T/\mu$ .

Much higher levels of eddy viscosity were found to be predicted when the turbulence intensity,  $Tu_\infty$ , was raised to 1% and the turbulence length scale,  $l_T$ , was set to 0.1% or 0.01% of the axial chord,  $C_x$ . Four cases were computed with 1998  $k-\omega$  turbulence model and one was



computed with the standard  $k-\varepsilon$  turbulence model (Wilcox 2000). Except for one case, where the Boussinesq-assumption was used in conjunction with the low Reynolds number terms, the EASM was employed.

Instantaneous visualizations of spanwise vorticity and eddy viscosity are shown in Fig. 2.12. Eddy-viscosity builds up in the recirculation region and in the wake. The low Reynolds number terms effectively lower the eddy-viscosity level. The largest separation bubble was predicted for case *c*. A somewhat smaller separation bubble was obtained for cases *a* and *b*. The model contribution was very small for all other cases and the flow appeared to be almost laminar. Obviously, the result is very dependent on the inflow turbulence quantities and on the model. The combination of Low Reynolds number  $k-\omega$  model with EASM predicts zero eddy viscosity, and can therefore be discarded. When EASM is employed more eddy viscosity is predicted in the separated flow region when compared to the result obtained with Boussinesq-assumption and low Reynolds number terms.

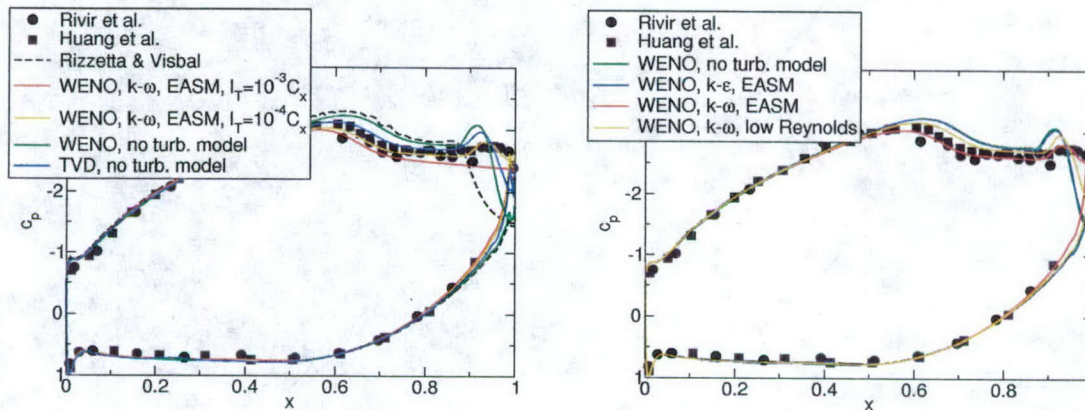


**Fig. 2.13:** Time-averaged wall pressure coefficient as measured by Rivir and co-workers and Huang *et al.* and computed by Rizzetta and Visbal. URANS results with different turbulence modeling approaches and varying inflow turbulence conditions compared with laminar results (TVD and WENO scheme). Figure on right-hand-side is for  $l_T=10^{-4}C_x$ .

The time-averaged wall pressure coefficient allows for a more qualitative comparison of the various cases (Fig. 2.13). The “hump” close to the trailing edge, which is the consequence of strong spanwise coherent structures present in the 2-D calculation, does not appear in the experimental data and was diminished when a more diffusive numerical scheme (the 2<sup>nd</sup>-order accurate symmetric TVD scheme) was employed. The addition of eddy viscosity by the various models (most noticeable for case *c*) lead to earlier separation and an increased pressure plateau in the separated region. The pressure distribution closest to the experimental data was



obtained with 1998  $k$ - $\omega$  turbulence model with EASM and an inflow turbulence length scale of  $l_T=10^{-4}C_x$  with  $Tu_\infty=1\%$ .

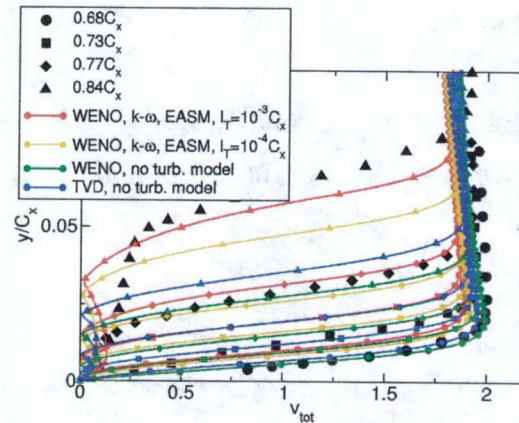


**Fig. 2.14: Wall normal profiles of total velocity taken at four different axial locations. Comparison with measurements by Rivir and co-workers.**

Wall normal profiles of total velocity are shown in Fig. 2.14. The size of the separation bubble was underpredicted in laminar computations with the less diffusive WENO scheme. When the more diffusive TVD scheme was employed a larger bubble and stronger recirculation were predicted. At the later stations of  $0.77$  and  $0.84C_x$  the best results were achieved with an inflow turbulence length scale of  $l_T=10^{-3}C_x$  and EASM. The boundary layer upstream of the separation at  $0.68C_x$  was only predicted correctly when no turbulence model was used. As expected, numerical diffusion or eddy viscosity introduced by the model thickens the boundary layer upstream of the separation. With the TVD scheme a slightly better match could be achieved. One may wonder if the assumption of a hydraulically smooth wall was justified and if the combination of surface roughness and inflow turbulence could sufficiently explain the differences between experiment and simulations. As the inflow turbulence length scale,  $l_T$ , was increased the boundary layer thickened. For  $l_T=10^{-3}C_x$ , the prediction was still in reasonable agreement with the experiment. However, additional numerical diffusion (additional diffusion can also be introduced by insufficient grid resolution) or turbulent mixing in the separated flow region also appear to strengthen the recirculation and increase the size of the separation bubble. One may conclude that the additional diffusion introduced by the model weakened the growth rate of the spanwise structures and thus weakened the wall normal mixing leading to a larger separation bubble and later reattachment. It appears likely that a similar mechanism



occurs in 3-D simulations where a secondary instability can set in and break up or weaken the intensity of the spanwise structures.

### 2.4.3 Three-dimensional simulations

For 3-D simulations the 2-D grid was extended in the spanwise direction by 64 cells. Following investigations by Rizzetta and Visbal (2003) the spanwise width of the computational domain was set to  $\Delta z=0.2$ .

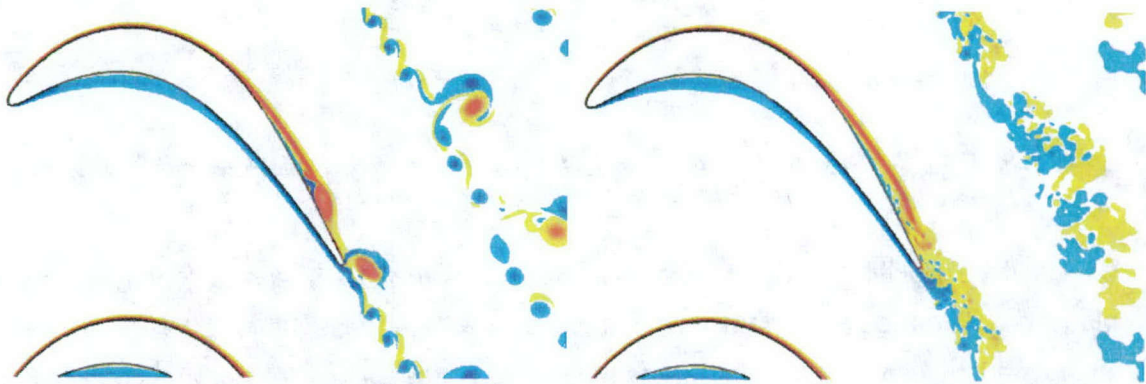


*Fig. 2.15: Instantaneous visualization of spanwise vorticity. Left: 2-D result and right: 3-D simulation (spanwise average). Results are for design blade spacing,  $d/C_x=0.88$ . The onset of 3-D turbulent motion close to the trailing edge weakens the spanwise coherent structures.*

Instantaneous visualizations of spanwise vorticity obtained from the 2-D and 3-D computations are shown in Fig. 2.15. In the 3-D simulation the separated boundary layer transitions before reattaching to the blade. The turbulent mixing significantly weakens the spanwise coherent structures (especially in the wake region of the blade). The length and thickness of the separation bubble does, however, appear to be almost unaltered. It should be noted that due to the extensive computational requirements of 3-D simulations, rigorous grid resolution studies have not been carried out yet. An instantaneous visualization of the flow structures using the Q-criterion (Hunt et al. 1988),

$$Q=0.5(W_{ij}W_{ij}-S_{ij}S_{ij}),$$

where  $W_{ij}=0.5(\partial v_i/\partial x_j - \partial v_j/\partial x_i)$  is the rotation rate and  $S_{ij}=0.5(\partial v_i/\partial x_j + \partial v_j/\partial x_i)$  is the strain rate, is shown in Fig. 2.16. A positive Q-criterion indicates areas where rotation dominates strain. The 2-D spanwise structures that periodically develop as a consequence of the shear layer



instability become unstable with respect to three dimensional perturbations. These disturbances initially cause a 3-D modulation of the 2-D structures, and eventually lead to a rapid breakdown to turbulence close to the trailing edge. (The question if the bubble is absolutely or convectively unstable is not being discussed here.) Although the wake is turbulent, the unsteady “footprints” of the two-dimensional shear layer instability can still be recognized. However, their strength is diminished due to the turbulent mixing. The predominant two-dimensionality of the flow over most of the blade explains why the  $c_p$ -curves for the 2-D and the 3-D cases shown in Fig. 2.16 are almost similar. The additional diffusion caused by the turbulent mixing weakens the spanwise structures. The “hump” near the trailing edge in the  $c_p$ -curve is diminished somewhat and shifted in downstream direction. A similar trend could be observed in the 2-D calculations when additional numerical diffusion was introduced by computing on a coarser grid (Fig. 2.7).

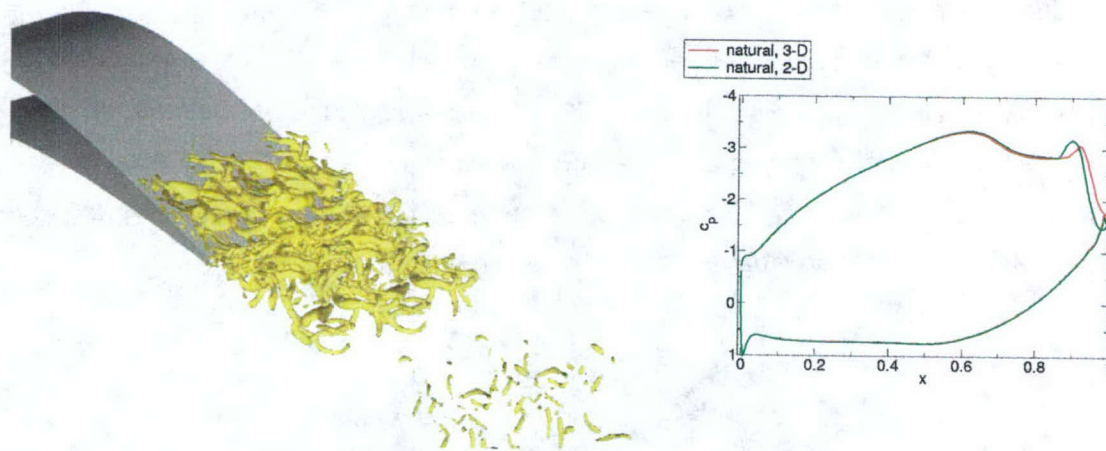


*Fig. 2.16: Instantaneous visualization of  $Q$ -criterion ( $Q=1000$ , domain was multiplied once in the spanwise direction and  $c_p$ -distribution. Results are for design blade spacing,  $d/C_x=0.88$ .*

Visualizations of the trailing edge region of the blades are shown in Fig. 2.17. Clearly, the spanwise structures are broken up and become three-dimensional. The flow transitions very shortly before reattaching. Since the difference between the 2-D and 3-D result was small and since 3-D simulations are almost prohibitively expensive it was decided to perform most of the Active Flow Control (AFC) investigations in sections 2.5 and 2.6 using 2-D calculations only.



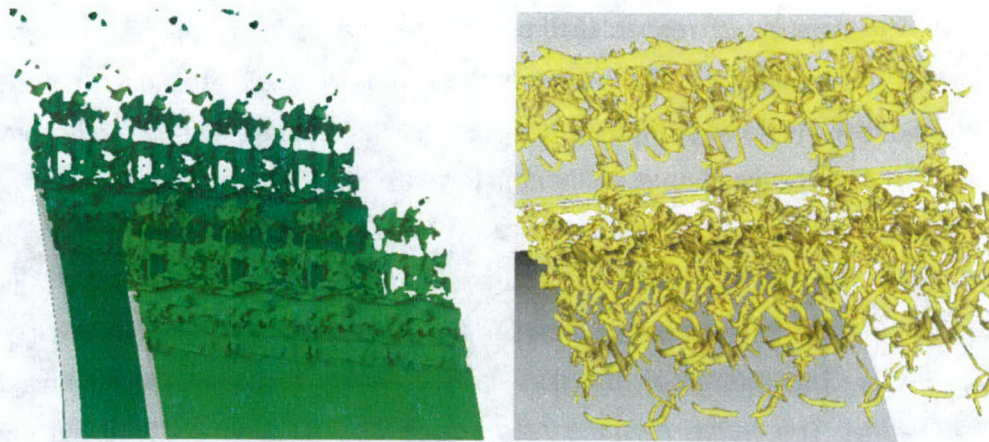


*Fig. 2.17: Simulation of entire cascade at design blade spacing,  $d/C_x=0.88$  (the computational domain was extended 3 times in the spanwise direction). Close-ups at trailing edge. Left: Iso-surface of axial velocity ( $u=0.3$ ) and right: iso-surface of  $Q$ -vortex criterion ( $Q=100$ ).*

To reduce the computational expense a 3-D ILES based on the more diffusive 2<sup>nd</sup>-order accurate upwind scheme was performed on a computational grid with a spanwise extent of  $\Delta z=0.1$  and 32 cells in the spanwise direction. The spanwise width of the domain was chosen to coincide with the VGJ hole spacing of a later AFC investigation. The 2<sup>nd</sup>-order accurate TVD scheme was chosen for the 3-D ILES because of its numerical diffusion properties (Margolin and Rider 2002) and because it gave reasonable 2-D results (Fig. 2.13).

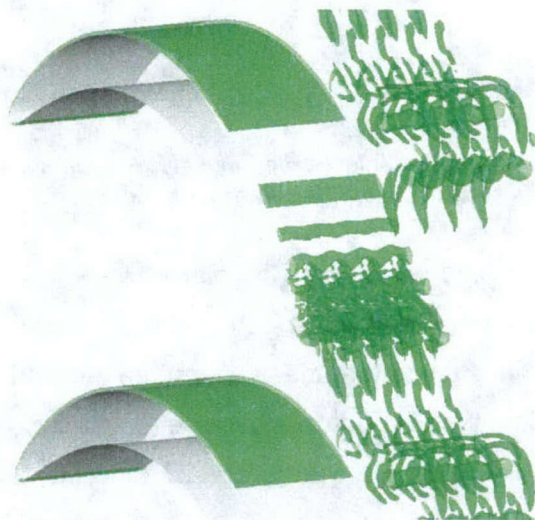


*Fig. 2.18: 3-D ILES. Iso-surface of  $Q$ -criterion ( $Q=100$ , the computational domain was extended 3 times in the spanwise direction). Uncontrolled natural flow.*

An instantaneous visualization of the  $Q$ -criterion for the uncontrolled natural flow obtained



from the 3-D ILES is shown in Fig. 2.18. The flow looks very similar to the earlier 3-D result obtained with the more accurate WENO scheme (Figs. 2.16 & 2.17). However, as a consequence of the larger numerical diffusion of the discretization, the structures are less fine-grain. Small scale turbulence motion is modeled implicitly. To get additional insight into the flow dynamics a Proper Orthogonal Decomposition (POD) of the time-dependent flow data was performed.

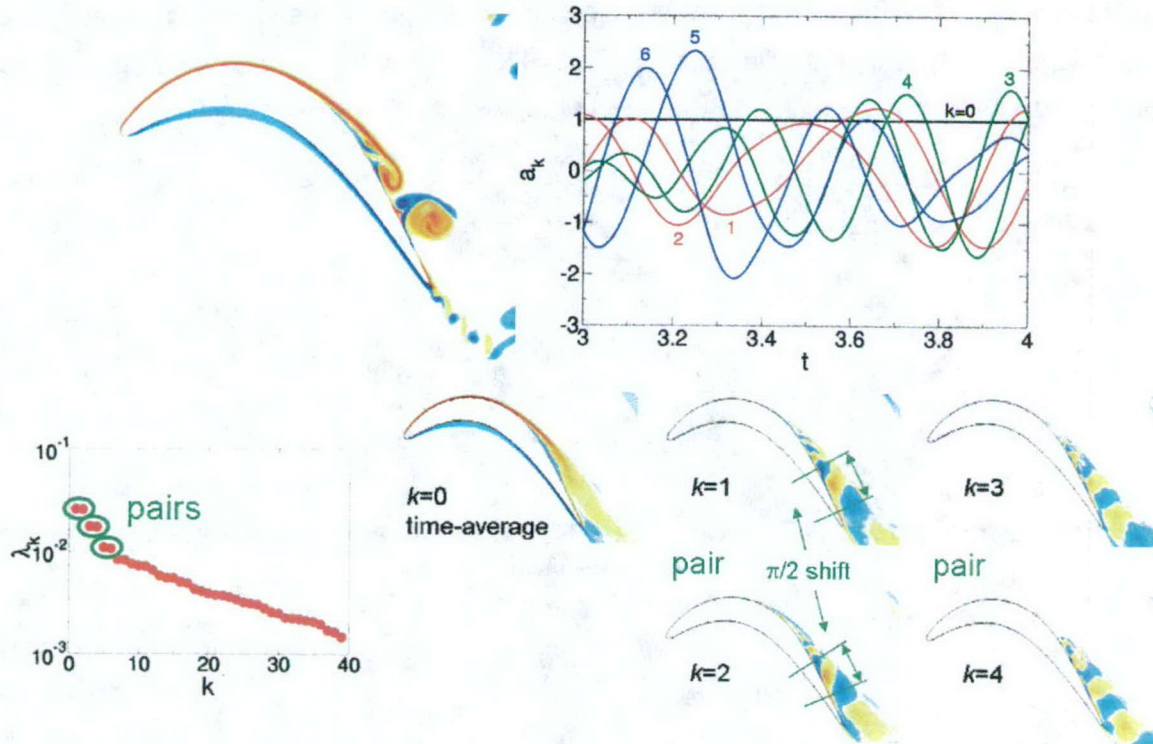


*Fig. 2.19: POD of 2-D flow data. Instantaneous visualization of spanwise vorticity, time-coefficients,  $a_k$ , eigenvalues,  $\lambda_k$ , and eigenmodes (iso-contours of spanwise vorticity).*

POD decomposes time dependent flow data,  $v(t)$ , into time-coefficients,  $a_k(t)$ , and eigenfunctions,  $q_k(x)$ ,

$$\vec{v}(\vec{x}, t) = \sum_k a_k(t) \vec{q}_k(\vec{x}).$$

The POD eigenvalues,  $\lambda_k$ , are a measure of the total kinetic flow energy contained in the respective POD mode,



$$(\vec{q}_k, \vec{q}_{k'}) = \delta_{kk'} \lambda_k.$$

POD is the modal decomposition that captures most of the kinetic energy of a flow with the least number of modes. POD modes that appear in pairs of equal eigenvalue size with eigenmodes and time-coefficients that show waves of similar wavelength with a phase difference of  $\pi/2$  describe traveling waves. As an example a POD of the time-dependent 2-D flow data is shown in Fig. 2.19. Mode 0 is the time-average of the data. Modes 1 & 2, 3 & 4, 5 & 6 form pairs and describe traveling waves. The time-coefficients describe almost harmonic functions indicating a very periodic vortex shedding. Modes 1 & 2 describe the primary vortex shedding. Modes 3 & 4 are higher harmonics of modes 1 & 2.

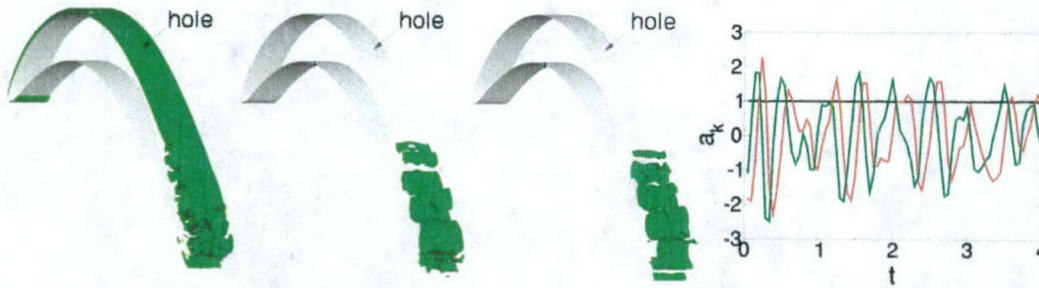


Fig. 2.20: 3-D ILES. POD of uncontrolled natural flow. Left to Right: POD eigenfunctions 0, 1, 2, and time-coefficients.

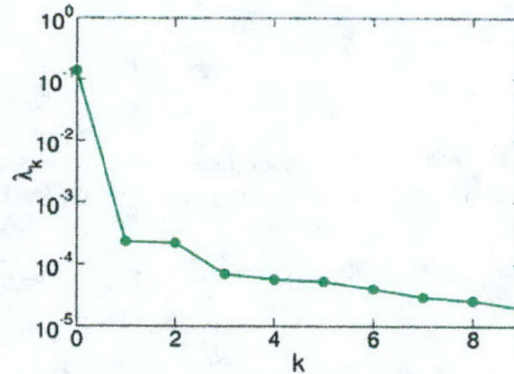


Fig. 2.21: 3-D ILES. POD of uncontrolled natural flow. POD eigenvalues.

The POD result of the time-dependent 3-D ILES data is shown in Figs. 2.20 & 2.21. Due to the limited amount of data available for the POD the eigenfunctions are not smooth and the time-coefficients are not well resolved in time. POD reveals the uncontrolled flow to be dominated by strong spanwise coherent structures. Three times more energy is contained in



modes 1 and 2 than in the higher modes (Fig. 2.21). The flow on the suction side of the blade is essentially 2-D. The oscillation frequency of the POD time-coefficients of modes 1 & 2 is relatively low, indicating slow moving and large spanwise coherent structures.

#### 2.4.4 Larger blade spacing

The blade spacing was increased by 25% ( $d/C_x=1.1$ ) to increase the size of the separation bubble, resulting in higher performance losses. The differences between the 2-D and 3-D results are dramatic (Fig. 2.22). The strong spanwise coherent structures present in the 2-D simulation are not visible in the 3-D simulation. These spanwise structures appear to immediately break up into small scale turbulent motion. This is in stark contrast to the 3-D simulation for the design blade spacing (Fig. 2.15), where the flow transitions very close to the trailing edge.

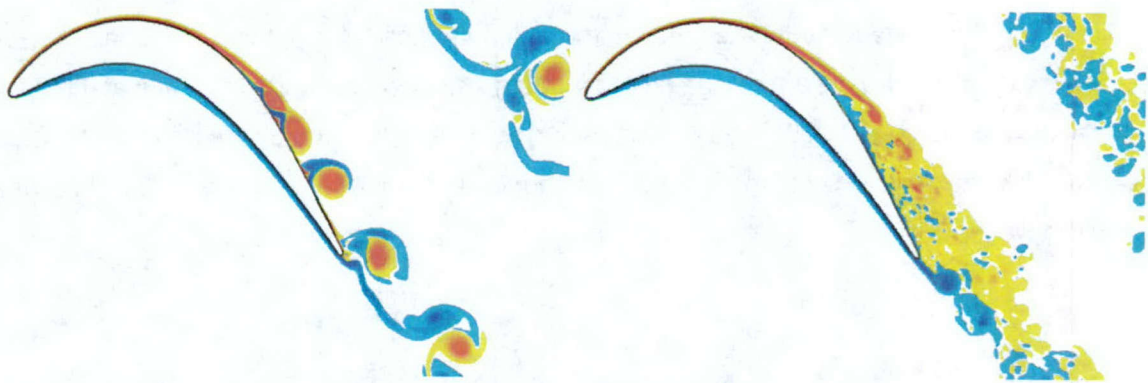


*Fig. 2.22: Instantaneous visualization of spanwise vorticity. Left: 2-D result and right: 3-D simulation (spanwise average). Results are for 25% larger blade spacing,  $d/C_x=1.1$ .*

A different visualization of the 3-D result and a comparison of the wall pressure distribution with the 2-D calculation are shown in Fig. 2.23. As for the URANS calculations in the previous chapter, weakening of the spanwise coherent structures leads to a larger separation bubble with earlier separation and a higher pressure plateau. The strength of the “hump” close to the trailing edge, which can be associated with strong spanwise coherent structures, is reduced considerably. From these results one may conclude that spanwise structures are a very efficient means for separation control. Excitation and/or strengthening of these structures by AFC may significantly reduce the amount of flow separation and improve performance.



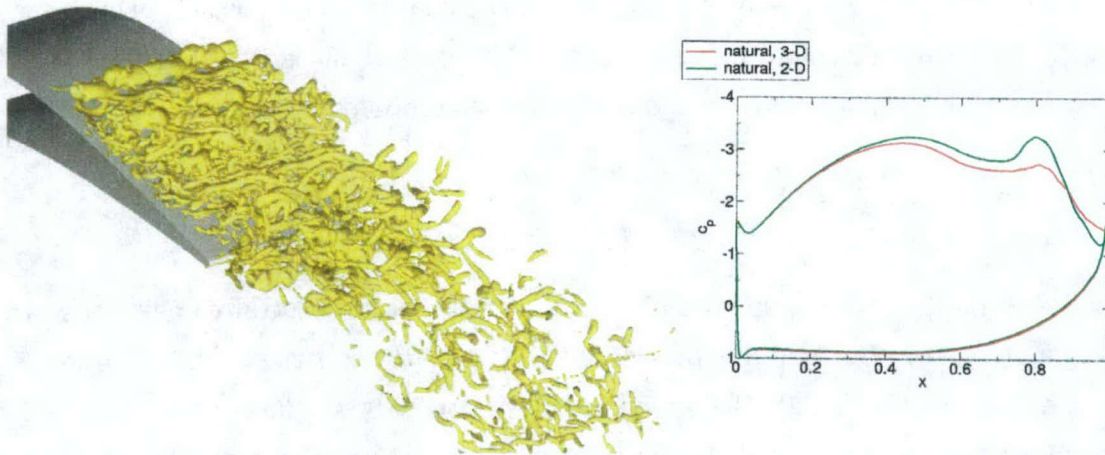


*Fig. 2.23: Instantaneous visualization of  $Q$ -criterion ( $Q=1000$ , domain was multiplied once in the spanwise direction) and  $c_p$ -distribution. Results are for 25% larger blade spacing,  $d/C_x=1.1$ .*

#### 2.4.5 Periodic passing wake

Finally, preliminary results are shown from simulations where the LPT cascade was subjected to periodic upstream wakes by prescribing a time-periodic wake profile at the inflow boundary (Xiaohua et al. 1999). The wake spacing was chosen to match the original LPT blade spacing. The lateral velocity of the wakes was chosen to be 1.2 the inflow velocity. The wake half-width was  $0.05C_x$ .



*Fig. 2.24: Iso-contours of spanwise vorticity. Left: without passing wakes and right: with passing wakes. Results are for 25% larger blade spacing  $d/C_x=1.1$*



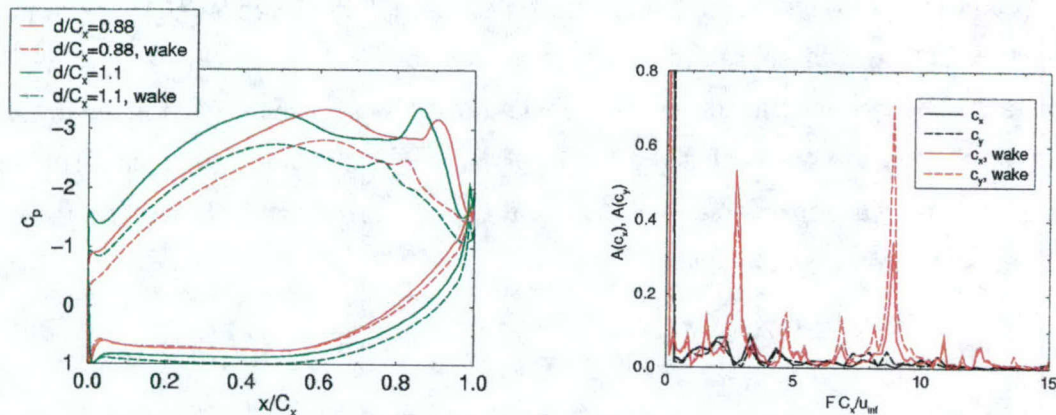


**Fig. 2.25: Calculations with and without passing wakes. Left: time-averaged pressure coefficient and right: frequency spectra of aerodynamic coefficients for design blade spacing  $d/C_x=0.88$ .**

A comparison of the cascade flow with and without wake is given in Fig. 2.24. The passing wakes periodically excite the boundary layers on the suction and the pressure side. In the temporal average, the passing wakes lower the free stream velocity. The length of the separation region is shortened (Fig. 2.25) and a larger pressure recovery is achieved, indicating an earlier boundary layer reattachment. The passing wakes have a similar effect on the flow separation as AFC by pulsed blowing (see section 2.5). However, in contrast to pulsed blowing by AFC the passing wakes excite two frequencies simultaneously and act on both sides of the blade. The results are indeed preliminary and extensive computations are required to assess the effect of passing wakes and in particular the effect of AFC.

## 2.5 Open-loop control

### 2.5.1 Set-up of 2-D flow actuation

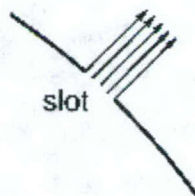


**Fig. 2.24: Forcing slot for 2-D calculations.**

For 2-D calculations with Active Flow Control (AFC) a 3 cell wide forcing slot was positioned upstream of the separation (at  $0.645 \leq x/C_x \leq 0.655$  (for the design blade spacing) and  $0.573 \leq$



$x/C_x \leq 0.583$  (for the 25% increased blade spacing)). The slot width was  $b=0.01 C_x$ . Blowing with an amplitude  $Bv_\infty f(t)$  was applied in wall normal direction (Fig. 2.24), where  $B=v_{jet}/v_\infty$  is the blowing ratio. The blowing amplitude was constant over the slot width. The forcing frequency,  $F^+$ , was non-dimensionalized with free stream velocity,  $v_\infty$ , and chord,  $C_x$ . The non-dimensional period,  $T$ , is defined as the inverse of  $F^+$ . The duty cycle,  $\tau$ , is defined as the ratio of jet on-time to off-time. A square forcing function

$$\begin{aligned} f(t) &= 1 \text{ if } 0 \leq t < \tau T \\ f(t) &= 0 \text{ if } \tau T \leq t < T \\ f(t+T) &= f(t) \end{aligned}$$

was used (Fig. 2.25).

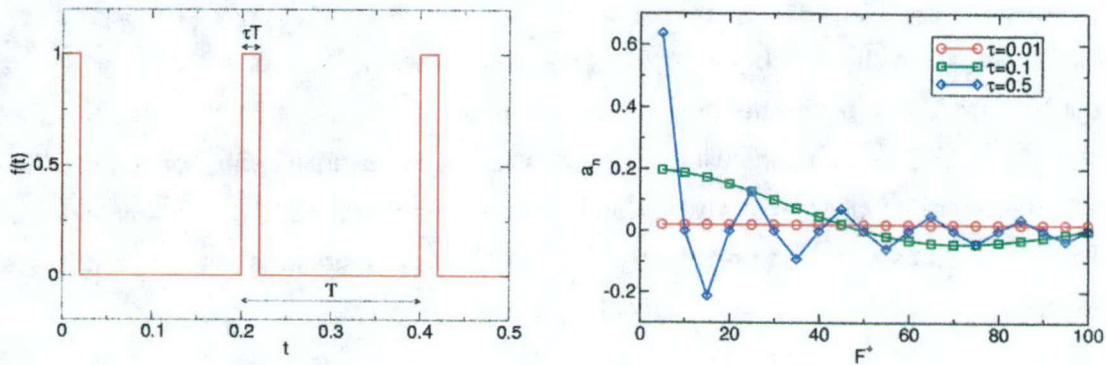
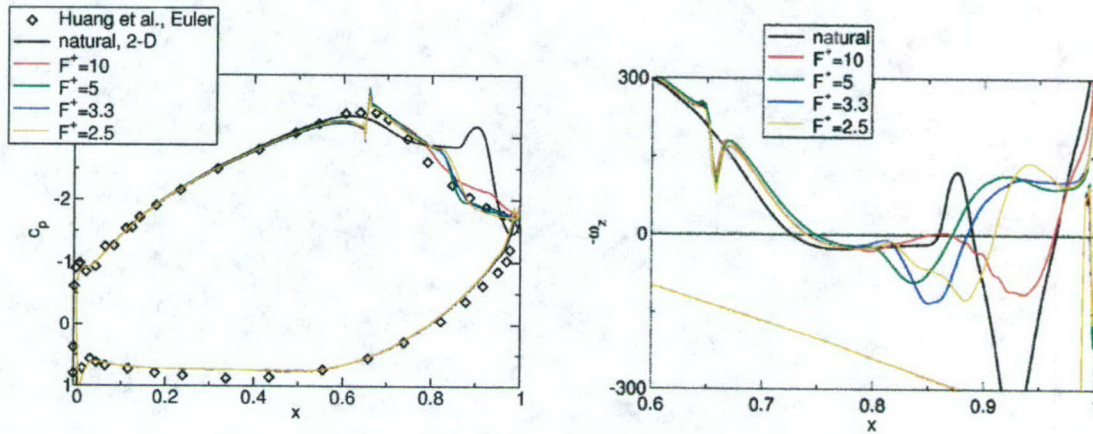


Fig. 2.25: Left: Square forcing function  $f(t)$  with period  $T=0.2$  ( $F^+=5$ ) and duty cycle  $\tau=0.1$  and right: frequency spectra of forcing function for  $F^+=5$  and various duty cycles.

Frequency spectra of the forcing function for different duty cycles,  $\tau$ , are shown in Fig. 2.25. As the duty cycle approaches very small values the amplitude drop-off toward higher frequencies (or alternatively shorter periods) becomes smaller, meaning that for smaller duty cycles higher frequencies are forced at comparatively larger amplitudes (the frequency spectra become flatter). Also noteworthy is that for a duty cycle of  $\tau=0.5$  only uneven multiples of  $F^+$  are forced. For  $\tau=0.1$  modes  $n=10, 20, \dots$  are zero. Arguably, a perfect square forcing function can never be achieved in the experiment. However, the square forcing function used in the experiments by Rivir and co-workers at AFRL should exhibit similar properties. For the controlled cases presented in this section, a blowing ratio of  $B=1$  and a duty cycle of  $\tau=0.1$  were chosen. The momentum coefficient,  $c_\mu = b/C_x \tau B^2$ , was  $10^{-3}$ .



## 2.5.2 Results for design blade spacing



**Fig. 2.26:** Left: Time-averaged wall pressure coefficient and right: wall vorticity. Results are for design blade spacing,  $d/C_x=0.88$ . Included are measurements by Huang et al. and data for the natural uncontrolled flow.

In the uncontrolled case, the flow separated at  $x \approx 0.73C_x$  and reattached at  $x \approx 0.95C_x$  (Fig. 2.26). A small secondary separation bubble was located at  $0.86 \leq x/C_x \leq 0.89$ . The flow was then controlled by pulsed blowing through a slot. Four different non-dimensional forcing frequencies,  $F^+$ , were explored. When the flow was forced, separation was delayed (Fig. 2.26) and the wall pressure distribution approached the inviscid solution (Huang et al. 2003), indicating very little or no flow separation. The smallest separation was obtained for  $F^+=5$ . One should keep in mind that, with the square forcing function chosen, higher harmonics were forced as well.



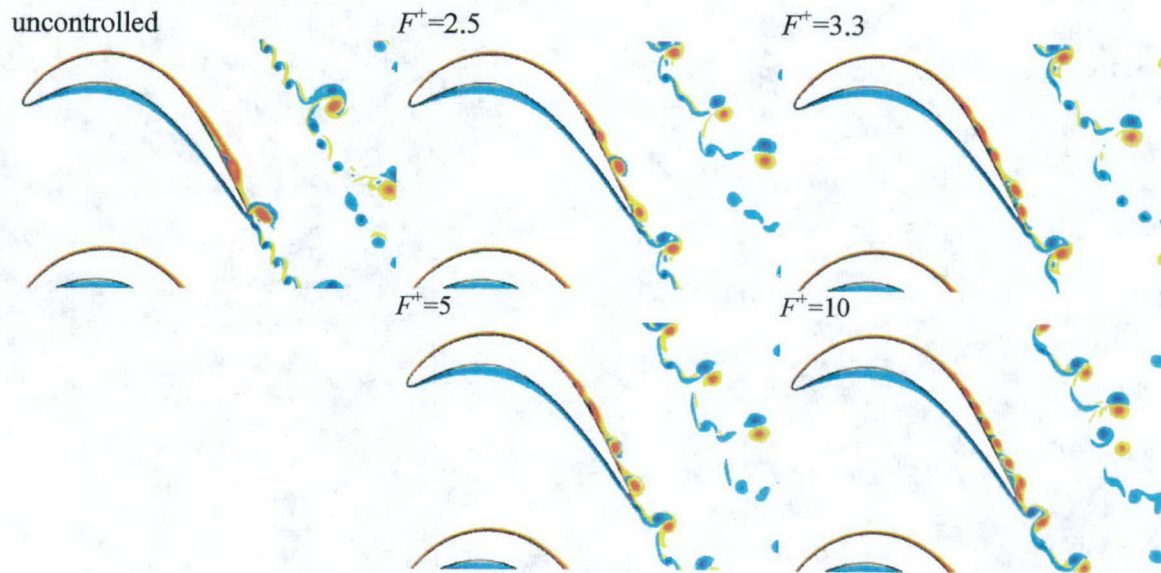


*Fig. 2.27: Instantaneous visualization of spanwise vorticity for the design blade spacing,  $d/C_x=0.88$ .*

Instantaneous visualizations of the different cases are shown in Fig. 2.27. As a consequence of the forcing spanwise structures emerge farther upstream and appear to be more organized. For higher forcing frequencies the spacing of the structures is reduced. Also, vortex merging is visible in all instances. To more quantitatively assess the dynamics of the flow, wall vorticity was Fourier-decomposed in time.

Fig. 2.28 shows the time evolution of wall vorticity for the uncontrolled case and the controlled case with  $F^+=5$ . Light shaded areas represent regions of low wall shear stress. In the uncontrolled case, spanwise structures form in a very regular fashion downstream of  $0.87C_x$ . When the wall vorticity is Fourier transformed in time the regularity of these spanwise structures becomes visible as a pronounced amplitude peak at  $F^+\approx 3.3$ .

The controlled flow displays a very regular vortex shedding at the forcing frequency. The flow “locks in” to the forcing. Both the forcing signal and its higher harmonic are amplified. The higher harmonic reaches its maximum amplitude before the fundamental. This agrees well with stability theory. The oscillation period of disturbances that experience maximum amplification is proportional to the shear layer thickness. With forcing, the frequency spectrum becomes very regular.



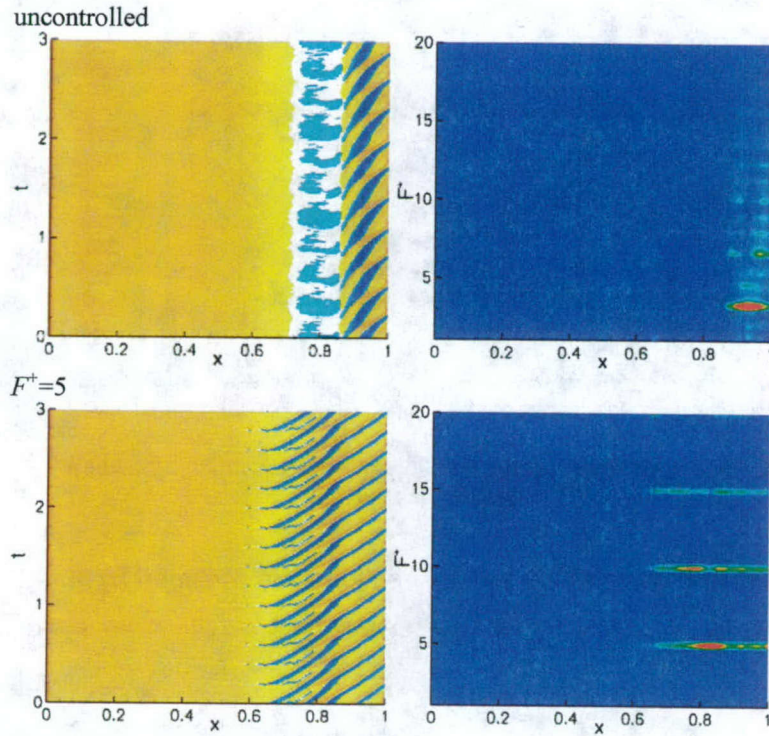


**Fig. 2.28:** Design blade spacing,  $d/C_x=0.88$ . Wall vorticity on suction side of blade. Left: Time-evolution ( $\omega_t=-1200\dots1200$ ) and right: Fourier transform ( $A(\omega)=0\dots400$ ).

It should be noted that each forcing pulse also generates an upstream traveling acoustic wave (visible in the  $x$ - $t$  graphs in Fig. 2.28). Pulsed forcing with a square forcing function does not only simultaneously excite a large number of frequencies (which is practical from an engineering point of view because it makes forcing at the “right” frequency more likely) but also generates strong acoustic waves and thereby transports the disturbance signal upstream of the forcing slot. From a scientific point of view, it would rather be desirable to force one frequency only (harmonic forcing) to obtain a clearer understanding of the relationship between the forcing frequency and the flow response.



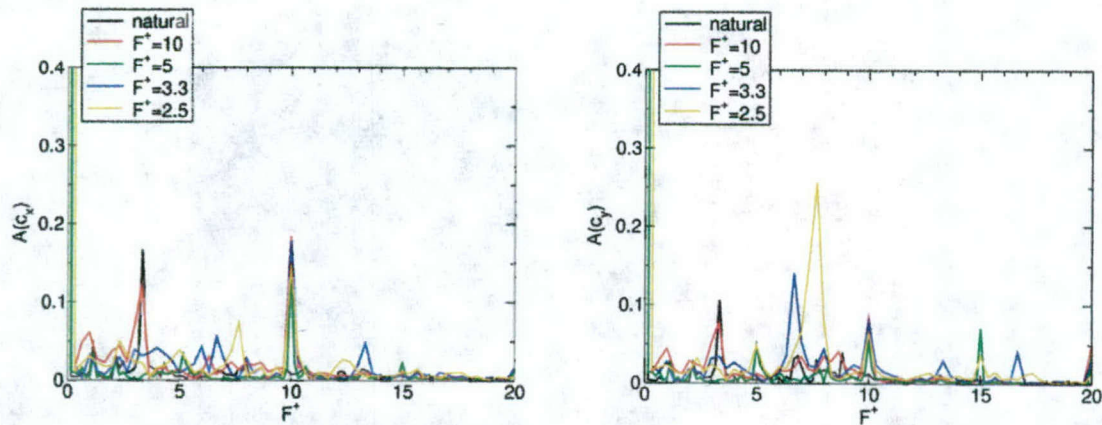


Fig. 2.29: Fourier transforms of aerodynamic coefficients  $c_x$  and  $c_y$ . Results are for design blade spacing  $d/C_x=0.88$ .

The aerodynamic coefficients in  $x$ - and  $y$ -direction were obtained by non-dimensionalizing the aerodynamic forces,  $F_x$  and  $F_y$ , by the free stream dynamic pressure, the chord,  $C_x$ , and the unit span,

$$c_{x,y} = F_{x,y} / (C_x 0.5\rho_\infty v_\infty^2) .$$

$F_x$  and  $F_y$  were calculated by integrating the pressure and friction forces over the entire blade surface. Fourier transforms of the aerodynamic coefficients in time are shown in Fig. 2.29. The frequency spectra of the forced cases are more discrete than the frequency spectrum of the uncontrolled case. The uncontrolled case shows a frequency peak at  $F^+ \approx 3.3$ . When the flow was forced at  $F^+ = 10$  the separated shear layer was first dominated by  $F^+ = 10$ . Close to the leading edge the subharmonic  $F^+ = 3.3$  became stronger than the fundamental. This process can be interpreted as vortex merging. When the flow was forced at  $F^+ = 3.3$ , the higher harmonic  $F^+ = 6.7$  was most amplified; When the flow was forced at  $F^+ = 2.5$ , the higher harmonic  $F^+ = 7.5$  was most amplified. The frequency the controlled flow appeared to be most unstable to was close to  $F^+ = 7.5$ . If the flow had been forced with this forcing frequency, the disturbances would possibly have been most amplified, leading to a very effective flow control. This frequency is noticeably higher than the predominant frequency of the uncontrolled flow,  $F^+ = 3.3$ . As one might expect, the frequency that the flow is most unstable to is related to the inverse of the separation bubble length. The mean bubble size is smaller in the controlled case. On the other hand, forcing at the frequency the flow is most unstable to may yield very high dynamic aerodynamic loads.



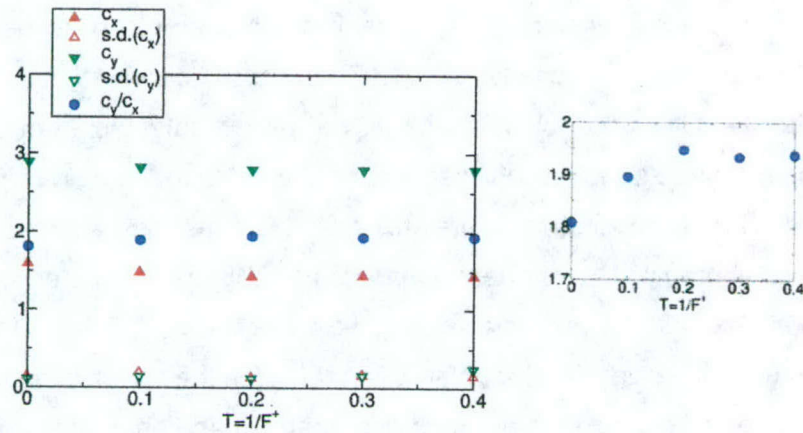


Fig. 2.30: Time averaged aerodynamic coefficients  $c_x$  and  $c_y$ . Results are for design blade spacing,  $d/C_x=0.88$ .

Time-averages of the aerodynamic coefficients are shown in Fig. 2.30. The 3-D result was not included since the computed time period was too small for obtaining reasonable time-averages. For all forced cases a gain in  $c_y/c_x$  was obtained. The largest gain (almost 7.7%) was achieved for  $F^+=5$ .

### 2.5.3 Results for 25% larger blade spacing

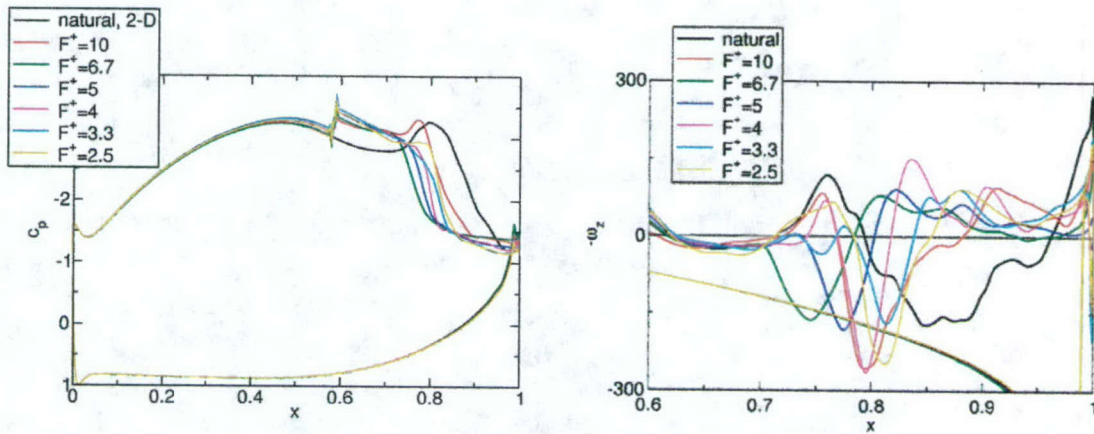
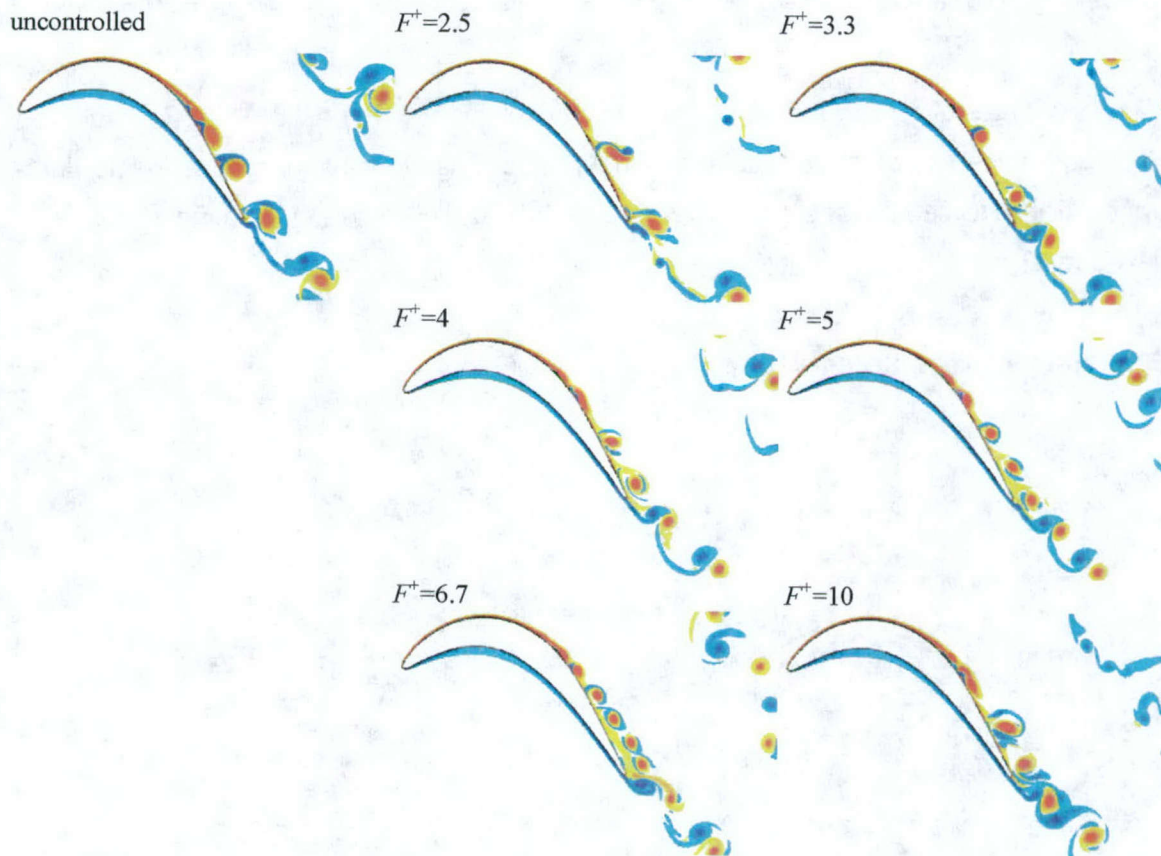


Fig. 2.31: Left: Time-averaged wall pressure coefficient and right: wall vorticity. Results are for 25% larger blade spacing,  $d/C_x=1.1$ .

When the blade spacing is increased by 25% the area enclosed by the  $c_p$ -curve (Fig. 2.31) is larger than at the design blade spacing since each individual blade has to exert a larger



aerodynamic force on the flow. As mentioned earlier, 3-D simulations are currently too expensive for AFC parameter studies. For the sake of comparability with the results presented for the design blade spacing, the feasibility of AFC by pulsed blowing was again demonstrated in 2-D calculations. Since 2-D calculations do not permit small scale turbulent motion, the strength of the spanwise structures is over-predicted and the following results should therefore be considered to be of a qualitative nature only. For all forced cases, the mean separation could be reduced considerably. The shortest separation bubble was obtained when the flow was forced at  $F^+=6.7$ . Visualizations of spanwise vorticity are shown in Fig. 2.32. Except for forcing with  $F^+=2.5$  and 10, the size of the structures is reduced in the mean when compared with the uncontrolled case, indicating a thinner time-averaged separation bubble and shear layer.



*Fig. 2.32: Instantaneous visualizations of spanwise vorticity. Results are for 25% larger blade spacing,  $d/C_x=1.1$ .*



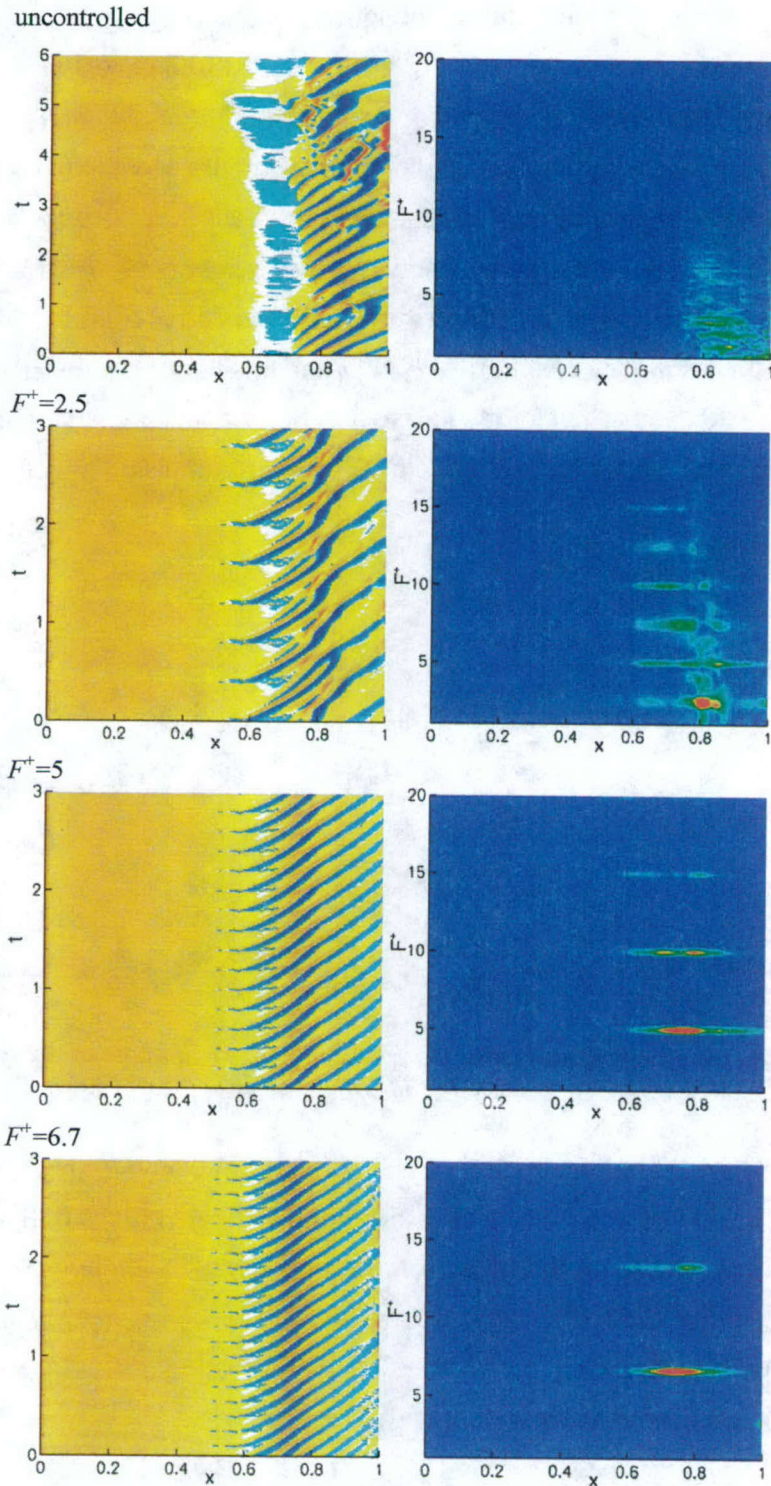


**Fig. 2.33: Wall vorticity on suction side of blade. Left: Time-evolution ( $\omega_t = -1200 \dots 1200$ ) and right: Fourier transform ( $A(\omega) = 0 \dots 400$ ). Results are for 25% larger blade spacing,  $d/C_x = 1.1$ .**



The frequency spectrum of the natural, uncontrolled case (Fig. 2.33) is very broad when compared with the result for the design blade spacing (Fig. 2.28). The wall vorticity  $x$ - $t$  diagram shows little regularity. More energy is contained in the lower frequency range of the spectrum than for the design blade spacing. The separation bubble and the associated length scales are larger. When the forcing frequency was chosen "properly", the flow "locked in" to the forcing frequency. The wall vorticity  $x$ - $t$  diagrams show a periodic response which is confirmed by distinct peaks in the frequency spectra. When the flow was forced at  $F^+=6.7$  or its subharmonic  $F^+=3.3$ , the peak in the frequency spectrum at  $F^+=6.7$  became very pronounced (Fig. 2.34). The forcing frequency  $F^+=2.5$  was too low for the flow to fully "lock in" to it, again resulting in a broad frequency spectrum. The higher harmonics, e.g.  $F^+=5$ , were amplified less than when being forced separately.

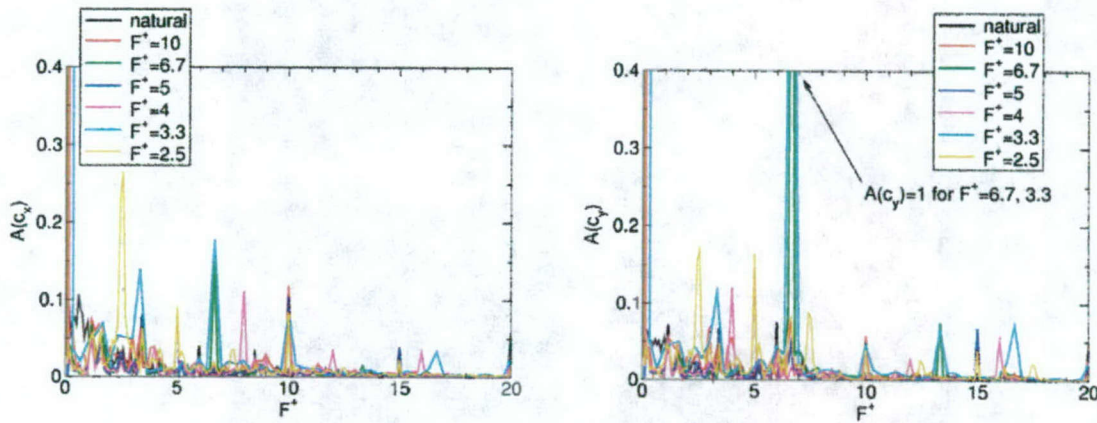
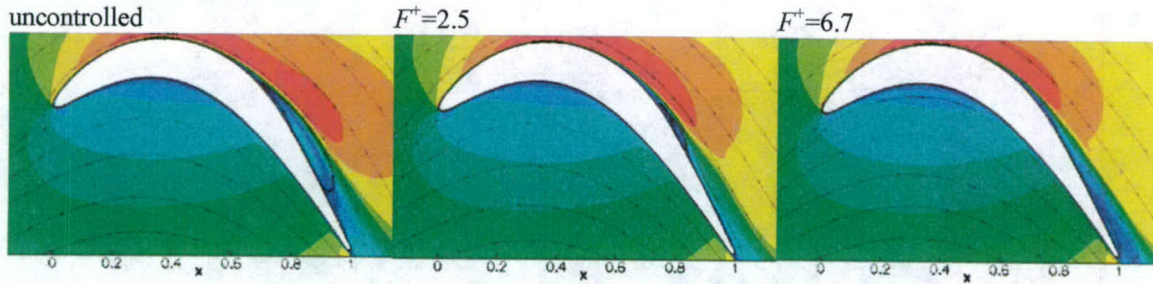


Fig. 2.34: Fourier transforms of aerodynamic coefficients  $c_x$  and  $c_y$ . Results are for 25% larger blade spacing,  $d/C_x=1.1$ .

The response of the flow to forcing at  $F^+=6.7$  or its subharmonic  $F^+=3.3$  is very pronounced (Fig. 2.34). This may be of importance when considering later practical application. Large unsteady aerodynamic forces on the blade may be undesirable. Temporal averages of total velocity are shown in Fig. 2.35. The large separation bubble of the uncontrolled flow seems totally removed when the flow was forced with  $F^+=6.7$ . For forcing with  $F^+=2.5$  the size of the separation bubble was considerably reduced.





*Fig. 2.35: Time-averaged data. Iso-contours of total velocity and streamlines. Results are for 25% larger blade spacing,  $d/C_x=1.1$ .*

Again, as measure for the increase in aerodynamic efficiency the ratio of the aerodynamic forces in y- and x-direction was studied (Fig. 2.36). This ratio is also a measure for the total flow turning angle.

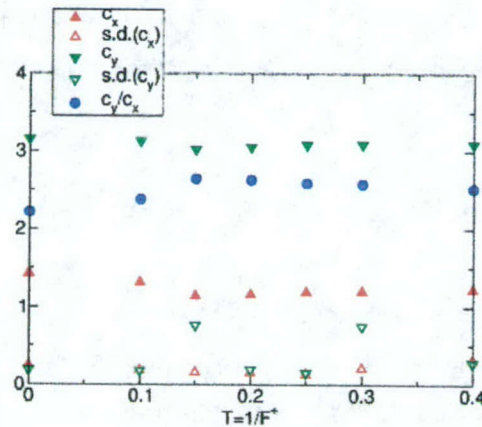


*Fig. 2.36: Time averaged aerodynamic coefficients  $c_x$  and  $c_y$ . Results are for 25% larger blade spacing,  $d/C_x=1.1$ .*

The largest gain in aerodynamic performance (about 19.4%) was achieved for  $F^+=6.7$ . However, for that forcing frequency, the dynamic aerodynamic loads on the blade reached very high levels. When the flow was forced at  $F^+=5$ , the fundamental and its higher harmonic were both close to the most amplified frequency of the controlled flow. Both were amplified, but not as much as when the flow was forced at the frequency for which it was most unstable. The loss in aerodynamic gain that was incurred by not forcing at the optimum frequency was very small. In fact, the gain in aerodynamic performance was still 18.7%. However, the dynamic loads were reduced considerably.



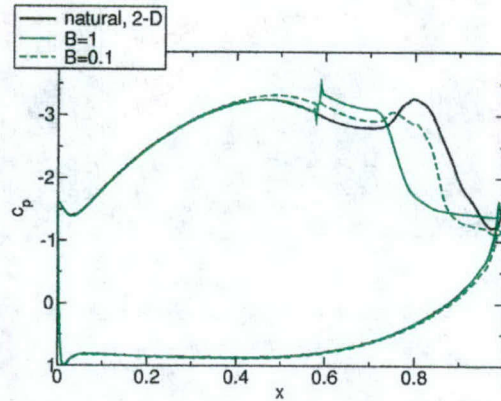


*Fig. 2.37: Time-averaged wall pressure coefficient. Comparison of uncontrolled result with controlled cases,  $F^+=6.7$ ,  $\tau=0.1$ , for two different blowing ratios,  $B$ . Results are for blade spacing  $d/C_x=1.1$ .*

Finally, the blowing ratio,  $B$ , for forcing with  $F^+=6.7$  was reduced by a factor of 10 (Fig. 2.37), leading to an immediate loss of control effectiveness and hence reduction of aerodynamic efficiency,  $c_y/c_x$ , from 19.4% ( $B=1$ ) to 10.2% ( $B=0.1$ ). The pressure distribution approached the shape of the uncontrolled flow.

#### 2.5.4 Pulsed Vortex Generator Jets (VGJs)

Pulsed vortex generator jets for open-loop separation control were explored in 3-D ILES simulations. A higher-order accurate simulation of pulsed VGJs for LPT blades was previously performed by Rizzetta and Visbal (2004). Jet pitch and skew angle were chosen as in the experiments by Rivir and co-workers (Fig. 2.38).

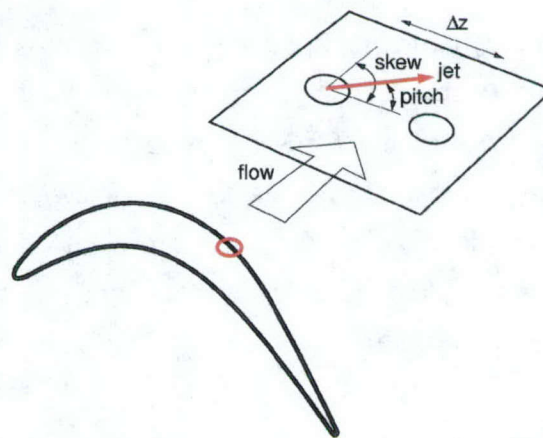


*Fig. 2.38: VGJ pitch angle ( $30^\circ$ ) and skew angle ( $90^\circ$ ) for 3-D ILES.*



Simulations were performed with small holes (5 cells long and 4 wide) and large holes (7 by 6 cells) located at 65% axial chord. The hole spacing was  $\Delta z=0.1$  and identical to the spanwise width of the computational domain. The ratio of hole spacing to diameter was about 8 for the small holes and 5.3 for the large holes. Parabolic velocity profiles were prescribed at the jet exit holes. The flow was forced at a preset frequency,  $F^+=5$ , and blowing ratio (defined as maximum jet exit velocity to inflow velocity),  $B=2$ , with a square forcing function and 10% duty cycle. The corresponding momentum coefficients,  $c_{\mu}$ , were  $8.9 \cdot 10^{-4}$  for the small holes and  $1.9 \cdot 10^{-3}$  for the large holes.

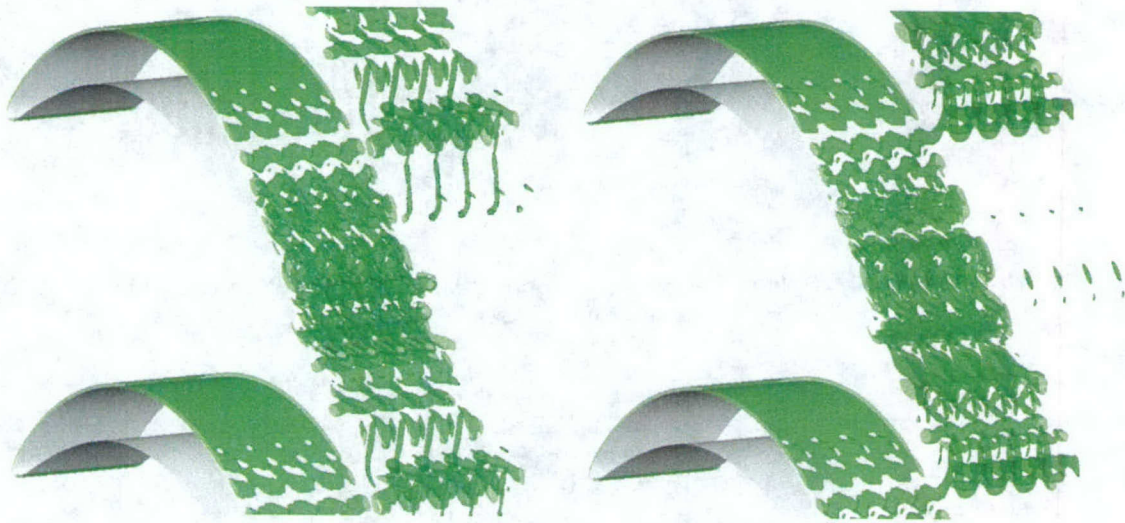


*Fig. 2.39: 3-D ILES. Iso-surface of  $Q$ -criterion ( $Q=100$ ). Controlled flow. Left: Small holes and right: large holes.*

The controlled flow is shown in Fig. 2.39 (compare to uncontrolled flow, Fig. 2.18). Qualitatively, results for small and large holes look very similar. In the controlled case, both streamwise and spanwise disturbances are introduced at non-linear amplitudes by the pulsed VGJ actuation. The flow transitions shortly downstream of the jet exit holes. A POD of the data was performed to further substantiate these statements.



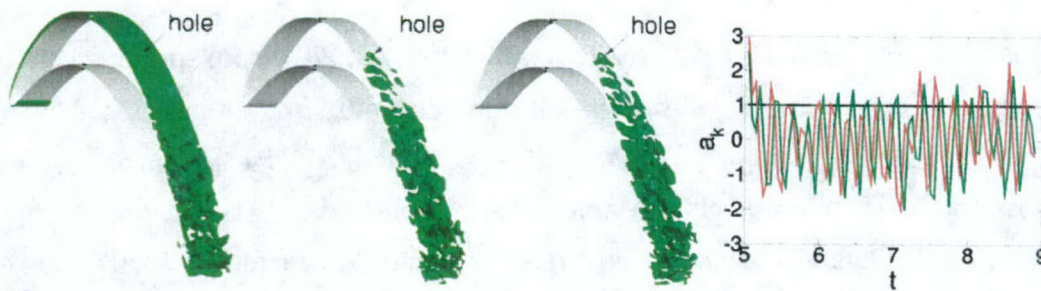


Fig. 2.40: 3-D ILES. POD of controlled flow (small VGJ holes). Left to Right: POD eigenfunctions 0, 1, 2, and time-coefficients.

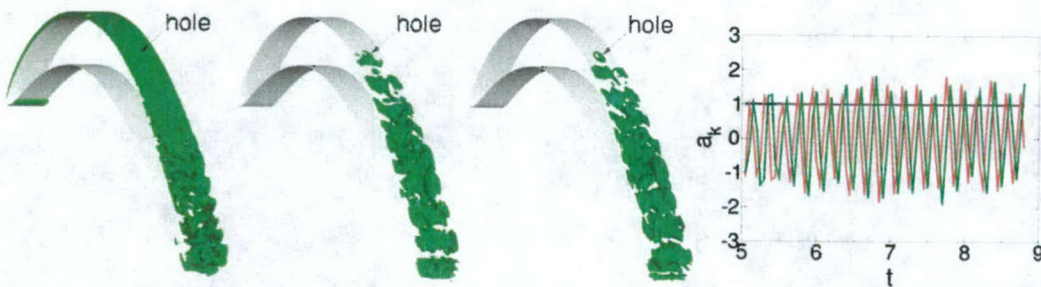


Fig. 2.41: 3-D ILES. POD of controlled flow (large VGJ holes). Left to Right: POD eigenfunctions 0, 1, 2, and time-coefficients.

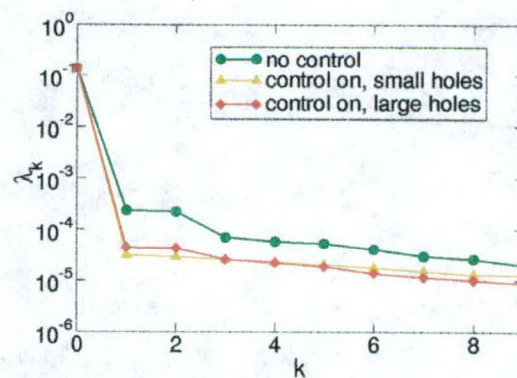


Fig. 2.42: 3-D ILES. POD eigenvalues for uncontrolled and controlled (pulsed VGJs) flow.

In the controlled case, less energy is contained in the unsteady POD modes (and slightly more energy is in the temporal mean) when compared with the uncontrolled case (Fig. 2.42) (PODs of the controlled cases were performed for  $t > 5.05$  to exclude the initial flow adjustment to the control.) Also, the energy distribution of the unsteady POD modes is flatter, indicating less dominant coherent structures. Accordingly, the oscillation amplitudes of the aerodynamic coefficients are reduced as the control becomes effective (Figs. 2.40 & 2.41). The oscillation



frequency of POD modes 1 & 2 corresponds to the VGJ pulsing frequency. For the large jet exit holes, modes 1 & 2 do in fact show some spanwise coherence close to the trailing edge (Fig. 2.41) which can be associated with a larger 2-D mode energy contents (larger eigenvalues  $\lambda_1$  &  $\lambda_2$ , Fig. 2.42).

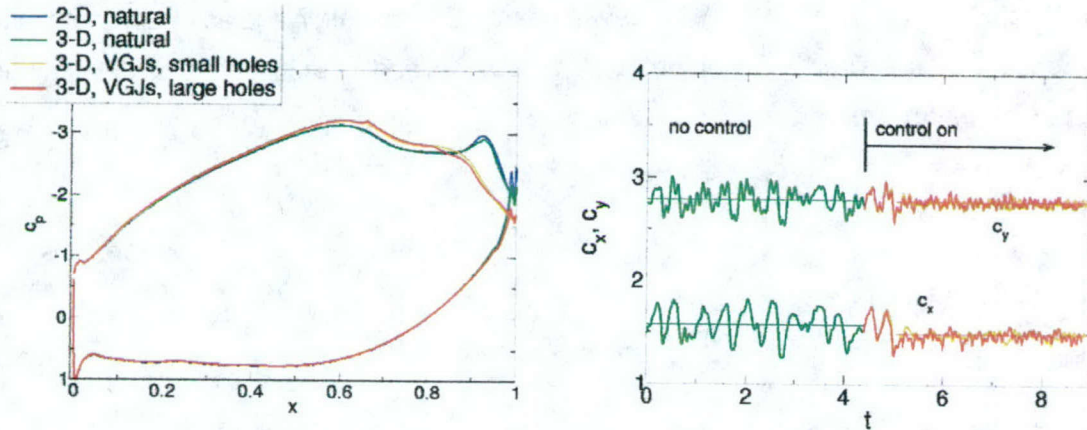


Fig. 2.43: 3-D ILES. Left: Time-averaged wall pressure coefficient and right: aerodynamic coefficients.

The controlled flow separates only insignificantly later than the uncontrolled flow. The “hump” close to the trailing edge disappears (Fig. 2.43). As a measure of the improvement in aerodynamic performance, the ratio of the aerodynamic coefficients,  $C_y/C_x$ , was estimated from their time-averages. This ratio was 1.771 in the uncontrolled natural case. With pulsed VGJs and small holes it could be raised to 1.875 (which corresponds to a 5.9% gain relative to the uncontrolled case) and 1.887 (6.6% gain) for the large holes. The maximum gain obtained in the 2-D calculations with pulsed forcing through a slot was 7.7% (section 2.5.2).

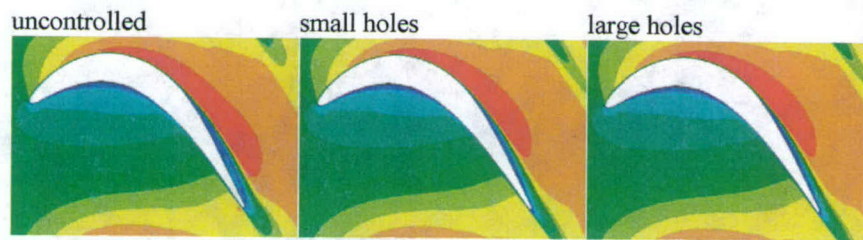


Fig. 2.44: 3-D ILES. Time and spanwise averages of total velocity.

Time-averages of total velocity are shown in Fig. 2.44. The separation bubble does not disappear as a consequence of the forcing. Instead it becomes narrower, indicating smaller structures in the shear layer. It should be kept in mind that for the current simulations a low-



order accurate numerical discretization was deliberately chosen to model unresolved small scale turbulent motion. When compared to highly resolved and detailed simulations (Postl et al. 2004) the relevant fluid dynamics in the vicinity of the jet exit holes appear not to be captured in the current 3-D ILES simulations. In the better resolved simulations it was found that this particular kind of forcing triggered the generation of hair pin vortices, thereby "by-pass" transitioning the flow (Morkovin 1969). However, despite the resolution and accuracy limitations the net result of the pulsed VGJ actuation, namely the early transitioning of the flow, is reproduced in the current ILES results (Fig. 2.39).



### **3. DIRECT NUMERICAL SIMULATIONS OF LAMINAR SEPARATION BUBBLES AND ACTIVE FLOW CONTROL USING VORTEX GENERATOR JETS**

In this second approach, we focused our investigations on a simpler flow, namely laminar separation bubbles on a flat plate. By simulating this prototypical model geometry, we were able to perform more detailed investigations of the fundamental physical mechanisms associated with laminar boundary layer separation and its control. Available computational resources could be concentrated in the regions of primary interest. As a consequence, the increased resolution (compared to the simulations of the "full" turbine cascade) allowed us to extract the physics associated with low Reynolds number separation control using vortex generator jets.

Section 2.1 briefly describes the Navier-Stokes code that was used for the present investigations. In addition, we summarize the progress that we made in the past three years regarding code development. In sections 2.2 and 2.3, results are presented from a series of preliminary investigations involving generic laminar separation bubbles. The understanding gained from these simulations helped us in interpreting the results obtained from our highly resolved direct numerical simulations presented in section 2.4.

#### **3.1 Numerical method and code development**

For the simulations presented in this chapter, we used a high-order accurate research code which has been developed by our CFD group at the University of Arizona over many years. This code is based on an incompressible Navier-Stokes solver developed for investigating transitional and turbulent boundary layer flows (Meitz & Fasel 2000) and has been successfully applied to a wide range problems including flows with both passive and active flow control. The extensive experience with this code gives us great confidence in its accuracy and reliability. While the code was originally written for Cartesian grids, it has since been adapted to orthogonal curvilinear grids. The current version of the code employs fourth-order accurate compact finite differences in combination with a fourth-order accurate explicit Runge-Kutta time integration for the solution of the three-dimensional Navier-Stokes equations in vorticity-velocity formulation. The spanwise direction is treated with a pseudo-spectral approach, which results in very high accuracy. The large linear systems that result from the high-order compact discretization of the equations are solved iteratively using a zebra-alternating-line Gauss-Seidel (ZALGS) algorithm with multigrid acceleration. Given that supercomputers such as the new



Cray X1 can only be utilized to their full potential if a code is fully vectorized, the ZALGS, despite its slightly inferior smoothing properties (when compared with some other iteration schemes), was chosen because it lends itself to highly efficient vectorization. We have spent a significant amount of time optimizing the code for the new Cray X1. The parallelization in the code is performed by using the message passing interface (MPI) and the domain is “decomposed” with respect to the spanwise Fourier modes. The efficiency of this algorithm on the Cray X1 is very high. Results of typical parallel performance for our simulations are shown in Fig. 3.1. These three-dimensional benchmark calculations were performed on the 128 CPU Cray X1 at the AHPCRC. The problem size was increased along with the number of CPUs and ranged from  $\sim 2.1$  million points ( $513 \times 513 \times 8$ ) on 1 CPU to  $\sim 135$  million points ( $513 \times 513 \times 512$ ) on 64 CPUs. The speed-up is shown on the left, the parallel efficiency,  $\eta = (\text{ideal CPU time})/(\text{actual CPU time})$  is shown on the right. As can be seen in Fig. 3.1, the code scales well, especially when considering the amount of data communication that is required for such big simulations. For 64 CPUs, the speed-up is 43, which corresponds to a parallel efficiency of approximately 67%.

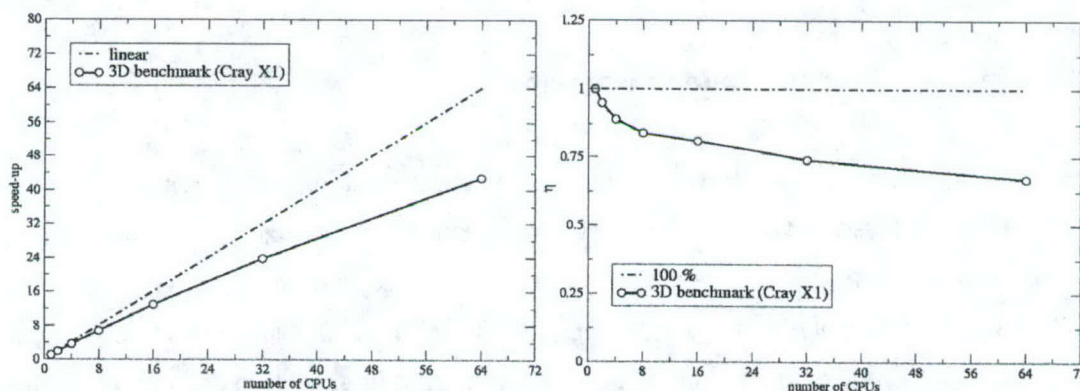


**Fig. 3.1: Parallel scaling of typical 3D simulations with the number of grid points ranging from  $2.1 \cdot 10^6$  to  $135 \cdot 10^6$ . The simulations were performed on the Cray X1 at the AHPCRC. Shown are the speed-up (left) and the parallel efficiency (right).**

### 3.2 Hydrodynamic instabilities in laminar separation bubbles

In the present section, results are presented for a prototypical laminar separation bubble on a flat plate. We performed these simulations in an effort to shed light on the complicated interaction of separation and transition in boundary layers. The importance of hydrodynamic instability mechanisms in understanding separation and reattachment in laminar separation



bubbles was already recognized by Gaster in his Ph.D. thesis 50 years ago (see Gaster, 1963). A profound understanding of the key physical mechanisms associated with the interaction of separation and transition is particularly relevant when passive and active flow control techniques are being considered, as is the case in the current research effort. The insight that we obtained from these preliminary investigations provided a good foundation on which to build our understanding of the relevant mechanisms that are present in active control of laminar boundary layer separation (see sections 3.3 and 3.4).

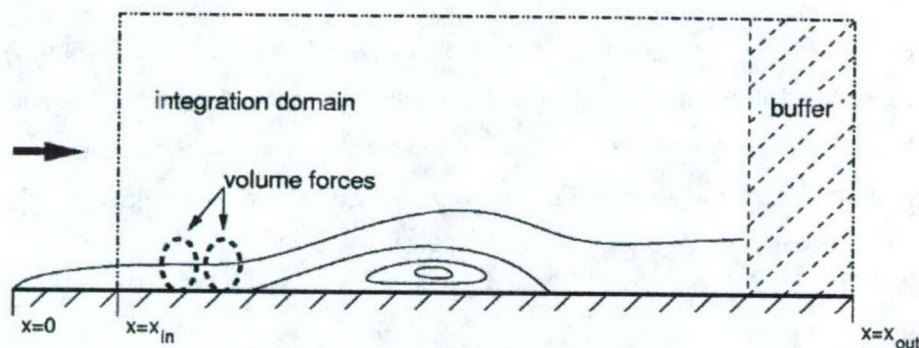


*Fig. 3.2: Schematic of the computational setup.*

In the simulations discussed below, the separation bubbles were generated by a volume force field such that the boundary layer was first accelerated and then decelerated in such a way that generic separation bubbles developed (see Fig. 3.2). In principle, the separation bubble could also have been generated by imposing a pressure gradient at the free stream boundary. However, using volume force fields facilitated the tailoring of the separation bubbles such that certain properties could be exposed. Depending on the strength of the volume force field, i.e. the magnitude of the acceleration or deceleration of the boundary layer, the simulations yielded separation bubbles that were either steady or unsteady.

### 3.2.1 Case 1: Steady separation bubble

For this simulation, the force field was gradually imposed on an attached, zero pressure gradient boundary layer (see Fig. 3.2). The final, maximum acceleration/deceleration was chosen such that the flow reached a steady state behavior (as shown in Fig. 3.3), albeit by a small margin. A slight increase in the maximum acceleration/deceleration would no longer have yielded a steady-state flow.



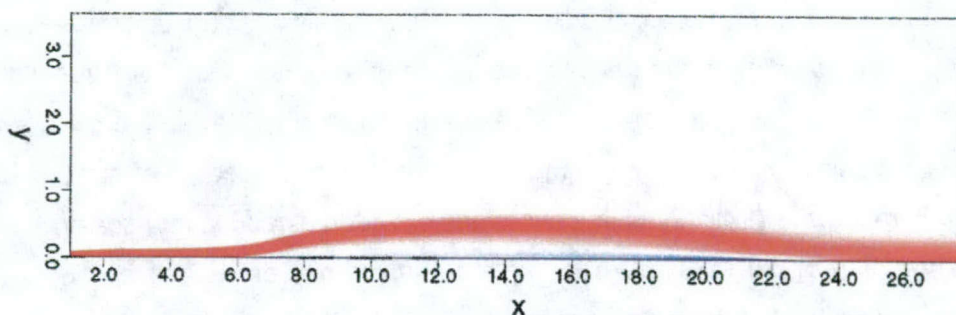


Fig. 3.3: Case 1: Spanwise vorticity contours (steady state).

The temporal development of the separated region can be observed clearly from the instantaneous wall shear, as shown in Fig. 3.4. It is obvious that the separated region increases with time until a final, steady state is reached. The velocity profile at the location of maximum negative wall shear stress is given in Fig. 3.5, indicating that a reverse flow of approximately 13% of the free stream velocity is reached.

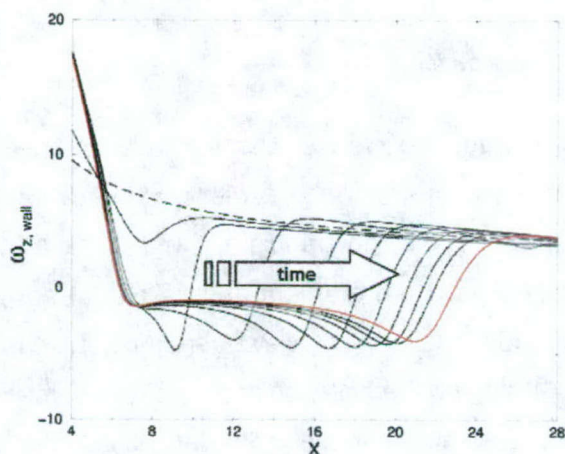


Fig. 3.4: Case 1: Temporal development of the spanwise wall-vorticity.

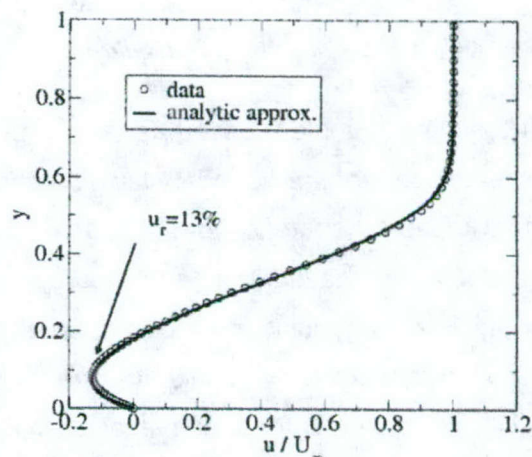


Fig. 3.5: Case 1: Velocity profile at the location of max. negative wall-shear.

This is mentioned here since in several other research efforts, it was observed that the intensity of the reverse flow is one of the parameters that determines whether the flow is convectively or absolutely (globally) unstable. In our investigation, we tried to determine if the flow is convectively or absolutely unstable by using a numerical simulation tool similar to the one proposed by Brancher and Chomaz (1997). For this, we set up a separate simulation with a parallel base flow and periodic inflow/outflow boundary conditions. The base flow was constructed by using the velocity profile (from the spatial simulation) that was to be examined



with respect to its convective or absolute instability (Fig. 3.6).

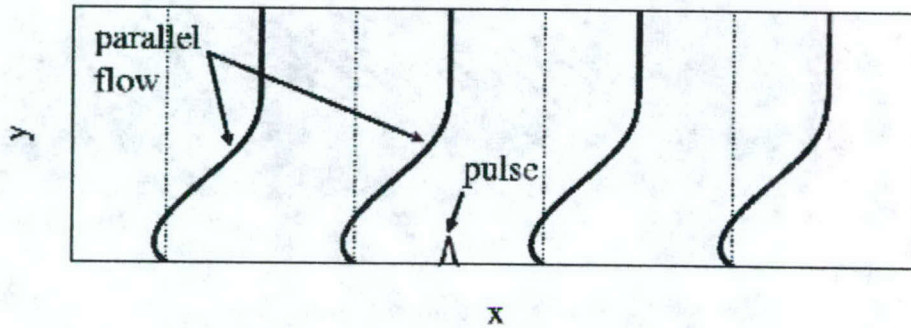


Fig. 3.6: Computational setup for the convective/absolute instability investigations.

Then, at a sufficient distance from the inflow and outflow boundaries, a very small pulse disturbance was introduced through a blowing and suction slot. The pulse generates a wave packet that grows in time and in space (if the profile is unstable), as shown schematically in Fig. 3.7. If the trailing edge of the wave packet propagates downstream (see left-hand-side of Fig. 3.7), the profile is classified as convectively unstable. If the trailing edge propagates upstream (see right-hand-side of Fig. 3.7), the profile is absolutely unstable. The calculation becomes meaningless once the perturbations reach the inflow and/or the outflow boundaries. Therefore, it is essential that the computational domain is sufficiently large so that a clear trend is established before the perturbations reach these boundaries.

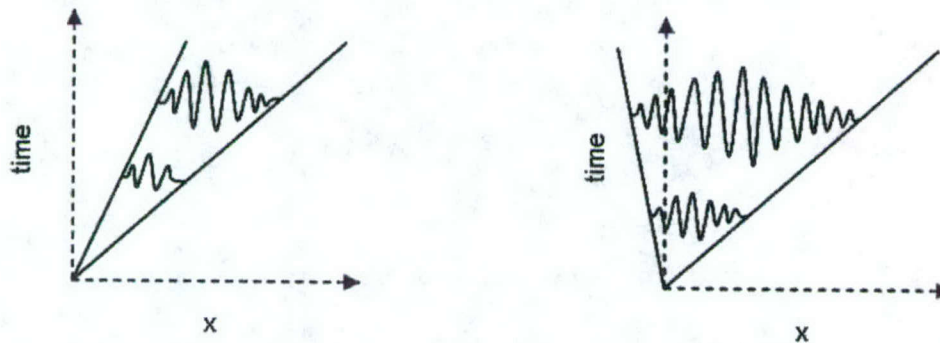
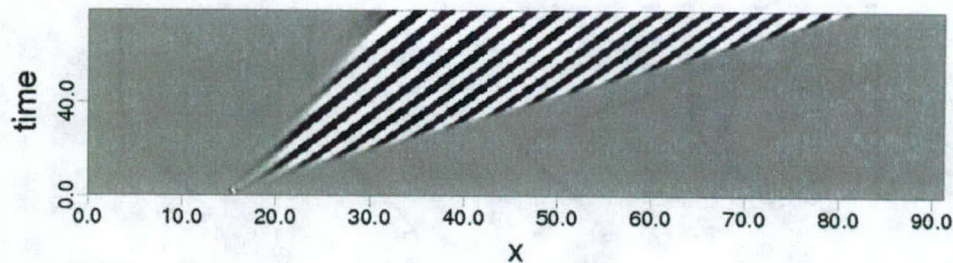


Fig. 3.7: Schematic of convective and absolute instability. Left: convective instability; right: absolute instability (Huerre and Monkewitz, 1990).

Applying this tool for the velocity profile of Fig. 3.5 yielded the response given in Fig. 3.8. To construct the  $t/x$  diagram of Fig. 3.8, the spanwise vorticity perturbations at the wall were used. It is obvious that these perturbations grow, but remain contained in a wedge. The trailing edge



of the wave packet propagates downstream, thus confirming that this profile is convectively unstable, but absolutely stable. This is consistent with the fact that our spatial simulation of this



*Fig. 3.8: Case 1:  $t/x$  diagram of the disturbance wall-vorticity.*

bubble lead to a steady behavior without unsteady perturbations.

The fact that this profile is convectively unstable can be clearly observed from Fig. 3.9, where the Fourier amplitude of the spanwise disturbance vorticity at the wall is plotted versus the downstream direction. The increase in amplitude by approximately seven orders of magnitude is an indication of the very strong (convective) instability which is caused by the inviscid (inflection point) instability mechanism.

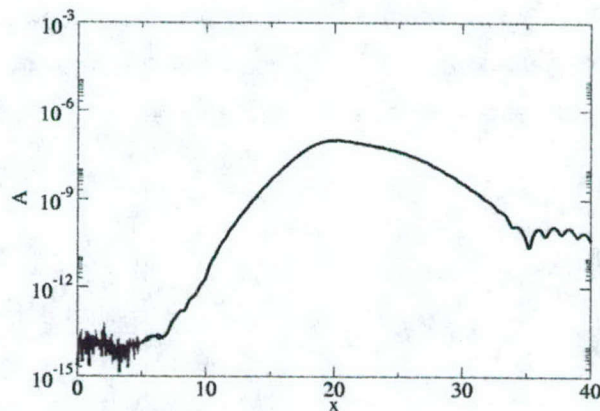


*Fig. 3.9: Case 1: Fourier amplitude of the disturbance wall-vorticity.*

However, as seen in Fig. 3.9, the amplitudes never reach levels large enough to observe a “visible” unsteadiness as “confirmed” by Fig. 3.3. Fig. 3.9 clearly points to the difficulty and dilemma when using numerical simulations and/or experiments for determining if a flow is convectively or absolutely (globally) unstable based on observations of “natural” (unforced) perturbation waves or vortex shedding. Due to the enormous amplification rates of the instability



waves (see Fig. 3.9), extremely small background disturbances (for example due to round-off error in simulations or free stream turbulence in experiments) can lead to visible, large disturbance waves and vortices without additional “controlled” forcing. To demonstrate this, we used the steady flow field of the previous simulation (see Fig. 3.3) as initial condition and introduced small, controlled perturbations (with an amplitude of 0.1% of the free stream velocity) by periodic blowing and suction through a slot located upstream of the separation location (see Fig. 3.10). The perturbations quickly grow to very large amplitudes, not surprising considering the very high growth rates observed in Fig. 3.9, so that large amplitude waves develop (typically described in the literature as “vortex shedding”). The large amplitude waves or “vortices” (“rollers”) enhance the exchange of momentum between the inner and outer fluid.

To answer the question of whether this phenomenon is only an artifact of the periodic forcing, we performed a simulation where random forcing was used instead of periodic forcing (everything else being the same). This is a better model of the effects of “uncontrollable” environmental disturbances that arise in experiments (free stream turbulence, vibrations, noise, etc.) or in numerical simulations (discretization and round-off errors). The response to the random forcing, as shown in Fig. 3.11, illustrates how disturbance amplification caused by the convective instability mechanism once again quickly leads to large perturbation waves (or vortices). However, since the flow is unstable with regard to a band of frequencies, a wide spectrum of frequencies (and wavelengths) can be observed. It is important to note that, in both simulations, the bubble returned to a steady state when the forcing was turned off.

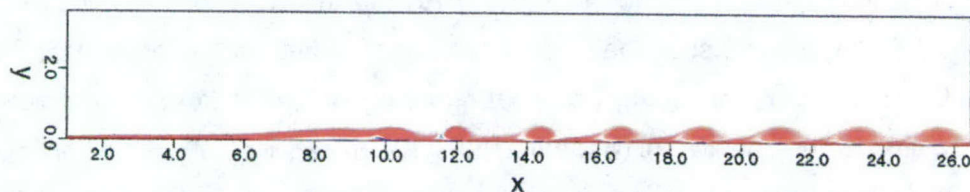


*Fig. 3.10: Case 1: Instantaneous vorticity contours for periodic forcing.*

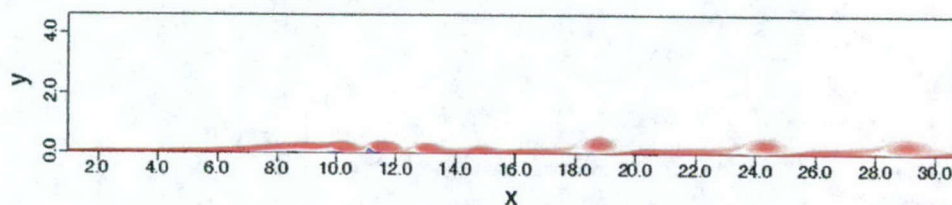


*Fig. 3.11: Case 1: Instantaneous vorticity contours for random forcing.*



### 3.2.2 Case 2: Marginally unsteady separation bubble

In the next sequence of simulations (case 2), the acceleration/deceleration in the force field was chosen such that large amplitude instability waves or “vortex shedding” occurred “naturally” (see Fig. 3.12), that is without adding “controlled” forcing, either periodic or random, as for the previous case 1.

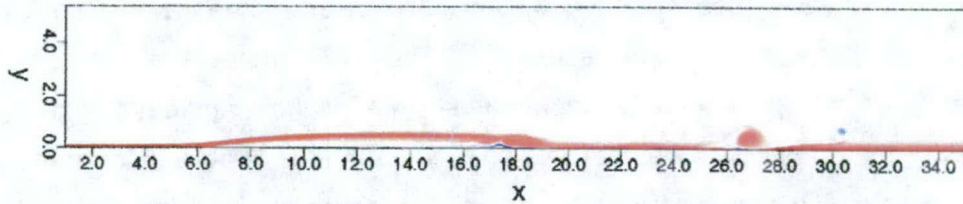


*Fig. 3.12: Case 2: Instantaneous spanwise vorticity contours.*

As before, the simulation was started with an attached boundary layer flow as initial condition, and then the volume force field was gradually imposed. It is noteworthy that the intensity of the force field was increased only by approximately 5% compared to case 1, indicating the strong sensitivity of the flow field to the increased acceleration/deceleration. The question arose whether the observed unsteadiness was caused by convective or absolute instability mechanisms. As observed from the previous case 1, the growth rates of the convective instability are very strong. Now, with the stronger acceleration/deceleration and, associated with this, the stronger separation, the amplification rates of the convective instability would also be accordingly larger. Therefore, the finite amplitudes that are reached (as a result of convective growth) may be such that “visible” vortex shedding can be observed. However, the unsteadiness or vortex shedding could, of course, also result from an absolute/global instability. To answer the question of whether an absolute instability is at play, we examined the profile with the maximum reverse velocity (approximately 25%), as shown in figure Fig. 3.13.



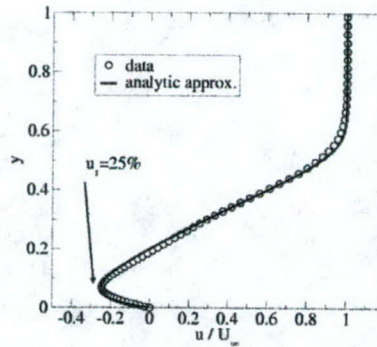


*Fig. 3.13: Case 2: Velocity profile for the stability investigation.*

This profile is only reached momentarily just before the shedding sets in. In order to establish a  $t/x$  diagram, we used the same numerical tool as discussed previously. The result of this analysis is presented in Fig. 3.14. As before, the wave packet-type disturbances grow in time and in space, and are contained in a wedge region. Contrary to the previous case, the left boundary of the wedge is now practically vertical, indicating that the trailing edge of the wave packet is stationary. Thus, disturbances never really convect entirely out of the field. Therefore, we classify this profile as “marginally” absolutely unstable. However, it is not possible to unequivocally attribute the observed vortex shedding to an absolute/global instability mechanism, because, as discussed previously, the strong convective instability is present at the same time.

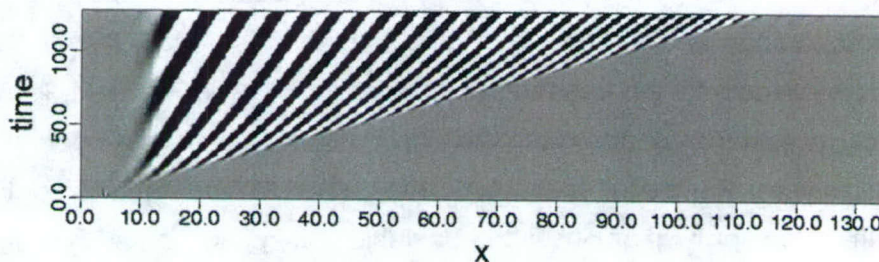


*Fig. 3.14: Case 2:  $t/x$  diagram of the disturbance wall-vorticity.*

What happens now if we additionally introduce external perturbations as for the previous case? The response to upstream periodic blowing and suction with the same small amplitude as in case1 is presented in Fig. 3.15. Comparing with Fig. 3.10 for the weaker separation (convective instability only), the responses are practically indistinguishable. This is an additional indication that judging convective versus absolute instability based on observed vortex shedding is misleading, at best. It should be noted that the bubble returned to the self-sustained



shedding when the additional external forcing was discontinued.

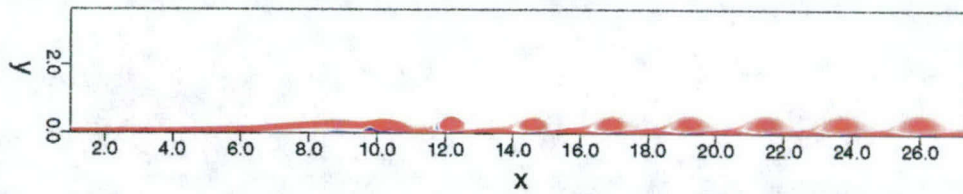


*Fig. 3.15: Case 2: Instantaneous vorticity contours for periodic forcing.*

### 3.2.3 Case 3: Highly unsteady separation bubble

In this case, the force field was such that it generated velocity profiles with considerably larger reverse velocities than in all the previous simulations. The instantaneous flow field shown in Fig. 3.16 illustrates the development of highly energetic structures.

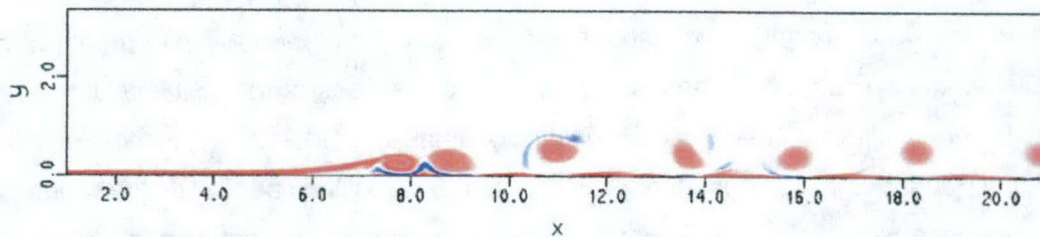


*Fig. 3.16: Case 3: Instantaneous spanwise vorticity contours.*

The entrainment and exchange of momentum caused by these structures is so strong that the extent of the separation is drastically reduced. Shortly before vortex shedding set in, the maximum reverse velocity for this case was approximately 55% (see Fig. 3.17). The  $t/x$  diagram of Fig. 3.18 now reveals a “true” absolute instability. In contrast to before, the perturbations now indeed travel upstream. For the full spatial simulation, at the location where this velocity profile arises, the disturbances grow in an absolutely unstable manner. In other words, a continuous “oscillator” is present that generates perturbations of increasing amplitude until a non-linear, finite equilibrium is attained. The streamwise extent of this absolutely unstable behavior is, of course, limited by the fact that sufficiently far away from the location where the maximum reverse flow is reached, the local profiles become absolutely stable. This is essentially the mechanism that leads to “global” modes (Couairon and Chomaz, 1996).



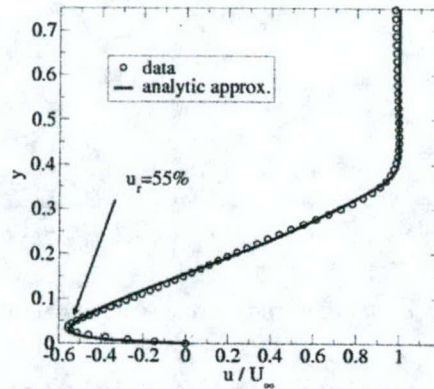


Fig. 3.17: Case 3: Velocity profile for the stability investigation.

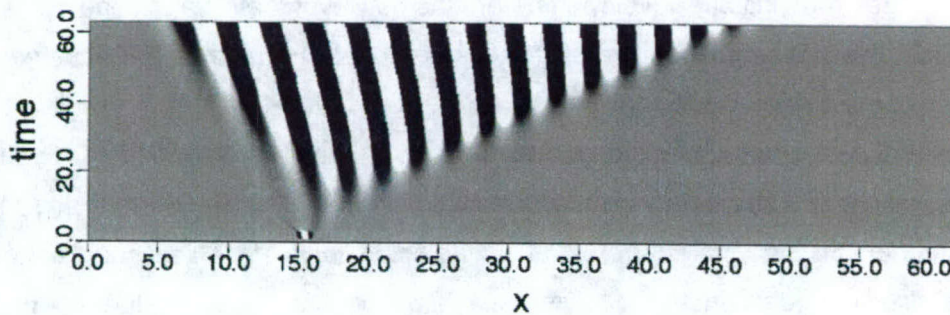


Fig. 3.18: Case 3:  $t/x$  diagram of the disturbance wall-vorticity.

All the simulations presented so far were two-dimensional, thus all three-dimensional effects were (deliberately) neglected. As a consequence, secondary (3-D) instability mechanisms were excluded and, in particular, the breakdown to turbulence could not occur. The only mechanisms allowed were viscous (Tollmien-Schlichting) and inviscid (Kelvin-Helmholtz) instability mechanisms. Thus, the question arose what contributions would arise from 3-D effects, and, in particular, from allowing the flow to transition? A simulation of the last case was performed for which the 2-D simulation was used as an initial condition for a 3-D simulation, thus allowing breakdown to turbulence. As can be observed from Fig. 3.19, compared to the 2-D simulation, the strong 2-D structures are considerably weakened, although shedding of 2-D coherent structures ("rollers") can still be observed. The weaker structures provide less exchange of momentum between outer and inner regions, and, as a consequence, the extent of the separation is greatly increased.



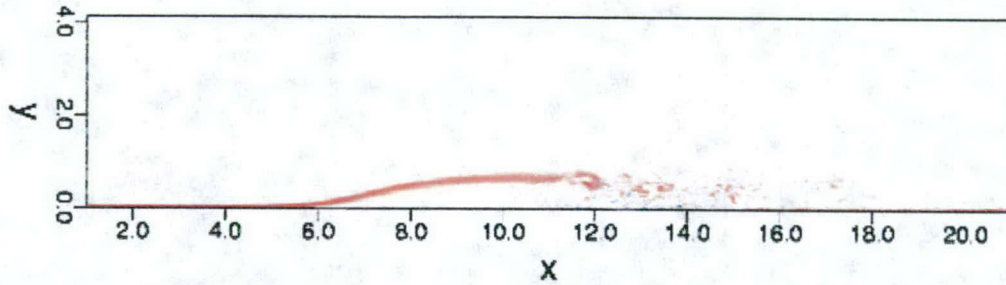


Fig. 3.19: Case 3: Instantaneous spanwise vorticity contours (3-D simulation).

Finally, for the same case (pressure gradient), the simulation was started up immediately in 3-D instead of first establishing a 2-D simulation as before. As in the 2-D simulation, large laminar (2-D) structures initially developed before the flow eventually transitioned (not shown). In other words, the 3-D simulation looked exactly like the 2-D simulation for quite some time. This observation provides additional evidence of the fact that the flow is initially absolutely unstable with respect to two-dimensional disturbances and that the growth of 3-D perturbations is the consequence of a secondary instability mechanism. The precise nature of this secondary instability mechanism is not fully understood, as the breakdown of the flow could either be due to a convective secondary instability (with very large growth rates) or due to an absolute secondary instability (as suggested by Maucher *et al.*, 1997 and Marxen *et al.*, 2004).

The examples discussed in this section demonstrate the intricate interplay of separation, hydrodynamic instability waves, and transition, where several complicated physical mechanisms are at play. The same (and possibly additional) mechanisms are likely to be relevant for the more complex situations found in low-pressure turbine flows, especially in the context of active separation control. Therefore, we are in the process of continuing similar model investigations as part of our current research efforts.



### 3.3 Active control of a generic separation bubble using Vortex Generator Jets (VGJs)

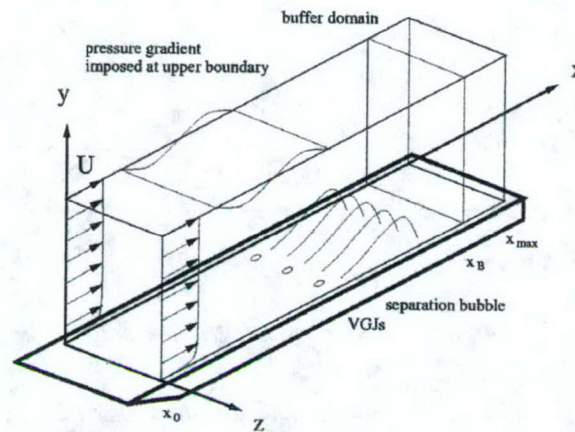
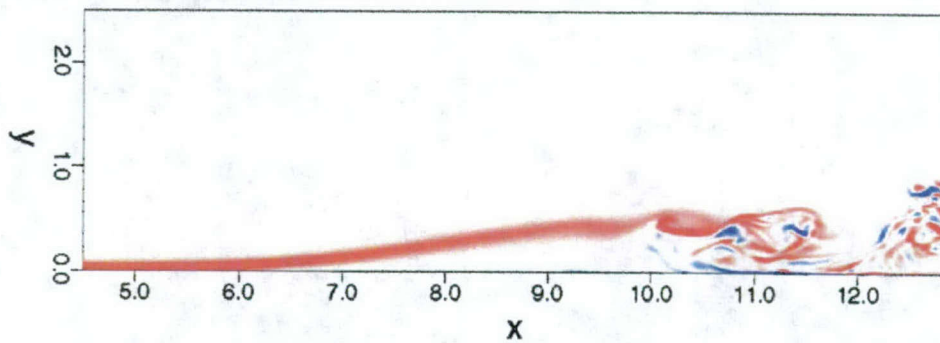


Fig. 3.20: Schematic of the computational setup.

The results presented in this section were obtained from simulations of a boundary layer on a flat plate. The investigations were aimed at providing insight into the fundamental mechanisms associated with active separation control at low Reynolds numbers using steady and pulsed VGJs. A laminar boundary layer was subjected to a strong adverse pressure gradient such that separation occurred. The flow transitioned to turbulence in the separated region and eventually reattached to the surface. The Reynolds number at the separation point was  $Re_{\delta,s}=375$  and was of the same order as in the experiments by Rivir and co-workers at AFRL (Bons *et al.* 1999, 2000, 2001, Sondergaard *et al.* 2002). At this Reynolds number, the boundary layer upstream of the separation point is sub-critical (recall that the Blasius boundary layer becomes unstable at  $Re_{\delta,s}=520$ ). This is important because the stability characteristics of the flow directly affect the effectiveness of any given control device. If the flow were super-critical, minute disturbances to the boundary layer, placed far enough upstream of the separation point, would likely suffice to initiate the transition process and to possibly prevent separation altogether. For a sub-critical flow, on the other hand, a significant disturbance input is required in order to achieve by-pass transition upstream of the separation region. If a successful control strategy is defined as one that is both effective *and* efficient (from an energy point of view), the by-pass transition scenario in an otherwise stable boundary layer does not seem to represent the most economical approach. Typical results from our simulations of the uncontrolled, separated boundary layer are shown in Fig. 3.21.





*Fig. 3.21: Instantaneous spanwise vorticity contours for the uncontrolled separation bubble.*

In the mean, the flow separates at about  $x=6.5$  and reattaches at about  $x=11.8$ . The length of the unforced separation bubble is approximately  $63 \delta^*$ . The setup of the VGJ actuation is shown schematically in Fig. 3.22. The pitch angle is the angle formed by the jet velocity vector and its projection onto the surface, the skew angle is the angle formed by projection of the jet velocity vector onto the surface and the x-axis (streamwise direction).

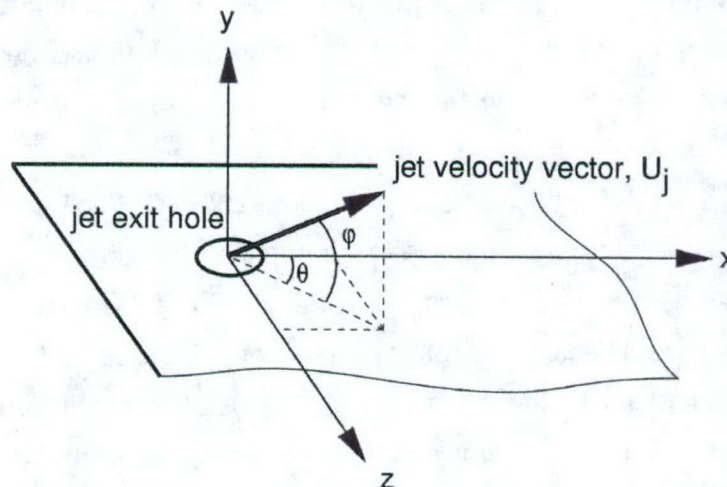


*Fig. 3.22: Schematic of VGJ forcing.  $\theta$ : skew angle.  $\phi$ : pitch angle.*

Two different VGJ configurations were investigated: (1) jets issued vertically into the boundary layer and (2) jets that are pitched and skewed to the free stream direction. For both configurations, steady and pulsed actuation was considered. The parameters used in the VGJ simulations are summarized in Table 2.1.



CASE	steady		pulsed	
	F1	F2	F3	F4
B.L. thickness / VGJ diameter	2			
VGJ spacing / VGJ diameter	8			
Pitch angle	90°	30°	90°	30°
Skew angle	—	90°	—	90°
Forcing frequency $F^+$	0	0	2	2
Duty cycle	—	—	10%	10%
Blowing Ratio	0.175			
Jet Momentum Coefficient $c_{\mu}$	$6.7 \cdot 10^{-5}$	$6.7 \cdot 10^{-5}$	$6.7 \cdot 10^{-6}$	$6.7 \cdot 10^{-6}$

Tab. 2.1: Forcing parameters for the VGJ simulations.

In cases F1 and F2, the jets were issued continuously. In cases F3 and F4, the jets were pulsed with a non-dimensional frequency  $F^+=2$  and a duty cycle of  $\tau=10\%$ . The pulsed jet actuation involves blowing only.  $F^+$  is based on the time-averaged length of the unforced separation bubble and the local free stream velocity at the jet injection location. With the blowing amplitudes being identical for both steady and pulsed blowing, the required mass flux for the pulsed blowing is one tenth of that required for the steady blowing. The values for the momentum coefficient,  $c_{\mu}$ , listed in Table 2.1 are based on a spatially averaged value of the jet-exit velocity. Typical results from simulations with pulsed, vertical VGJs and steady, vertical VGJs are shown in Fig. 3.23 and Fig. 3.24, respectively.

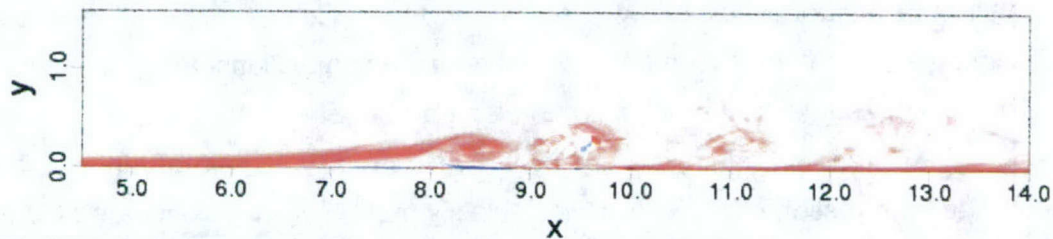


Fig. 3.23: Instantaneous vorticity contours for pulsed, vertical VGJs (in the plane of the jets)

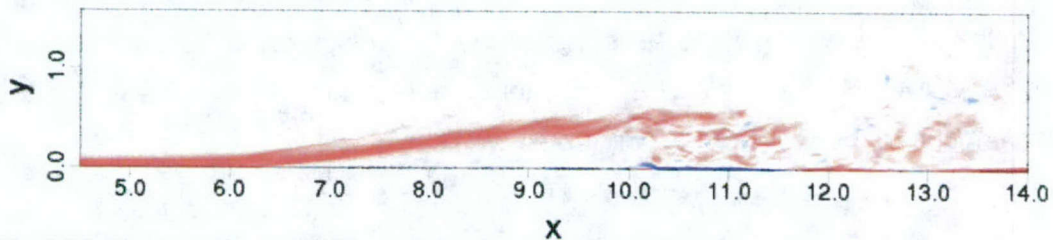
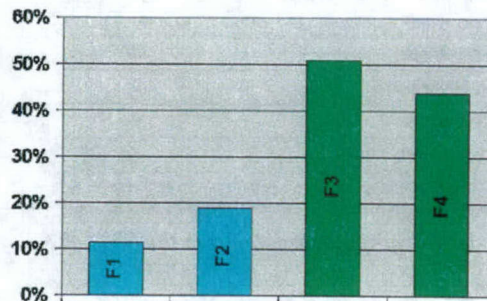


Fig. 3.24: Instantaneous vorticity contours for steady, vertical VGJs (in the plane of the jets).



The effect of the forcing on the separation behavior for all four cases is summarized in Fig. 3.25, where the time-averaged reduction of the separation (compared to the uncontrolled case) is plotted for cases F1 – F4.



*Fig. 3.25: Reduction of the extent of boundary layer separation.*

Fig. 3.25 clearly reveals that, for the generic separation bubble considered in this investigation, pulsed blowing was significantly more effective (and more efficient) than steady blowing. A comparison of cases F1 and F2 shows that for steady blowing, vertical jet injection is less effective than pitched and skewed injection. For pulsed blowing, on the other hand, the opposite seems to be the case. In regard to the amount of literature published on the effectiveness of pitched and skewed VGJs versus vertical VGJs, this observation initially seemed surprising. The following questions arose as a result of the conclusions drawn from Fig. 3.25: What is the role of the longitudinal structures for cases F1 and F2? What are the mechanisms that make pulsed blowing more effective than steady blowing? In the remainder of this section, we attempt to provide some answers to these questions. Fig. 3.26 shows time-averaged streamwise velocity profiles in the plane of the jet exit hole at  $x=7$ . This location corresponds to a position approximately eight diameters downstream of the VGJ injection location. The deformation of the streamwise velocity profiles visible for steady VGJ blowing (cases F1 and F2) clearly indicates the presence of longitudinal vortices. In cases F3 and F4, on the other hand, where the VGJs are pulsed with a duty cycle of  $\tau=10\%$ , no deformation is visible in the velocity profiles. This fact suggests that the dominant mechanism responsible for the high effectiveness of pulsed VGJs may not be related to the entrainment of free-stream momentum due to the presence of streamwise vortices.



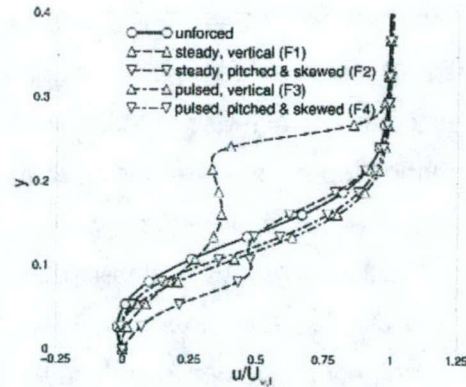
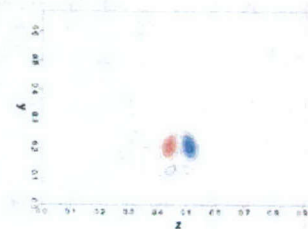
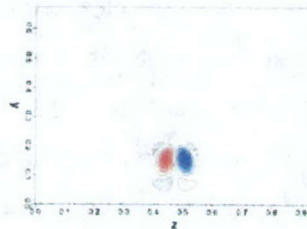
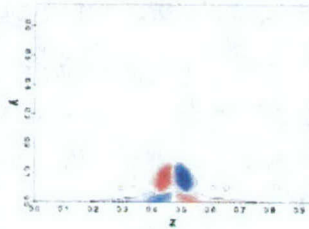


Fig. 3.26: Streamwise velocity profiles at  $x=7$ .

### 3.3.1 Steady VGJs

A comparison of the cases involving steady blowing (F1 and F2) is presented in Fig. 3.27. Shown are time-averaged contour plots of streamwise vorticity in the  $y$ - $z$  plane at three positions downstream of the forcing location.

#### • F1 (steady, vertical)



#### • F2 (steady, angled)

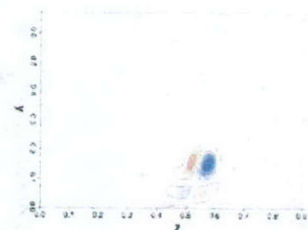
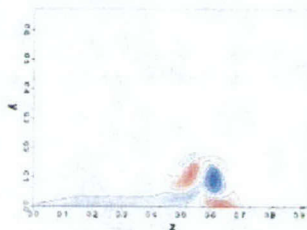
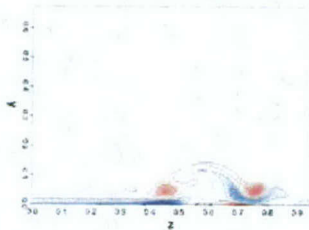


Fig. 3.27: Streamwise vorticity contours at selected downstream locations. Blue: clockwise rotation red: counter-clockwise rotation.

In case F1 (top), symmetric vortices are generated by the jets issuing vertically into the boundary layer. The symmetric nature of this vortex pair remains intact while its strength slowly decays as it develops downstream. The vortices move away from the wall, but are embedded in the separating boundary layer.



In case F2 (bottom), the generating process and the development of the longitudinal structures is far more complex. At  $x=6.45$ , three diameters downstream of the jet hole, two distinct vortical structures with counter-clockwise rotation seem to form, with most of the positive vorticity (clockwise rotation) confined to a region near the wall. The non-symmetric jet injection results in a significant interaction between the vortices, causing the formation of a clockwise-rotating structure that seems to gradually increase in strength as it develops in the streamwise direction ( $x=6.85$  and  $x=7.15$ ). A comparison of the structures shown in Fig. 3.27 reveals that the strength of the longitudinal vortices in both cases is approximately equal. This seems to contradict reports on the increased strength of streamwise vortices associated with pitched and skewed jet injection. In addition, the nature of the structures created by the angled jets in case F2 differs from those seen in experiments on VGJs in turbulent, zero pressure gradient boundary layers (see Khan and Johnston, 2000), where dominant vortical structures of one sign were observed downstream of the jets. Due to the fact that these dominant streamwise vortices were not observed in case F2, a simulation was performed where pitched and skewed jets (with the same parameters as in case F2) were injected into a laminar, *zero pressure gradient* boundary layer. Streamwise vorticity contours obtained from this simulation are shown in Fig. 3.28. The dominant, counter-clockwise-rotating structure that develops downstream of the jet is now clearly visible, and it is in excellent qualitative agreement with observations made by Khan and Johnston, 2000. In accordance with the results of Henry and Pearcey, 1994, Fig. 3.28 confirms that an adverse pressure gradient has a significant effect on the development of the longitudinal structures created by angled VGJs.

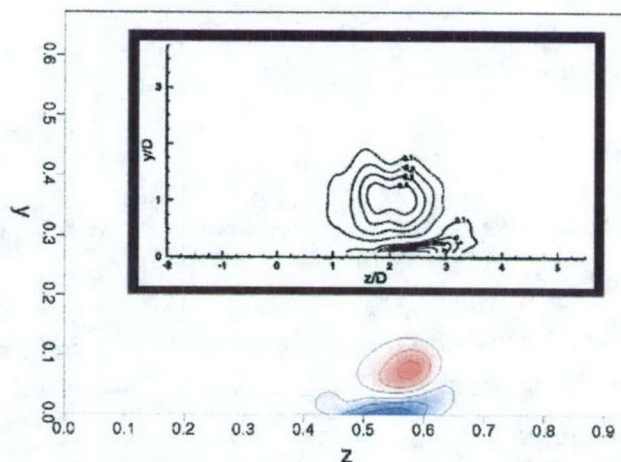


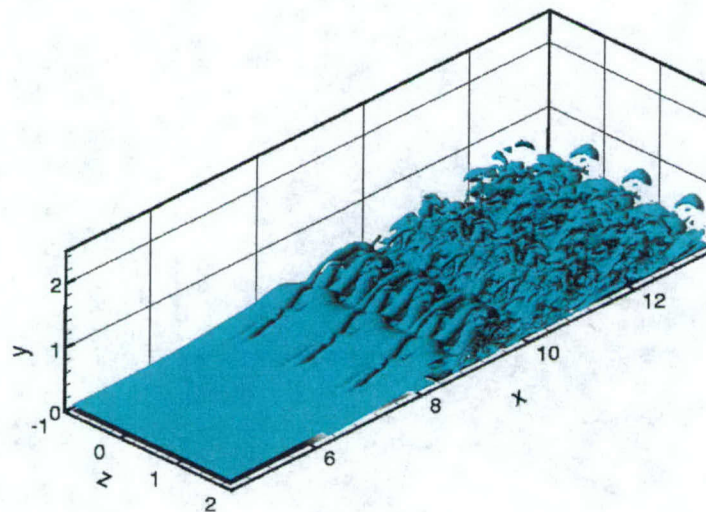
Fig. 3.28: Streamwise vorticity contours for steady, angled jets in a zero pressure gradient boundary layer.



The significant increase in performance of VGJ control associated with the introduction of pulsing is considered next.

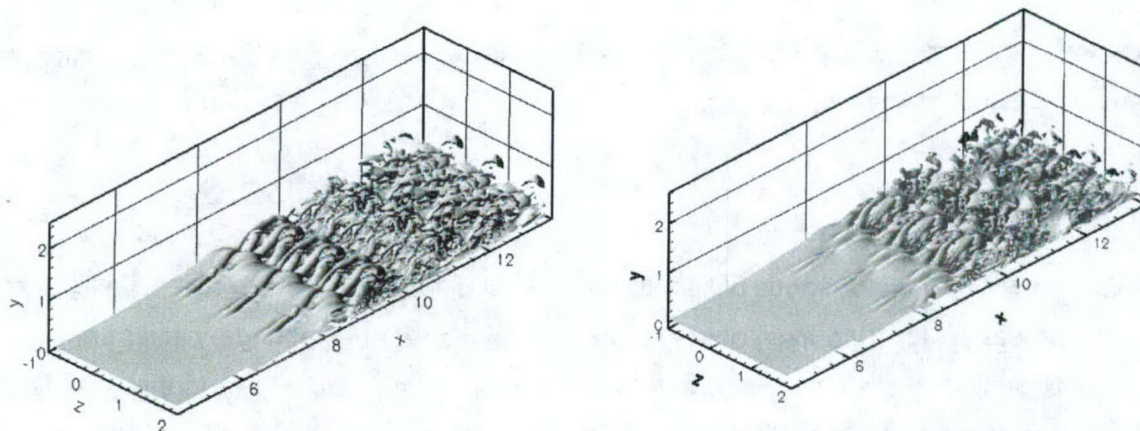
### 3.3.2 Pulsed VGJs

Fig. 3.29 shows instantaneous 3D contour surfaces of spanwise vorticity ( $\omega_z=3$ ) for case F3 (pulsed, vertical VGJs). Two main observations can be made: First, boundary layer transition occurs at a much earlier stage (compared to the steady VGJs), contributing to the increased effectiveness of pulsed blowing. Second, in addition to the apparent three-dimensionality of the structures visible in Fig. 3.29, distinct two-dimensional wave fronts (spanwise coherent structures) can be observed in the transitional region. The two-dimensionality of these structures is believed to be due to the strong inviscid instability of the inflectional free shear layer-type profile with respect to 2D disturbances. Despite the inherent three-dimensionality of VGJ control, a 2D unsteady disturbance component is always introduced as a result of the actuation. In other words, if the jets are pulsed with the proper frequencies (as is done here), it appears as though this natural instability mechanism can be exploited. A side-by-side comparison of the spanwise vorticity contours for pulsed, vertical VGJs and pulsed, angled VGJs (Fig. 3.30) reveals that similar observations can be made for case F4 as discussed above for case F3.



*Fig. 3.29: Instantaneous iso-surfaces of  $\omega_z$  for case F3 (pulsed, vertical VGJs).*





**Fig. 3.30: Instantaneous iso-surfaces of  $\omega_x$ . Comparison of case F3 (left) and case F4 (right).**

In an effort to further investigate the nature of the structures that are present in the case of pulsed VGJ control, the flow fields associated with cases F3 and F4 were analyzed using Proper Orthogonal Decomposition (POD). In Fig. 3.31, the first mode obtained from the POD of case F3 is shown. This mode contains the most energetic unsteady structures (mode 0 generally represents the mean flow). Shown are wall-normal velocity contours ( $|v|=0.01$ ) and the time signal associated with this mode. The coherent structures present in the flow field can now clearly be identified as predominantly two-dimensional. The time signal associated with mode 1 is also shown in Fig. 3.31. Comparison of this time signal with that of the VGJ input (shown in red) reveals that the structures are synchronized with the forcing and develop as a

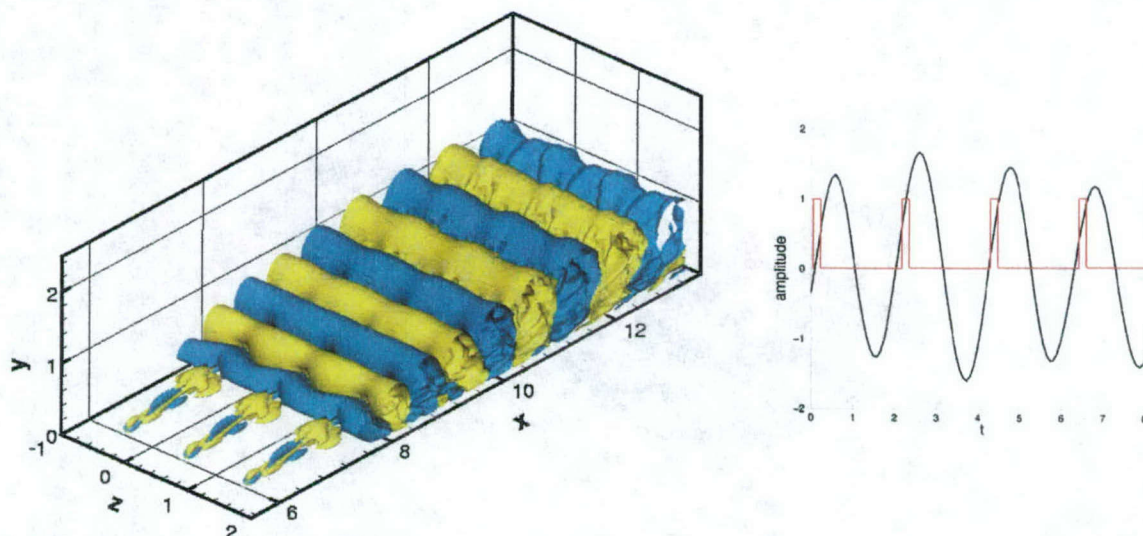


**Fig.2.31: Iso-surfaces of wall-normal velocity obtained from a Proper Orthogonal Decomposition (POD) of case F3. Insert: Associated POD- and forcing time signals.**



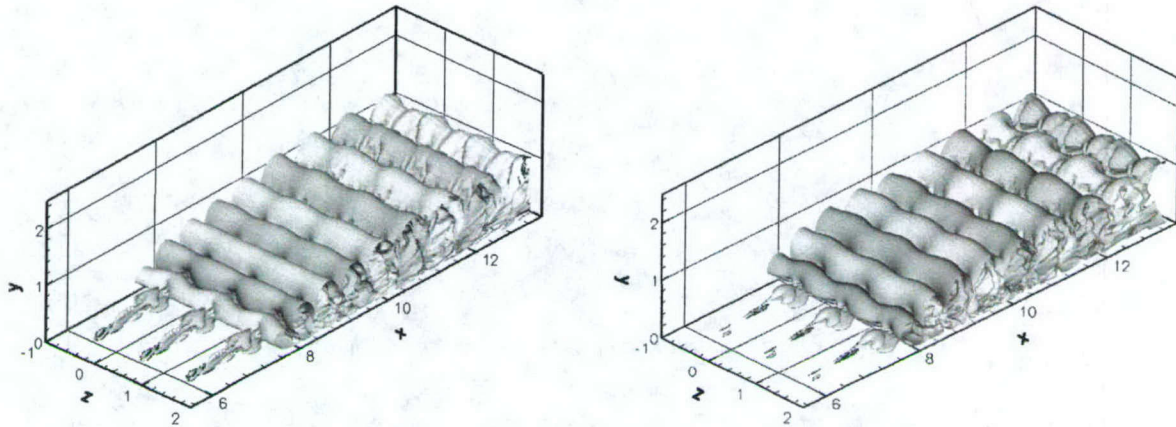


*Fig. 3.32: Iso-surfaces of wall-normal velocity from the POD. Comparison of case F3 (left) and case F4 (right).*

direct consequence of the actuation. The side-by-side comparison of the POD results for cases F3 and F4 (see Fig. 3.32) reveals that similar, (predominantly) two-dimensional coherent structures are also present in the case with pulsed, angled VGJ injection.

The wall-normal velocity contours confirm that the separated shear layer profile is most unstable with respect to 2D disturbances that develop into large-scale, spanwise coherent structures. The amplification of the 2D component of the instability modes in case F3 and case F4 is illustrated in Fig. 3.33. Shown is the development of the Fourier amplitudes for the spanwise disturbance wall vorticity. In spite of the relatively large amplitudes at the forcing holes, the disturbances grow exponentially (linear in the log-plot) downstream of an adjustment region. This exponential growth is another (strong) indication that linear instability mechanisms are present. Note that, in the case of steady blowing, the natural instability of the flow with respect to 2D disturbances is not exploited by the control device



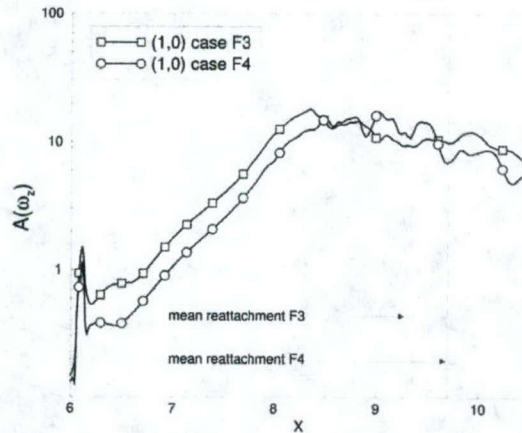


Fig. 3.33: *Fourier amplitude of the disturbance wall-vorticity.*

The results obtained from the present investigation of generic separation bubbles indicate that the spanwise structures likely play a key role in the increased effectiveness of pulsed versus steady jet actuation. It appears as though these 2D structures act in two ways. For one, the presence of a large-amplitude 2D disturbance accelerates the three-dimensional breakdown process. In addition, the 2D structures appear to enhance the momentum transfer between the free stream and the boundary layer.

Although we were able to gain valuable insight into the physical mechanisms associated with active flow control of generic laminar separation bubbles, the question arose as to whether or not these findings would still be relevant in a scenario that more closely matches the experiments conducted by Rivir and co-workers at AFRL.

### 3.4 Direct Numerical Simulations (DNS) of Active Flow Control (AFC) for a boundary layer subjected to Low-Pressure Turbine (LPT) blade conditions

The computational setup for the present flat-plate simulations is schematically depicted in Fig. 3.34. The goal of these investigations was to simulate the flow on the suction side of a LPT blade as in the experiments by Rivir and co-workers at AFRL. The effects of curvature were deliberately not taken into account, and they will be investigated after the flat-plate case is reasonably well understood.



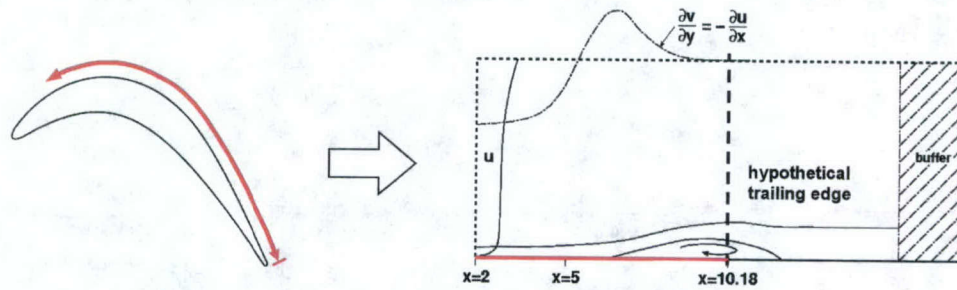


**Fig. 3.34: Computational setup.** The suction surface of the LPT blade is “unrolled” on a flat plate.

The flow was subjected to the same streamwise pressure gradient as measured in the experiments at a Reynolds number of 25,000 (based on chord length,  $C_x$ ). The wall-pressure coefficient versus suction surface length (SSL) for the uncontrolled case is shown in Fig. 3.35 in comparison to the experiments. The pressure plateau downstream of 62% SSL can be associated with the “dead-air” region in the separation bubble. Velocity profiles at various streamwise locations are also shown in Fig. 3.35.

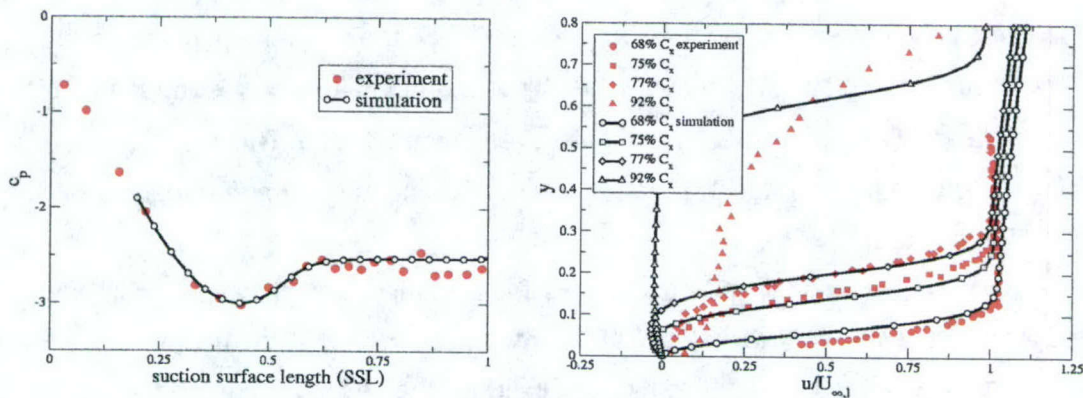


**Fig. 3.35: Wall pressure coefficient (left) and streamwise velocity profiles (right).** Comparison between simulations and experiments by Rivir and co-workers.

The reason that the experimental profiles do not show negative velocities is an artifact of the hot-wire measurements. While the experimental profile at 92%  $C_x$  may indicate attached flow, the boundary layer is in fact separated. Overall, the careful setup of the numerical simulations resulted in good agreement with the experimental data for the base flow. Typical results from a simulation of the uncontrolled, separated boundary layer are shown in Fig. 3.36. In the mean, the boundary layer separates at approximately  $x=5.7$  and reattaches at approximately  $x=15.8$ . Note that the trailing edge of the hypothetical LPT suction surface is located at  $x=10.18$ ,



indicating that the flow for an actual LPT cascade would, for this case, not reattach to the blade

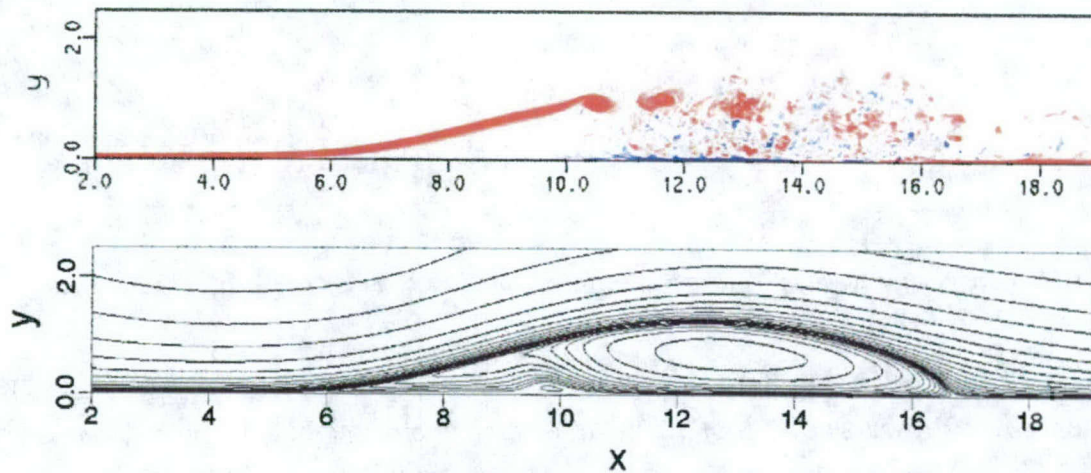


*Fig. 3.36: Top: Instantaneous contours of spanwise vorticity for the uncontrolled boundary layer; bottom: Time- and spanwise-averaged streamlines.*

surface.

For the simulations of active flow control, both steady and pulsed VGJs were employed for various forcing parameters. For the results presented here, the momentum coefficient,  $c_{\mu}$ , was  $7.9 \cdot 10^{-7}$  for both the steady and the pulsed VGJ investigations (this corresponds to a blowing ratio of  $B=0.32$  and  $B=1$  for the steady and pulsed jets, respectively). The duty cycle,  $\tau$ , (ratio of jet on-time to forcing period) was 10% for the pulsed cases, and the non-dimensional forcing frequency  $F^+$  was 4.2.

Time- and spanwise-averaged streamlines for the uncontrolled case in comparison to selected forced cases are shown in Fig. 3.37. For the cases with VGJ control, the extent of the separation region is reduced significantly, especially for the cases with pulsed VGJs. In other words, the same trend observed in the investigations involving generic laminar separation bubbles is also visible in the present cases: pulsed VGJs are considerably more effective in reducing boundary layer separation than steady VGJs (for fixed  $c_{\mu}$ ). In addition, analogous to the findings reported in section 3.3, pulsed, vertical VGJs appear to be slightly more effective than pulsed, angled VGJs. This conjecture is based on the fact that the streamlines indicate a smaller separation bubble for the case where the jets are issued vertically (see Fig. 3.37). Spanwise vorticity contours are presented in a top view towards the surface in Fig. 3.38. In addition to the cases shown in Fig. 3.37, a two-dimensional simulation was included for reference. In this simulation, disturbances were introduced by means of periodic blowing and suction through a slot (with the same frequency and momentum coefficient as used for the



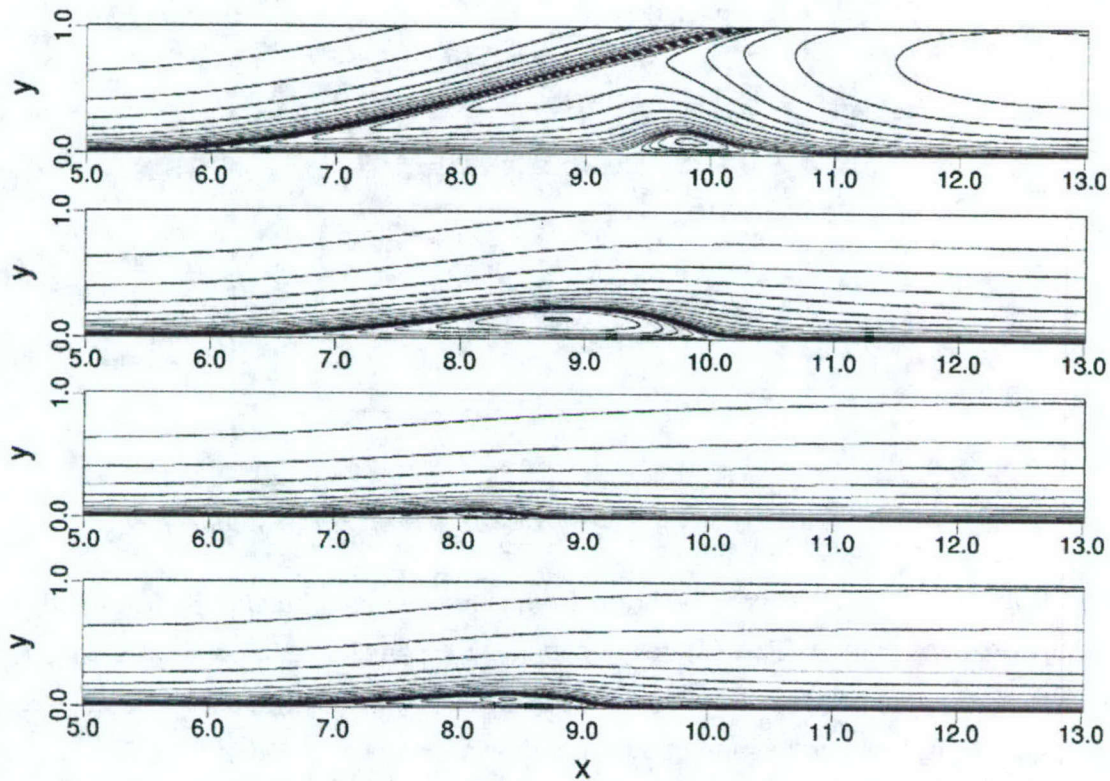


Fig. 3.37: Time- and spanwise-averaged streamlines for selected forced cases. From to bottom: Unforced case; steady, angled VGJs; pulsed, vertical VGJs; pulsed, angled VGJs.

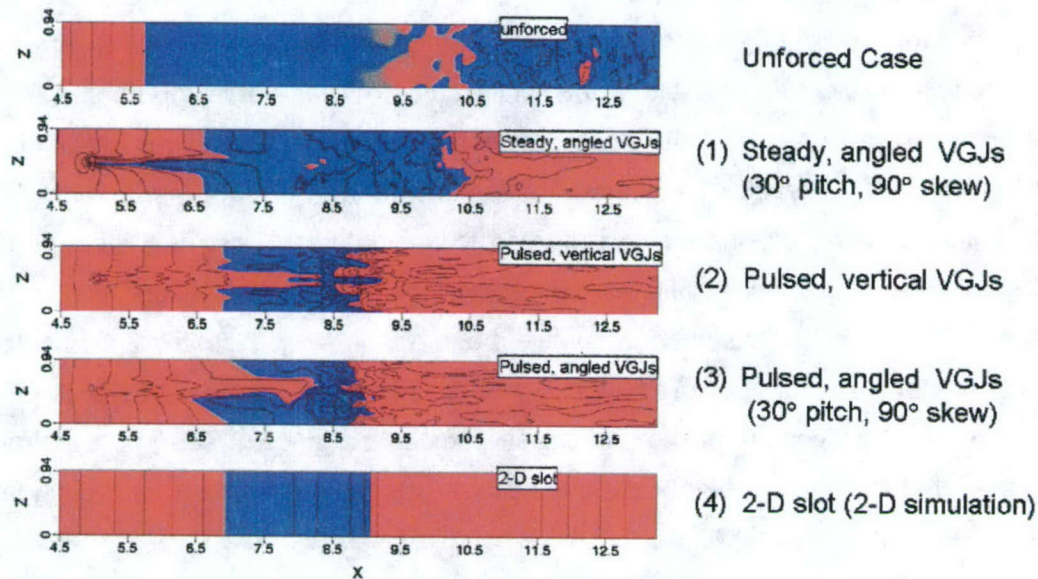
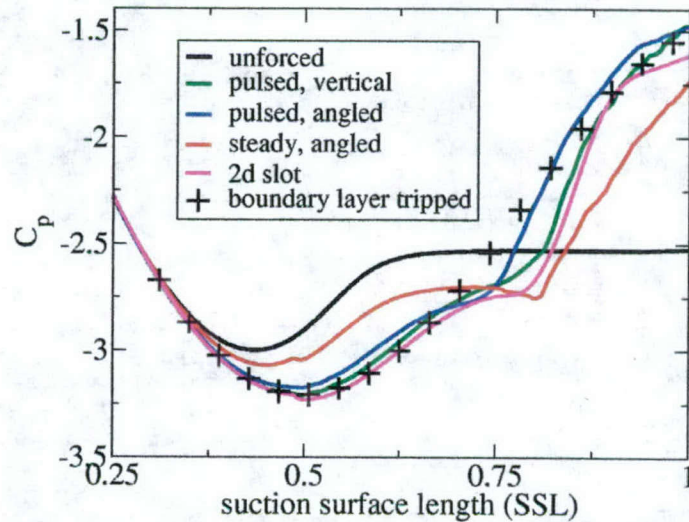


Fig. 3.38: Time-averaged contours of the spanwise vorticity component for selected forced cases. Top view towards the surface. Red areas represent attached flow, blue areas represent separated flow.





*Fig. 3.39: Wall pressure coefficients for the forced cases compared to the unforced case.*

pulsed VGJs). In the 2D simulation, the breakdown of the flow to turbulence is prevented, thus excluding one of the potential flow control mechanisms. As can be seen from Fig. 3.38, the 2D simulation is (at least) as effective in reducing boundary layer separation as the cases with pulsed VGJs. This corroborates the conclusion drawn in section 2.3 that the 2D structures, “laminar” or “coherent”, play an important role in the context of active flow control.

Fig. 3.39 shows the wall-pressure coefficients obtained from these simulations with active flow control in comparison to the unforced case. Also included is the curve obtained from a simulation where the boundary layer was tripped to turbulence upstream of the separation location, resulting in attached flow along the entire surface. This curve represents a good reference case for the present AFC investigations where a fixed pressure gradient was imposed on the flow. For each of the forced cases shown in Fig. 3.39, the location of the pressure minimum moved downstream compared to the unforced case, especially for the pulsed VGJ cases and for the case with two-dimensional forcing. Steady, angled VGJ actuation was the least effective of the cases shown, while the curve obtained from the 2-D simulation was practically identical to that of the fully attached flow between 30% and 65% SSL. The differences in the effectiveness of the various strategies (for fixed  $C_\mu$ ) seem to be strongly related to the fundamentally different physical mechanisms that are at work for forcing using steady versus pulsed VGJs.



### 3.4.1 Steady VGJs

Since, in all our previous simulations with steady VGJs, we did not find the strong streamwise vortices that have been reported in the literature, we performed a series of additional simulations in an effort to gain insight into the nature of the structures that develop downstream of the forcing location. Fig. 3.40 shows contour plots of the streamwise vorticity component as well as velocity profiles at  $x=7$  for increasing values of the jet blowing ratio  $B$  (ratio of maximum jet velocity to free stream velocity). In the vorticity plots, blue areas represent clockwise rotation, red areas represent counter-clockwise rotation.

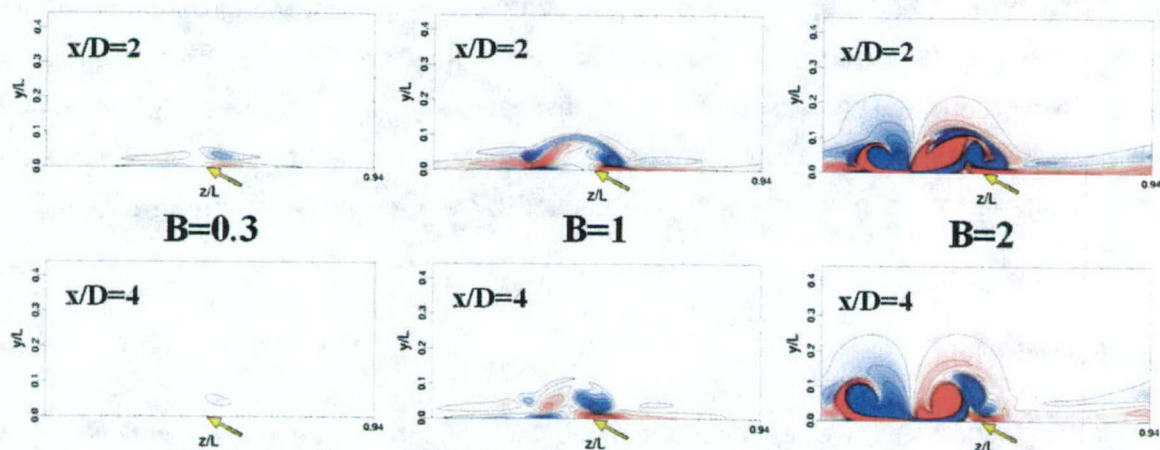


Fig. 3.40: Streamwise vorticity contours at selected downstream locations for various jet blowing ratios.

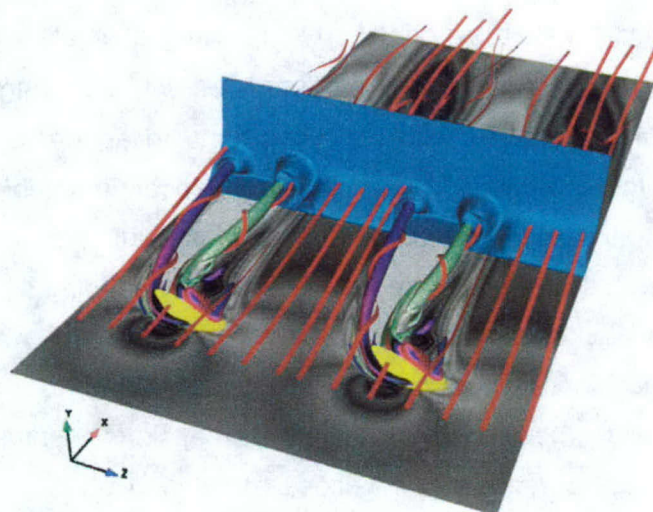


Fig. 3.41: Flow visualization for steady, angled VGJs ( $B=2$ ). Yellow: VGJs; red: streamlines; blue: streamwise velocity profiles; purple and green:  $\lambda_2$  iso-surfaces.



The contour levels are identical for all three cases. As the jet velocity was increased, dominant streamwise structures developed, as was observed in numerous experimental studies of turbulent VGJ control (Johnston and Nishi 1990, Compton and Johnston 1992, Khan and Johnston 2000). These structures have great potential for enhancing the momentum exchange between the near-wall and outer regions of the flow. This is illustrated in Fig. 3.41 for the case with  $B=2$  in a perspective view of the flow field. Shown are the VGJs (yellow), streamlines (red), streamwise velocity profiles (blue), as well as iso-surfaces of the  $\lambda_2$  vortex identification criterion (Jeong and Hussain 1995) (purple and green). The longitudinal vortices become so strong that the streamlines actually “wrap around” the  $\lambda_2$  iso-surfaces. As a result, enough high-momentum fluid is transported to the near-wall region to generate a “new” boundary layer that is energetic enough to overcome the pressure gradient without separating. Therefore, we conjecture that for high enough jet velocities, the dominant physical mechanism for the effectiveness of steady, angled VGJs is the momentum exchange caused by the formation of strong streamwise vortices.

### 3.4.2 Pulsed VGJs

For the pulsed VGJs, the reattachment of the flow appeared to be at least partially due to the momentum exchange as a result of an accelerated boundary layer transition. The transition process can be clearly observed in Fig. 3.42 and Fig. 3.43. Here, the  $\lambda_2$  vortex identification criterion (Jeong and Hussain 1995) was used to highlight the nature of the structures created by the pulsed jets (for both vertical and angled injection).  $\Lambda$ -structures, along with the subsequent development of ring-like or hairpin vortices, were found to appear only a short distance downstream of the forcing location. These structures closely resemble the late stages of classical Klebanoff-type transition scenarios (Rist and Fasel 1995, Bake et al. 2002). Thus, it appears as though the pulsed VGJs are very effective in triggering a by-Pass mechanism leading to a relatively quick breakdown to turbulence. However, as was already shown in section 3.3, another mechanism appears to be present. In addition to accelerating transition, the pulsed jets, once again, seem to exploit the two-dimensional instability of the underlying base flow. When the pulsing frequency was chosen according to the natural instability of the separated shear layer, strong spanwise coherent structures could be observed both in the transitional region as well as in the turbulent region downstream of the reattachment location. Due to the natural instability of the separated shear layer with respect to two-dimensional



disturbances, these structures are amplified in the downstream direction, as was already shown in Fig. 3.33 for the generic separation bubble. The amplification of the two-dimensional instability modes for the present cases is illustrated in Fig. 3.44. Results are once again shown for both vertical and angled VGJs.

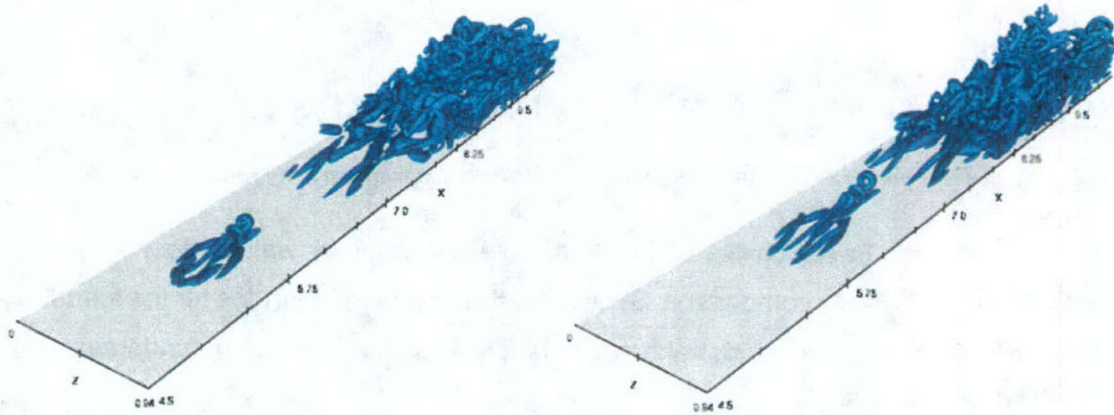


*Fig. 3.42: Vortex Visualization for pulsed, vertical VGJs. Shown are iso-surfaces of negative  $\lambda_2$ .*

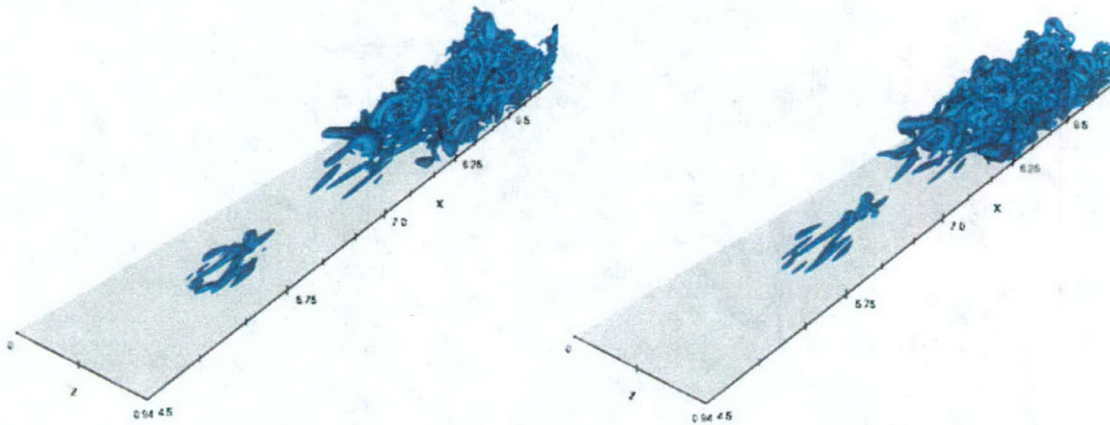


*Fig. 3.43: Vortex Visualization for pulsed, angled VGJs. Shown are iso-surfaces of negative  $\lambda_2$ .*



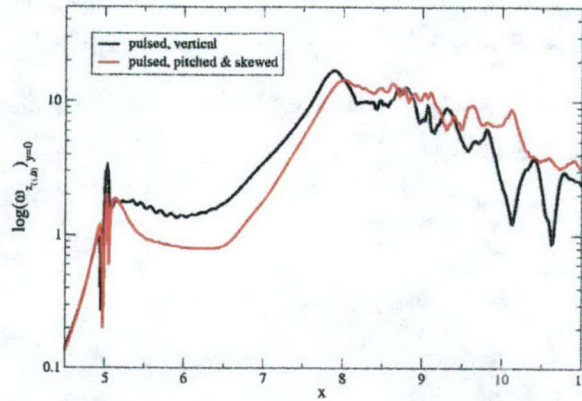


*Fig. 3.44: Fourier amplitude of the spanwise disturbance wall-vorticity for pulsed VGJs..*

In Fig. 3.45, the development of the spanwise disturbance wall-vorticity from the 2D simulation is presented for comparison. Shown are the Fourier amplitudes for the fundamental frequency as well as for several higher harmonics. The development of the fundamental in the 2D simulation exhibits similar growth as the curves in Fig. 3.44, which serves as additional “evidence” for the presence of 2D instability mechanisms in the cases with pulsed VGJ control.

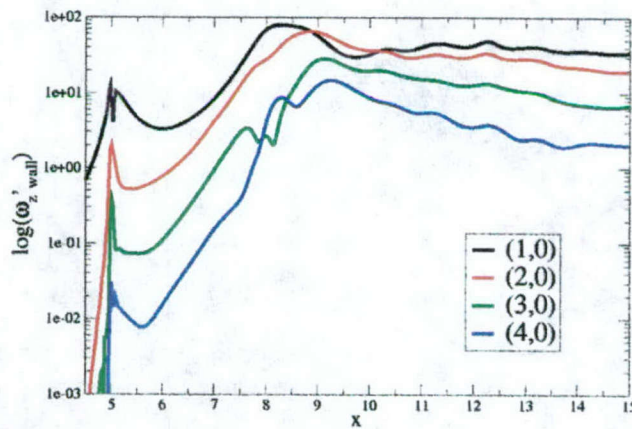


*Fig. 3.45: Fourier amplitude of the disturbance wall-vorticity (2D simulation).*



#### 4. SUMMARY AND CONCLUSION

In collaboration with the experimental effort at AFRL, we performed numerical investigations of AFC for LPT separation. We chose a two-pronged approach: A computationally less efficient but more versatile finite volume code was employed for simulations of the full geometry. Detailed investigations of the VGJ actuation for a flat plate model problem were performed with a very efficient finite difference code.

In the first approach (chapter 2), the transitional flow in a Low Pressure Turbine (LPT) cascade at a Reynolds number (based on inflow velocity and axial chord) of 25,000 was studied. The same cascade was investigated experimentally by Rivir and co-workers at the AFRL (Bons et al. 1999, 2000, 2001, Sondergaard et al. 2002). In initial two-dimensional (2-D) simulations with a higher-order accurate numerical scheme, the size of the separated flow region and the intensity of the reverse flow in the bubble were underpredicted. When the inflow Mach number was lowered, the agreement with the experimental results was considerably improved. Since 3-D motion and turbulence are suppressed in 2-D calculations and since the flow is transitional, we decided to investigate the capability of URANS and to perform 3-D DNS and ILES simulations. URANS calculations were performed with different turbulence models and inflow turbulence intensities. In general, turbulent viscosity and 3-D motion were found to weaken the spanwise coherent structures in the separated flow region, thus reducing wall normal mixing which resulted in a larger flow separation. A 2-D calculation with a 2<sup>nd</sup>-order accurate upwind scheme and without turbulence model showed a similar trend. Results were found to be strongly dependent on the inflow turbulence level and the turbulence modeling approach. For a certain combination of turbulence model and inflow turbulence quantities, very good agreement with the experimental data was achieved. The complexity of the flow (laminar separation and transition) makes for a very challenging test case for turbulence modeling. A 3-D simulation for the design blade spacing confirmed that the spanwise coherent structures that dominate the separated shear layer and the wake in the 2-D calculations were still present in the 3-D flow. The flow was shown to transition to turbulence upstream of the trailing edge. Similar results were obtained from a 3-D ILES simulation based on a diffusive 2<sup>nd</sup>-order accurate upwind scheme. In general, the extent of flow separation predicted in the simulations was slightly smaller than in the experiment.

It was shown in the experiments that separation control for LPT blades can noticeably increase performance at off-design conditions. Active Flow Control (AFC) by pulsed blowing



through a slot upstream of the separation location was explored in 2-D calculations. In the calculations presented here the blowing ratio and duty cycle were left constant. It was shown that forcing with a duty cycle of 10% excited higher harmonics at relatively large amplitudes. From an application point of view, it may be advantageous to force a large number of frequencies simultaneously since the optimum frequency may be unknown or varying, depending on the free stream conditions. It was shown that the efficiency of the forcing depended on the forcing frequency. When the forcing frequency was chosen such that the shear layer instability was exploited the disturbances became amplified and the control became more efficient. A 7.7% increase in lift over drag could be achieved. The optimum frequency of the controlled flow was shown to be slightly larger than the dominant frequency of the uncontrolled flow.

Pulsed Vortex Generator Jets (VGJs) were studied in 3-D ILES simulations. Although the flow dynamics near the jet exit holes were not accurately captured, the pulsed VGJs were shown to trigger early flow transition. A Proper Orthogonal Decomposition (POD) of the flow revealed that the time signal of the most energetic unsteady modes was directly linked to the forcing frequency of the jets, indicating that the forcing also left a "footprint" on the flow in the form of spanwise coherent structures. In a 3-D simulation at a 25% larger blade spacing, the flow transitioned well upstream of the trailing edge. The additional mixing associated with the turbulent small scale motion significantly weakened the spanwise coherent structures and delayed separation. In a preliminary 2-D simulation it was shown that periodically passing upstream wakes have a significant impact on the flow, generating spanwise flow structures and delaying flow separation.

AFC by pulsed blowing was also explored in 2-D calculations for a 25% larger blade spacing. Again, the efficiency of the pulsed blowing was shown to be dependent on the forcing frequency. When the forcing frequency was chosen "properly", a 19.4% gain in lift over drag could be accomplished. However, forcing at this optimal frequency also resulted in high dynamic loads. When the forcing frequency was chosen slightly different from the optimal frequency, comparable gains could be obtained without incurring high dynamic loads. However, 3-D simulations are required to obtain confidence in the effectiveness of AFC by pulsed blowing at larger blade spacings. However, since 3-D simulations of the entire cascade are very expensive, broad parameter studies would still have to be conducted with 2-D calculations. Although 2-D simulations do not quantitatively capture all relevant aspects of the flow control, they do seem to qualitatively predict the correct trends and dependencies.



In the second approach (chapter 3), the fundamental mechanisms associated with steady and pulsed VGJ control were investigated using Direct Numerical Simulations. Significant progress was made in our understanding of the complicated interaction of boundary layer transition and separation in the presence of localized flow control actuators such as VGJs. Strong streamwise vortices were found to develop for high-amplitude, steady jets when they were employed at an angle with respect to the free stream direction. Pulsed jets, on the other hand, were found to reduce/prevent separation by a combination of two mechanisms: (1) accelerated (by-pass) boundary layer transition and (2) development of strong, spanwise coherent structures as a consequence of the natural hydrodynamic instability of the underlying flow. At the present stage of our research effort, we conjecture that the higher efficiency of pulsed VGJs versus steady VGJs (for a fixed "energy input") is a direct consequence of exploiting this underlying instability mechanisms by pulsing with the proper frequencies. However, although we have made considerable progress, many questions remain. First of all, we need to unequivocally establish the differences in the relevant mechanisms for steady versus pulsed VGJ actuation for other flow conditions (Reynolds numbers and geometries) to explore the validity and "universality" of the preliminary explanations that we have come up with so far. For the pulsed jets, in particular, it is unclear whether boundary layer reattachment is achieved primarily due to transition to turbulence or due to the excitation of large, spanwise coherent structures. Second, the deliberate neglect of convex surface curvature in our simulations to date requires that we consider these effects in future investigations.



## 5. CONFERENCES, WORKSHOPS, AND PAPERS

Results from the current grant were reported in the following conferences, workshops, and papers:

Gross, A., Fasel, H.F., 2005, "Simulation of Active Flow Control for a Low Pressure Turbine Blade Cascade," AIAA-2005-0869

Fasel, H.F., Postl, D., 2004, "Interaction of Separation and Transition in Boundary Layers: Direct Numerical Simulations," In *Laminar-Turbulent Transition, Proceedings of the IUTAM Symposium, Bangalore, India*. Springer.

Fasel, H. F., Gross, A., Postl, D., 2004, "Numerical Simulation of Active Flow Control for Low Pressure Turbine Blades," RTO Applied Vehicle Technology Panel (AVT) Specialist Meeting on "Enhancement of NATO Military Flight Vehicle Performance by Management of Interacting Boundary Layer Transition and Separation," 4-7 October 2004, Prague, Czech Republic

Gross, A., Fasel, H.F., 2004, "Active Control of Separation for Low-Pressure Turbine Blades," AIAA-2004-2203

Postl, D., Gross, A., Fasel, H.F., 2004, "Numerical Investigation of Active Flow Control for Low-Pressure Turbine Blade Separation," AIAA-2004-0750

Postl, D., Gross, A., Fasel, H.F., 2003, "Numerical Investigation of Low-Pressure Turbine Blade Separation Control," AIAA-2003-0614 (submitted to AIAA J.)

Fasel, H.F., Gross, A., Postl, D., 2004, "Numerical Simulation of Active Flow Control for Low Pressure Turbine Blades," NATO RTO Specialist Meeting (RSM) on Enhancement of NATO Military Flight Vehicle Performance by Management of Interacting Boundary Layer Transition and Separation, Prague, Czech Republic

Fasel, H.F., Gross, A., Postl, D., 2003, Minnowbrook IV Workshop on Transition and Unsteady Aspects of Turbomachinery Flows

Fasel, H.F., Gross, A., Postl, D., 2003, "Control of Separation for Low Pressure Turbine Blades: Numerical Simulations," Workshop Crete, Greece



## REFERENCES

- Bake, S., Meyer, D.G.W., Rist, U., 2002, "Turbulence Mechanism in Klebanoff Transition: A Quantitative Comparison of Experiment and Direct Numerical Simulation," *J. Fluid Mech.* **459**: 217-243
- Bewley, B.R., Moin, P., Temam, R., 2001, "DNS-based predictive control of turbulence: an optimal benchmark for feedback algorithms," *J. Fluid Mech.* **447**: 179-225
- Bons, J.P., Sondergaard, R., Rivir, R.B., 1999, "Control of Low-Pressure Turbine Separation Using Vortex Generator Jets," AIAA-99-0367
- Bons, P.B., Sondergaard, R., Rivir, R.B., 2000, "Turbine Separation Control Using Pulsed Vortex Generator Jets," *Proceedings TURBOEXPO 2000*, Munich, Germany, May 8-11
- Bons, J.P., Sondergaard, R., Rivir, R.B., 2001, "Turbine Separation Control Using Pulsed Vortex Generator Jets," *Transactions of the ASME* **123**, Vol. 123
- Bons, J.P., Sondergaard, R., Rivir, R.B., 2001, "The Fluid Dynamics of LPT Blade Separation Control Using Pulsed Jets," *Proceedings of TURBOEXPO 2001*, New Orleans, LA
- Brancher, P., Chomaz, J.M., 1997, "Absolute and convective secondary instabilities in spatially periodic shear flows", *Physical Review Letters*, **78** (4): 658-661
- Chernobrovkin, A., Lakshminarayana, B., 1999, "Turbulence Modeling and Computation of Viscous Transitional Flows for Low Pressure Turbines," *Transactions of ASME* **121**: 824-833
- Chong, M.S., Perry, A.E., Cantwell, B.J., 1990, "A general classification of three-dimensional flow fields," *Phys. Fluids A* **2** (5), pp. 765-777
- Collis, S.S., Ghayour, K., Heinkenschloss, M., Ulbrich, M., Ulbrich, S., 2002, "Optimal control of unsteady compressible viscous flows," *Int. J. Numer. Meth. Fluids* **40**(11): 1-30
- Compton, D.A., Johnston, J.P., 1992, "Streamwise Vortex Production by Pitched and Skewed Jets in a Turbulent Boundary Layer," *AIAA J.*, **30**: 640-647
- Couairon, A., Chomaz, J.M., 1996, "Global instability in fully nonlinear systems," *Physical Review Letters*, **77** (19): 4015-4018
- Fujisawa, N., Nakabayashi, T., 2002, "Neural network control of vortex shedding from a circular cylinder using rotational feedback oscillations," *J. of Fluids and Structures* **16**(1): 113-119
- Garg, V., K., 2002, "Low-Pressure Turbine Separation Control – Comparison with Experimental Data," GT-2002-30229, *Proceedings of TURBOEXPO 2002*, Amsterdam, Netherlands
- Gaster, M., 1963, "The stability of parallel flows and the behaviour of separation bubbles,"



*Ph.D. thesis*, Queen Mary College, London

Gatski, T.B., Speziale, C.G., 1993, "On explicit algebraic stress models for complex turbulent flows," *J. Fluid Mech.* **254**: 59-78

Gatski, T.B., Jongen, T., 2000, "Nonlinear eddy viscosity and algebraic stress models for solving complex turbulent flows," *Progress in Aerospace Sciences* **36**(8): 655-682

Glauser, M.N., Higuchi, H., Ausseur, J., Pinier, J., 2004, "Feedback Control of Separated Flows," AIAA-2004-2521

Gross, A., Fasel, H., 2002, "High-Order WENO Schemes Based on the Roe Approximate Riemann Solver," AIAA-2002-2735

Gross, A., Fasel, H.F., 2004, "Active Control of Separation for Low-Pressure Turbine Blades," AIAA-2004-2203

Henry, F.S., Pearcey, H.H., 1994, "Numerical Model of Boundary-Layer Control using Air-Jet Generated Vortices," *AIAA J.*, **32**: 2415-2425

Hunt J.C.R., Wray A.A., Moin P., 1988, "Eddies, stream, and convergence zones in turbulent flows," Report CTR-S88, Center For Turbulence Research, Stanford, California

Huerre, P., Monkewitz, P.A., 1990, "Local and global instabilities in spatially developing flows," *Ann. Rev. Fluid Mech.* **22**: 473-537

Israel, D.M., Fasse, E.D., Fasel, H.F., 2002, "Numerical Simulation of Closed Loop Active Flow Control of Separation," AIAA-2002-3282

Ito, K., Ravindran, S.S., 1998, "A Reduced-Order Method for Simulation and Control of Fluids Flows," *J. Comp. Phys.* **143**: 403-425

Jeong, J., Hussain, F. 1995, "On the Identification of a Vortex," *J. Fluid Mech.*, 285: 69-94.

Johari, H., McManus, K., 1997, "Visualization of Pulsed Vortex Generator Jets for Active Control of Boundary Layer Separation," AIAA-97-2021

Johnston, J.P., Nishi, M., 1990, "Vortex Generator Jets-Means for Flow Separation Control," *AIAA J.*, **28**: 429-436

Joslin, R.D., Gunzburger, M.D., Nicolaides, R.A., Erlebacher, G., Hussaini, M.Y., 1995, "A Self-Contained, Automated Methodology for Optimal Flow Control Validated for Transition Delay," ICASE-1995-64

Khan, Z.U., Johnston, J.P. 2000, "On Vortex Generating Jets," *Int. J. Heat and Fluid Flow*, **21**: 506-511

Kim, J.W., Lee, D.J., 2000, "Generalized Characteristic Boundary Conditions for Computational Aeroacoustics," *AIAA Journal* **38**(11): 2040-2049



- King, R., Becker, R., Garwon, M., Henning, L., 2004, "Robust and adaptive closed-loop control of separated shear flows," AIAA-2004-2529
- Lumley, J.L., 1967, "The structure of inhomogeneous turbulent flows," *Atm. Turb. And Radio Wave Prop.*, Nauka, Moscow and Toulouse, France, eds. Yaglom and Tatarsky, pp. 166-178
- Margolin, L.G., Rider, W.J., 2002 "A rationale for implicit turbulence modeling," *Int. J. Numer. Meth. Fluids*; **39**, pp. 821-841
- McManus, K., Legner, H., Davis, S., 1994, "Pulsed Vortex Generator Jets for Active Control of Flow Separation," AIAA-94-2218
- Marxen, O., Rist, U., Wagner, S., 2004, "Effect of spanwise-modulated disturbances on transition in a separated boundary layer," *AIAA J.*, **42**: 937-944
- Maucher, U., Rist, U., Wagner, S., 1997, "Secondary instabilities in a laminar separation bubbles," *Notes on Numerical Fluid Mechanics*, 229-236. Vieweg Verlag
- Meitz, H.L. and Fasel, H., 2000, "A Compact-Difference Scheme for the Navier-Stokes Equations in Vorticity-Velocity Formulation," *J. Comp. Phys.* 157:371-403
- Michelassi, V., Wissink, J.G., Fröhlich, J., Rodi, W., 2003, "Large-Eddy Simulation of Flow Around Low-Pressure Turbine Blade with Incoming Wakes," *AIAA J.*, **41** (11): 2143-2156
- Morkovin, M.V., 1969, "The many faces of transition," In *Viscous Drag Reduction* (ed. C.S. Wells). Plenum Press
- Mutnuri, P.K., Ayyalasomayajula, H., Ghia, U., Ghia, K., 2003, "Analysis of Separated Flow in a Low-Pressure Turbine Cascade, using Multi-Block Structured Grid," AIAA-2003-0793
- Noack, B.R., Afanasiev, K., Morzynski, M., Tadmor, G., Thiele, F., 2003, "A hierarchy of low-dimensional models for the transient and post-transient cylinder wake," *J. Fluid Mech.* **497**: 335-363
- Postl, D., Gross, A., Fasel, H.F., 2003, "Numerical Investigation of Low-Pressure Turbine Blade Separation Control," AIAA-2003-0614
- Postl, D., Gross, A., Fasel, H.F., 2004, "Numerical Investigation of Active Flow Control for Low-Pressure Turbine Blade Separation," AIAA-2004-0750
- Raverdy, B., Mary, I., Sagaut, P., 2003, "High-Resolution Large-Eddy Simulation of Flow Around Low-Pressure Turbine Blade," *AIAA J.*, Vol. 41, No. 3, pp. 390-397
- Rist, U. and Fasel, H., 1995, "Direct Numerical Simulation of Controlled Transition in a Flat-Plate Boundary Layer," *J. Fluid Mech.* 298:211-248
- Rizzetta, D.P., Visbal, M.R., 2003, "Numerical Investigations of Transitional Flow Through a Low-Pressure Turbine Cascade," AIAA-2003-3587



- Rizzetta, D.P., Visbal, M.R., 2004, "Numerical Simulation of Separation Control for a Transitional Highly-Loaded Low-Pressure Turbine," AIAA-2004-2204
- Roussopoulos, K., 1993, "Feedback control of vortex shedding at low Reynolds numbers," *J. Fluid Mech.* 248: 267-296
- Rowley, C.W., Colonius T., Murray R.M., 2004, "Model reduction for compressible flows using POD and Galerkin projection," *Physica D-Nonlinear Phenomena* 189(1-2): 115-129
- Rumsey, C.L., Gatski, T.B., 2001, "Recent Turbulence Model Advances Applied to Multielement Airfoil Computations," *J. of Aircraft* 38(5): 904-910
- Schlichting, H., Gersten, K., 2000, "Boundary Layer Theory," 8<sup>th</sup> edition, Springer, pp. 292, 353, 354
- Sharma, O., 1998, "Impact of Reynolds Number on LP Turbine Performance," *Proceedings of the 1997 Minnowbrook II Workshop on Boundary Layer Transition in Turbomachines*, NASA CP-1998-206958: 65-69
- Siegel, S., Cohen, K., McLaughlin, T., 2004, "Experimental Variable Gain Feedback Control of a Circular Cylinder Wake," AIAA-2004-2611
- Sondergaard, R., Bons, J.P., Rivir, R.B., 2002, "Control of Low-Pressure Turbine Separation Using Vortex Generator Jets," *Journal of Propulsion and Power* 18 (4): 889-895
- Sondergaard, R., Bons, J.P., Sucher, M., Rivir, R.B., 2002, "Reducing Low-Pressure Turbine Stage Blade Count Using Vortex Generator Jet Separation Control," *Proceedings of TURBOEXPO 2002*, Amsterdam, The Netherlands, June 3-6
- Suzen, Y.B., Huang, P.G., 2004, "Numerical Simulation of Transitional Flows as Affected by Passing Wakes," AIAA-2004-0103
- Wilcox, D.C., 2000, "Turbulence Modeling for CFD," Second Edition, DCW Industries
- Wynanski, I., 1997, "Boundary Layer and Flow Control by Periodic Addition of Momentum," AIAA-1997-2117
- Xiaohua, W., Durbin, P.A., 2001, "Evidence of Longitudinal Vortices Evolved from Distorted Wakes in a Turbine Passage," *J. Fluid Mech.* 446: 199-228
- Xiaohua, W., Jacobs, R.G., Hunt, J.C., Durbin, P.A., 1999, "Simulation of Boundary Layer Transition Induced by Periodically Passing Wakes," *J. Fluid Mech.* 398: 109-153
- Yee, H.C., 1987, "Upwind and Symmetric Shock-Capturing Schemes," NASA Technical Memorandum 89464